Statistical structure of plasma turbulence from BES measurements in MAST and the effect of flow shear



Michael Fox

Merton College

University of Oxford

A thesis submitted for the degree of

Doctor of Philosophy

October 2016

Abstract

The suppression of turbulent transport is a key requirement for enabling nuclear fusion to become a viable energy source. One possible route to achieving this suppression is through toroidal flow shear. We investigate the effect that flow shear has on the structure of turbulence by analysing data from both measurements of the fluctuating intensity field using the Beam-Emission-Spectroscopy (BES) diagnostic on the spherical tokamak MAST, as well as from numerical simulations of the fluctuating density field in MAST. We develop a procedure to map from the correlation parameters of the intensity field to the correlation parameters of the density field. This procedure is illustrated using the MAST BES system and the validity of the underlying assumptions is tested on fluctuating density fields generated by direct numerical simulations using the gyrokinetic code GS2. By using this procedure, we demonstrate how, in experiment, the flow shear associated with the differential toroidal rotation of tokamak plasmas breaks an underlying symmetry of the turbulent fluctuations imposed by the up-down symmetry of the magnetic equilibrium. Indeed, in both experimental BES measurements and gyrokinetic simulations, this symmetry breaking in ion-scale turbulence in MAST is shown to manifest itself as a tilt of the spatial correlation function and a finite skew in the distribution of the fluctuating intensity (density) field. The tilt is a statistical expression of the "shearing" of the turbulent structures by the mean flow. The skewness of the distribution is related to the emergence of long-lived density structures in sheared, near-marginal plasma turbulence. The extent to which these effects are pronounced is argued (with the aid of the simulations) to depend on the distance from the nonlinear stability threshold. Away from the threshold, the symmetry is effectively restored.

Contents

Contents ii

List of Figures vi

List of Tables vii

I Introduction 1

1 The problem of turbulence 3
1.1 Nuclear fusion as an energy source . . . 3
1.2 Confinement of particles and energy in a tokamak . . . 4
1.3 Turbulence in tokamaks . . . 6
1.3.1 Linear instabilities . . . 6
1.3.2 Subcritical turbulence . . . 7
1.3.3 The spatial structure of turbulence in a tokamak . . . 8
1.4 The role of flow shear . . . 8
1.5 The Mega-Ampere Spherical Tokamak . . . 10
1.6 Measuring turbulence using BES . . . 11
1.7 Modelling turbulence with the gyrokinetic equation . . . 14
1.7.1 The gyrokinetic equation . . . 14
1.7.2 Solving the gyrokinetic equation . . . 16
1.8 Structure of this work . . . 16
1.9 Author's contributions . . . 18
1.9.1 Published papers . . . 18
1.9.2 Conference submissions . . . 18

II Measuring turbulence using Beam-Emission Spectroscopy 19

2 Introduction and measurement methods 21
2.1 Correlation parameters of the measured BES signal . . . 22
2.1.1 Fluctuation amplitude . . . 23
2.1.2 Correlation time . . . 23
2.1.3 Apparent poloidal velocity . . . 25
2.1.4 Two-dimensional spatial correlation parameters . . . 25

3 Correlation parameters of the physical density field 29
3.1 Plasma frame . . . 29
3.2 Laboratory frame . . . 30
3.2.1 Spatial correlation function . . . 30
3.2.2 Temporal correlation function . . . 30
3.2.3 Asymptotic ordering for the CCTD method . . . 31

3.2.4 Laboratory-frame correlation time . . . 32
3.2.5 Low-Mach-number ordering . . . 32
3.2.6 Laboratory-frame poloidal velocity . . . 33

4 Point-Spread Functions **35**
4.1 Calculation of PSFs for BES systems . . . 35
4.2 Characterisation of the PSFs . . . 36
4.3 PSFs in MAST: 5 representative cases . . . 37
4.4 Gaussian-model PSFs . . . 38
4.5 Difference between real and Gaussian-model PSFs . . . 39

5 Analytic calculations of the effect of PSFs **41**
5.1 Effect of PSFs on the 2D spatial structure of the correlation function . 41
5.2 Effect of PSFs on the fluctuation amplitude . . . 44
5.3 Effect of PSFs on the correlation time and poloidal velocity . . . 45

6 Characterising the effect of PSFs on correlation parameters **47**
6.1 Model fluctuating density field . . . 47
6.2 The effects of real PSFs . . . 48
6.2.1 Fluctuation amplitude . . . 50
6.2.2 Radial correlation length . . . 50
6.2.3 Poloidal correlation length . . . 50
6.2.4 Tilt angle of the correlation function . . . 51
6.2.5 Correlation time . . . 52
6.2.6 Apparent poloidal velocity . . . 52
6.3 Validity of using Gaussian-model-PSFs . . . 52
6.3.1 Fluctuation amplitude . . . 53
6.3.2 Radial correlation length . . . 53
6.3.3 Poloidal correlation length . . . 53
6.3.4 Tilt angle of the correlation function . . . 54
6.3.5 Correlation time and apparent poloidal velocity . . . 54
6.4 Summary . . . 54

7 Correcting for PSF effects **55**
7.1 Laboratory-frame spatial correlation parameters and fluctuation amplitude . . . 55
7.2 Plasma-frame spatial correlation parameters and fluctuation amplitude 56
7.3 Resolution limit of BES . . . 56
7.4 Testing the inversion method using gyrokinetic simulations . . . 58
7.4.1 Assumptions of our method . . . 58
7.4.2 Gyrokinetic simulations . . . 59
7.4.3 Spatial correlation parameters . . . 59
7.4.4 Fluctuation amplitude . . . 62

8 Temporal correlation parameters: further refinements **63**
8.1 Physical interpretation of the correlation time . . . 64

8.2 Introducing a fluctuating radial velocity into the model of fluctuating fields . . . 64
8.3 Limitations of our model . . . 66
8.4 Apparent poloidal velocity . . . 68

9 Conclusions of Part II **71**

III The effect of flow shear on turbulence **75**

10 Introduction **77**
10.1 Symmetry of the field distribution . . . 78
10.2 Symmetry of the correlation function . . . 78

11 Symmetry breaking in experimentally measured plasma turbulence in MAST **81**
11.1 The MAST BES system . . . 81
11.2 Experimental example cases . . . 82
11.3 Two-dimensional spatial structure of the turbulence . . . 86
11.3.1 Instantaneous turbulent density field . . . 86
11.3.2 Spatial correlation function . . . 87
11.3.3 Symmetry breaking . . . 88
11.3.4 Correlation times and flow shear . . . 90
11.3.5 Case of intermediate flow shear . . . 91
11.4 Distribution of fluctuation field . . . 92
11.4.1 Symmetry breaking . . . 93
11.4.2 Skewness vs. tilt: two-component turbulence? . . . 95

12 Symmetry breaking in numerically simulated gyrokinetic turbulence **99**
12.1 Tilt vs. flow shear . . . 103
12.1.1 Tilt and life time . . . 103
12.1.2 Tilts at zero flow shear as a signature of zonal flows . . . 104
12.2 Skewness vs. flow shear . . . 105
12.2.1 Physics of skewed distributions . . . 107
12.2.2 Skewness vs. tilt: two-component turbulence in simulations . . . 108
12.3 Restoration of symmetry far from threshold . . . 110
12.3.1 Tilt, flow shear and life time . . . 111
12.3.2 Tilt and skewness vs. distance from threshold . . . 112

13 Discussion **115**

IV Conclusions **117**

14 Conclusions and future work **119**

V Appendices **121**

A Measuring the product of the poloidal wavenumber and poloidal correlation length **123**

B Modelling a fluctuating field **125**
B.1 Basic equations . . . 125
B.2 Plasma-frame correlation function . . . 128
B.3 Laboratory-frame correlation function . . . 130
B.4 Fluctuation amplitude . . . 131
B.5 Method for generating a fluctuating field . . . 132
B.6 Input parameters . . . 133

C CCTD method: apparent poloidal velocity and correlation time **135**
C.1 CCTD method in the laboratory frame . . . 135
C.1.1 Zeroth order . . . 136
C.1.2 Second order corrections to the peak amplitude of the correlation function . . . 136
C.1.3 Apparent poloidal velocity . . . 137
C.1.4 Correlation time . . . 137
C.2 PSF effects on the correlation time and apparent poloidal velocity . . . 138

D Quantifying the difference between real and Gaussian-model PSFs **141**
D.1 Difference of the shape of real PSFs from a tilted Gaussian function . . . 141
D.2 Spatial variation of PSFs . . . 143
D.3 Variation of PSF amplitudes . . . 143
D.4 Shifted centres of PSFs . . . 143

E Measuring skewed distributions **145**
E.1 Accounting and correcting for spurious skewness . . . 145
E.2 PSF effects . . . 147

Bibliography **151**

List of Figures

1.1 Sketch of ITG instability 6
1.2 Sketch of BES view location in MAST 11
1.3 Comparing measurements with the resolution limit of the MAST BES . . 13
2.1 PSF e^{-1} amplitude contours for the five representative cases 22
2.2 Example time delay correlation functions 24
2.3 Example binned and corrected spatial correlation functions 27
4.1 Characterisation of PSFs 37
4.2 Histogram of percentage differences between real and Gaussian-model PSFs 39
5.1 Contour lines of Ω 43
6.1 Real and Gaussian-model PSF effects on the turbulence correlation parameters 49
7.1 Resolution limits of BES measurements 56
7.2 Testing the reconstruction of spatial correlation parameters using a gyrokinetic simulation of a fluctuating density field 60
8.1 PSF effects on the correlation time measured from gyrokinetic simulations 63
8.2 Enlargement of Figure 6.1(e) 67
8.3 Time-delayed correlation functions from GS2 68
11.1 Equilibrium profiles for the three experimental cases: BLM, DLM, and IFS 83
11.2 Snapshots of raw BES fluctuating-intensity signal 86
11.3 Spatial correlation functions for BLM and DLM cases 89
11.4 Correlation function for the IFS case 91
11.5 Distribution of fluctuating intensity field for BLM and DLM cases 93
11.6 Distribution of fluctuating intensity field for IFS case 94
11.7 Conditional spatial correlation functions for BLM case 95
12.1 Spatial correlation functions from a scan in flow shear using gyrokinetic simulations 101
12.2 Dependence of lifetime of the turbulence on flow shear and on the ion turbulent heat flux 102
12.3 Integrated (over y) fluctuating density field from run GKa5 104
12.4 Conditional (on space) correlation function for run GKa5 104

12.5 Dependence of the distribution of the fluctuating density field on flow shear . . . 106
12.6 Conditional correlation function for run GKa1 . . . 108
12.7 Conditional correlation function for Marginal run, with and without high-pass filtering . . . 109
12.8 Dependence of tilt and skewness on the distance from the nonlinear marginal stability boundary . . . 113
A.1 Testing the method of reconstructing $k_{Z|L}\ell_{Z|L}$ . . . 123
D.1 Quantifying the difference between real and Gaussian-model PSFs . . . 142
E.1 Procedure for processing data before measuring skewness . . . 146
E.2 PSF effects on skewness . . . 148

List of Tables

1.1 MAST plasma and engineering parameters . . . 10
2.1 Example spatial-fit parameters for BES data in Figure 2.3 . . . 27
4.1 Mean PSF characteristics for the five representative cases in Figure 2.1 . 37
4.2 Differences from Gaussian for the five representative cases and difference between real and Gaussian-model PSF effects on tilt angle . . . 40
7.1 Spatial correlation parameters of Figure 7.2 . . . 61
11.1 Local equilibrium parameters for the three experimental cases and the numerical case . . . 84
11.2 Plasma-frame correlation parameters for the three experimental cases . . 89
11.3 Plasma-frame correlation parameters for the conditional spatial correlation functions of the BLM and IFS cases . . . 97
12.1 Turbulence parameters from a scan in flow shear using gyrokinetic simulations . . . 100
12.2 Turbulence parameters from a scan in ion-temperature gradient using gyrokinetic simulations . . . 110
B.1 Input parameters for generating time series from the model of fluctuating fields . . . 133

Acknowledgements

This Thesis would not exist if it were not for my two supervisors Prof. Alex Schekochihin and Dr. Anthony Field. Together, they have taught me a great deal, from theories of plasma turbulence to the details of experimental hardware, and probably most things in between. For that knowledge, I am exceedingly grateful.

Over the course of this DPhil project I have met many people who have contributed in part to this work, through working together, by providing necessary distraction, or a bit of both. The primary culprits are my friends, colleagues, and fellow DPhil students in the Plasma Theory group: Justin Ball, Greg Colyer, Archie Bott, Alessandro Geraldini, Michael Hardman, Joseph Parker, and Ferdinand van Wyk. To Ferdinand goes a special thanks, for his toils with GS2, of which some of the results feature in this Thesis. I must similarly thank my fellow PhD students based at Culham Centre for Fusion Energy, for their pearls of wisdom: Jakob Brunner, Stuart Henderson, Jack Lovell, Sam Murphy-Sugrue, David Thomas, and Nick Walkden.

I have also had the great pleasure of learning the details of the gyrokinetic equation from Ian Abel and Edmund Highcock. A special mention must be made to Young-chul Ghim, who, as my direct predecessor, developed many useful tools that I have come to rely on. Further gratitude is reserved for Sarah Newton, Daniel Dunai, and Jon Hillesheim, with whom I have had many insightful discussions. I would also like to thank everybody who has sat in a group meeting when I have been presenting my work, for their patience and advice; these include Prof. Michael Barnes, Prof. Steve Cowley, Prof. Paul Dellar, Prof. Tim Horbury, and Prof. Felix Parra.

Merton College has been my home in Oxford for the last eight years, during that time I have met an outstanding array of people, and made too numerous friends, who I wish to acknowledge, to list here. Most notable of these is Robert Jeffrey, who has suffered and celebrated the life of Merton Physics with me. And, of course, Jutta Toscano, whose presence makes every day better.

Finally, I wish to thank my parents for bringing me up with the freedom to explore whatever interested me, and my sister for being there when I needed her.

Part I

Introduction

CHAPTER 1

The problem of turbulence

The existence of turbulence has hindered the progress of humankind for centuries, as witnessed in the 11^{th} century by Eilmer the monk in an early attempt at flight [1]:

> *But agitated by the violence of the wind and the swirling of air, as well as by the awareness of his rash attempt, he fell, broke both his legs and was lame ever after.*

The turbulence, of which this thesis is concerned, is unlikely to cause bodily harm, however, it has prevented the realisation of a new way of generating electricity: nuclear fusion. This is unfortunate, because fusion can be considered an ideal energy source: the fuel, Deuterium (D) and Tritium (T), is extracted from two of the most abundant resources on Earth, water and Lithium; the reaction(s) produce lower levels of nuclear waste than fission reactors; there is no possibility of meltdown; no capacity for the proliferation of nuclear weapons; and there are no direct Carbon emissions. To understand why turbulence becomes an issue, we first have to understand the conditions required for nuclear fusion to occur.

1.1 Nuclear fusion as an energy source

For a nuclear fusion reaction to occur, two nuclei have to be approximately within a nuclear radius of each other. At these small distances the electrostatic repulsion due to the positive charge on each nucleus is extremely strong and, therefore, the nuclei require high initial kinetic energies to overcome this potential barrier. These energies correspond to $10 - 100\ \mathrm{keV}$, which drastically exceed the ionisation energy of Hydrogen, at $13.6\ \mathrm{eV}$. At such high temperatures the atoms are fully ionised and form an electrically neutral plasma.

Ideally, the energy released by the fusion reaction should be great enough to maintain the temperature of the plasma, as well as to provide power to the grid. The threshold condition for this to occur is called ignition and is defined by the triple product [2, 3]:

$$\hat{n}\hat{T}\tau_E > 5 \times 10^{21} \mathrm{m}^{-3}\,\mathrm{keV\,s}, \tag{1.1}$$

where $\hat{n}$ is the peak density, $\hat{T}$ is the peak temperature, and τ_E is the confinement time of the plasma. The confinement time is the ratio of energy stored in the plasma to the input power into the plasma, which, in the above expression, is assumed to come solely from alpha particle (He) heating, due to the following reaction:

$$\mathrm{D} + \mathrm{T} \longrightarrow \mathrm{He}(3.5\mathrm{MeV}) + \mathrm{n}(14.1\mathrm{MeV}).$$

A plasma at such high temperatures will rapidly cool onto any container it comes into physical contact with. The solution to this problem is to use the fact that the charged particles in the plasma will respond to magnetic fields. The tokamak configuration confines a torus shape plasma within externally applied toroidal and vertical magnetic fields, and a poloidal magnetic field generated by a toroidally directed current inside the plasma. The tokamak is the most successful terrestrial confinement method, with a triple product of $1 \times 10^{21}\ \mathrm{m}^{-3}\,\mathrm{keV\,s}$ achieved in the Joint European Torus (JET) [4].

The radius of the poloidal cross section of a plasma in a tokamak is typically of the order of a metre. Across this distance the temperature drops from $\sim 1\ \mathrm{keV} \simeq 10^7\ \mathrm{K}$ to effectively zero. The density also drops from $\sim 10^{20}\ \mathrm{m}^{-3}$ in the core to near vacuum at the walls. Therefore, there are very steep gradients in temperature and density, which can drive instabilities that excite turbulence (for an example see Section 1.3.1). The problem with turbulence is that it acts to reduce the gradients that are causing it, by transporting heat and particles radially out of the plasma core at a faster rate than otherwise would be possible by collisions and particle drifts (neoclassical transport). This then limits the maximum temperature and density achievable in the core, and thus prevents (1.1) from being satisfied. However, if the turbulence and its resulting transport can be suppressed, then ignition may be achieved. This thesis is concerned with one possible way to suppress the turbulence, which is through the presence of a radial gradient in the toroidal rotation of the plasma, which we refer to as 'flow shear'. Before discussing flow shear further, it is necessary to understand how a tokamak confines charged particles, and also what it means for a plasma to be turbulent.

1.2 Confinement of particles and energy in a tokamak

A charged particle in a constant, uniform magnetic field exhibits circular motion perpendicular to the magnetic field line and experiences no force parallel to the magnetic field. The radius of the circular motion is called the gyroradius, and for a

given species, s, is:

$$\rho_s \equiv \frac{v_\perp}{\omega_s}, \tag{1.2}$$

where $v_\perp$ is the perpendicular velocity, $\omega_s = q_s B/m_s$ is the gyrofrequency, with q_s the charge, B the total magnetic field strength, and m_s the mass.

Through their gyration around the magnetic field, the particles are confined in the direction perpendicular to the field. Confinement in the parallel direction is achieved by the wrapping of the field lines around the torus. For the equilibrium of the plasma to be stable to magneto-hydrodynamic (MHD) modes a poloidal and vertical magnetic field are required in addition to the toroidal field, which are the defining features of a tokamak [3, 5].

The particle motion becomes more complicated in the tokamak geometry: the strength of the toroidal magnetic field decreases with major radius, which leads to the trapping of a fraction of the particles, as well as drifting of the particles across field lines. However, because of the presence of an axisymmetric poloidal field these drifts close on themselves and particles are not lost from the plasma.

In the absence of turbulence, the only way that particles can move off their defined (drift) orbits, and therefore transport particle density and heat radially, is through collisions. However, this collisional transport typically occurs at a much slower rate than turbulent transport.

The confinement of particles is neither a necessary, nor sufficient condition for the confinement of energy. However, it does reduce the number of ways in which energy can be transported. Indeed, by using a strong externally applied toroidal field to confine the plasma, most of the energy of the system is in that magnetic field. The ratio of the thermal energy of the plasma to the magnetic energy is the plasma beta [5]

$$\beta \equiv \frac{p}{B^2/(2\mu_0)}, \tag{1.3}$$

where p is the total plasma pressure and μ_0 is the permeability of free space. Typical values of β for conventional tokamaks are in the range of a few percent. This has the implication that fluctuations of the magnetic field lines δB are small compared to fluctuations in pressure (density and temperature), and, therefore, particles and heat effectively cannot be transported by bending magnetic field lines.

Finally, a charged particle undergoing acceleration radiates energy. The dominant emission mechanism in tokamaks is through Bremsstrahlung radiation from Coulomb collisions between electrons and ions [5]. Other, smaller contributions include cyclotron and impurity line emission. Comparing the power losses from Bremsstrahlung (using equation 3.45 from [5]) with the turbulent transport of heat

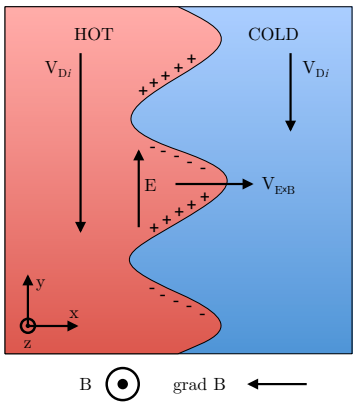


Figure 1.1: Sketch of the ion-temperature gradient instability in a slab geometry with curvature, following [9].

(using equation 2 from [6], appropriately rearranged) shows that the radiative contribution to the energy transport is at least an order of magnitude smaller than the turbulent transport, for typical MAST parameters (see Section 1.5). Indeed, experimental measurements from MAST have shown that radiative losses contribute to less than 10% of the total power balance [7].

1.3 Turbulence in tokamaks

Turbulence is the result of nonlinear physics, i.e., the interaction of a field (density, temperature, electrostatic potential, velocity, etc.) with itself. The characteristic features of a turbulent field are that it exhibits a wide and continuous distribution of length and time scales, and the trajectory of an element of the field is very sensitive to its initial conditions; in that sense the field is chaotic [8]. This second feature means that any predictive theory of turbulence must be based on the statistical properties of the field.

There are two distinct ways in which a field can become turbulent, through the growth of a linear instability or due to pre-existing noise in the system. In the below sections we will discuss these further, before discussing the current knowledge of the structure of turbulence in tokamaks.

1.3.1 Linear instabilities

A linear instability exponentially increases the amplitude of a mode (a specific or range of wavenumbers, or frequencies) in the plasma. In the absence of a nonlinearity this mode will grow eternally. Generally speaking, the nonlinearity saturates

the growth of this mode by transferring the energy of that mode into other modes, producing the distribution of length and time scales of a turbulent field.

There are a large range of different linear instabilities that can exist. The common feature shared by the different instabilities is that they are driven by gradients of the equilibrium fields. As a concrete example, let us consider a simplified version of the ion-temperature gradient instability, which is treated fully in [10]. We follow the Rosenbluth-Longmire [11] particle picture, elucidated in [9]. Consider two regions of plasma with different temperatures and a discontinuous boundary in the $y-z$ plane, which therefore gives a temperature jump that decreases in the x direction (see sketch in Figure 1.1). A magnetic field of strength B penetrates the plasma in the z direction, and has a gradient, ∇B that decreases in the x direction. This configuration is characteristic of the outboard side of a tokamak.

The drift velocity of the ions due to a gradient in the magnetic field is [5]

$$\mathbf{V}_{Ds} = \frac{v_\perp^2}{2\omega_s}\frac{\mathbf{B}\times\nabla B}{B^2}. \tag{1.4}$$

The electron drift velocity is in the opposite direction to the ion drift velocity, producing a net current. The dependence of the drift velocities on the perpendicular particle velocity in (1.4) means that the drift velocity is higher in the higher temperature region of the plasma.

Now, we consider a wave-like perturbation to the boundary layer, as shown in Figure 1.1. The difference in drift velocities between the hot and cold regions of the plasma causes charge to build up on the boundary layer. The charge difference gives rise to an electric field, which then causes an $\mathbf{E}\times\mathbf{B}$ drift. This $\mathbf{E}\times\mathbf{B}$ drift acts in the direction that reinforces the initial perturbation, causing it to grow, and grow exponentially fast.

Other linear instabilities include the electron-temperature gradient (ETG) mode [12, 13], which is similar to the ITG instability, but is associated with wavenumbers on the electron-gyroradius scale, rather than the ion-gyroradius scale. For MAST plasmas, the trapped-electron mode (TEM) instability [14, 15] can also be important [16], as the large variation in the magnetic field geometry increases the trapped-particle population. This instability has typical wavenumbers that span the range between the ion gyroradius and the electron gyroradius.

1.3.2 Subcritical turbulence

The second way in which a field can become turbulent is if there is noise in the system with sufficiently high amplitude to activate the nonlinearity. Then the nonlinearity can cause fluctuations to grow (as well as decay), in order to sustain the turbulent field.

It can be argued that the threshold amplitude requirement on the noise in the system is no different from the saturation of a linear instability once it reaches a certain amplitude, and therefore the turbulence itself is not fundamentally different between the two cases. However, as we shall see in Section 1.4, it is an important point that a turbulent state can be reached in the absence of any linearly unstable modes; this is the essence of subcritical turbulence [17, 18, 19].

1.3.3 The spatial structure of turbulence in a tokamak

The presence of the strong magnetic field in a tokamak has the implication that the turbulence is anisotropic. This is not surprising, given the distinctly different behaviour of particles in the directions parallel and perpendicular to the magnetic field discussed in Section 1.2. As the motion parallel to the magnetic field is unconstrained, it is clear that we would expect turbulent perturbations to be elongated in this direction. Indeed, experimental measurements at the plasma edge [20, 21, 22] have shown filamentary structures elongated in the parallel direction. The presence of long parallel structures in the outer core of a tokamak can be inferred from toroidal velocity measurements [23] made using Beam-Emission Spectroscopy (BES) in the Mega-Ampere Spherical Tokamak (MAST), see Section 1.6 for more details.

The exact extent to which the turbulence is anisotropic, and what determines the lengths in the parallel and perpendicular directions, remains an open question. Some progress has been made using the critical balance conjecture [24, 25], first applied to experiment in an astrophysical context [26]. This relates the parallel and perpendicular directions by asserting that two points remain spatially correlated in the parallel direction only for as long as they remain spatially correlated in the perpendicular direction. Critical balance has been used to derive a scaling relationship for the turbulent heat flux with temperature gradient, which has been confirmed in gyrokinetic simulations [27]. Whilst, experimental evidence supporting critical balance has been found on MAST [28], where the linear instability drive, turbulent correlation time, ion streaming time along the magnetic field, and the magnetic drift time were found to be of similar magnitude and scaled together.

The spatial and temporal structure of turbulence determines the level of heat flux through the plasma [6], understanding how flow shear affects this structure is, therefore, key to understanding the role flow shear can play in the suppression of turbulence.

1.4 The role of flow shear

A tokamak plasma rotates freely in the toroidal direction [29], which can occur due to both internal rearrangement of the angular momentum by turbulence: in-

trinsic rotation [30, 31, 32]; and the injection of angular momentum from external sources, such as neutral beams. In this work, for diagnostic reasons, we will only be concerned with the latter. The primary purpose of neutral beam injection (NBI) is to heat the plasma core, however, to maximise the energy deposition, neutral beams are often injected at an angle to the major radius (see Figure 1.2), which then provides a source of angular momentum.

As a result of the deposition profile of the NBI, the core of the plasma rotates faster than the edge. A radial gradient in the toroidal flow results, which is the flow shear:

$$\gamma_E \equiv -\frac{RB_Z}{B}\frac{\mathrm{d}\omega}{\mathrm{d}R}, \tag{1.5}$$

where R is the major radius, B_Z the poloidal component of the magnetic field, and ω is the toroidal angular frequency. Note, this definition does not include contributions from the pressure gradient or poloidal rotation velocity, unlike definitions used in the literature [33]. However, the poloidal rotation is not measured, but is known to be small [34, 35], and we have checked that the pressure gradient term is numerically small compared to (1.5) in all the analysis performed for this thesis. It should be further noted that, in general, it is not expected that the pressure-gradient contribution may always be neglected, especially in H-mode plasmas, where there is a steep pressure gradient at the edge [36].

The ratio of the poloidal magnetic field to the total magnetic field features in (1.5) because we are specifically interested in the component of the toroidal velocity perpendicular to the magnetic field (in the binormal direction). This is an important distinction, because the component parallel to the magnetic field can drive the parallel-velocity-gradient (PVG) instability [37, 38], which is similar in nature to the ITG instability described in Section 1.3.1.

It is known from theory and simulations that flow shear, in the absence of magnetic shear, prevents unstable modes from growing in perpetuity; doing so by increasing the radial wavenumber secularly in time (see Section 10.2) until being damped at the ion-gyroradius scale [18], or in the fluid limit, collisionally [39]. Indeed, because of the flow shear, it is generally the case in MAST that all linear modes are stable. However, turbulence is still present, and is subcritical [40].

Experimentally, it is well known that flow shear can suppress the fluctuation amplitude of an established turbulent field [41], the most pertinent example being the low (L) to high (H) confinement transition within tokamak plasmas [42, 43]. However, our theoretical understanding of how flow shear affects nonlinearly saturated turbulence is far from complete. This is not for a lack of trying [44, 45, 46, 47, 48, 49]. The main problem is being able to discriminate between the different proposed the-

Parameter	Typical value	
Minor radius - a (m)	0.65	
Major radius - R (m)	0.85	
Diameter of vacuum vessel (m)	4.0	
Height of vacuum vessel (m)	4.4	
SS neutral beam* power (MW)	2.0	(max 2.5)
SS neutral beam energy (kV)	67	(max 75)
Plasma current (MA)	1.3	
Toroidal field at major radius (T)	0.5	
Pulse duration (s)	0.5	(max 1.0)
Plasma volume (m^3)	10	
Plasma density (m^{-3})	$10^{19} - 10^{20}$	
Core temperature (keV)	1.0	(max 2.7)

Table 1.1: Typical plasma and engineering parameters for MAST [50]. *MAST has two neutral beams located at different ports: SS and SW, see Figure 1.2.

ories. In order to do this, we must look to experiment.

1.5 The Mega-Ampere Spherical Tokamak

MAST, and the National Spherical Torus Experiment (NSTX) in Princeton, are the world's largest and most advanced Spherical Tokamaks (ST) [51]. Engineering and typical plasma parameters of MAST are given in Table 1.1. The main difference between an ST, and a conventional tokamak is its small aspect ratio ($A = R/a < 1.3$, where a is the minor radius of the plasma). The initial motivation for the development of STs was based on cost and speed of development [52]: the small aspect ratio means that the total physical size of the device is smaller than a conventional tokamak, reducing fixed material costs. Furthermore, the ability to achieve high plasma beta (1.3), due to the improved shaping of the plasma [53], means that lower magnetic fields are required to achieve the same plasma pressure, and, therefore, the current required in the coils is reduced, lowering running costs.

The MAST tokamak is well suited to studying turbulence, because the plasma is extremely well diagnosed. Ion-scale turbulence in the density field is measured using the BES system [54], being the main focus of this thesis, which we will discuss in more detail in Section 1.6. Additionally, the Doppler backscattering system (DBS) is capable of measuring higher wavenumber turbulence (intermediate ion-electron scales) [55]. While a new 2D DBS capability, demonstrated using the Synthetic Aperture Microwave Imaging (SAMI) diagnostic has recently been developed [56].

The study of turbulence is not isolated, as properties of the turbulent field will be affected by the equilibrium parameters, as seen in Section 1.3.1. The plasma equilibrium is reconstructed from magnetic measurements using the EFIT code [57, 58],

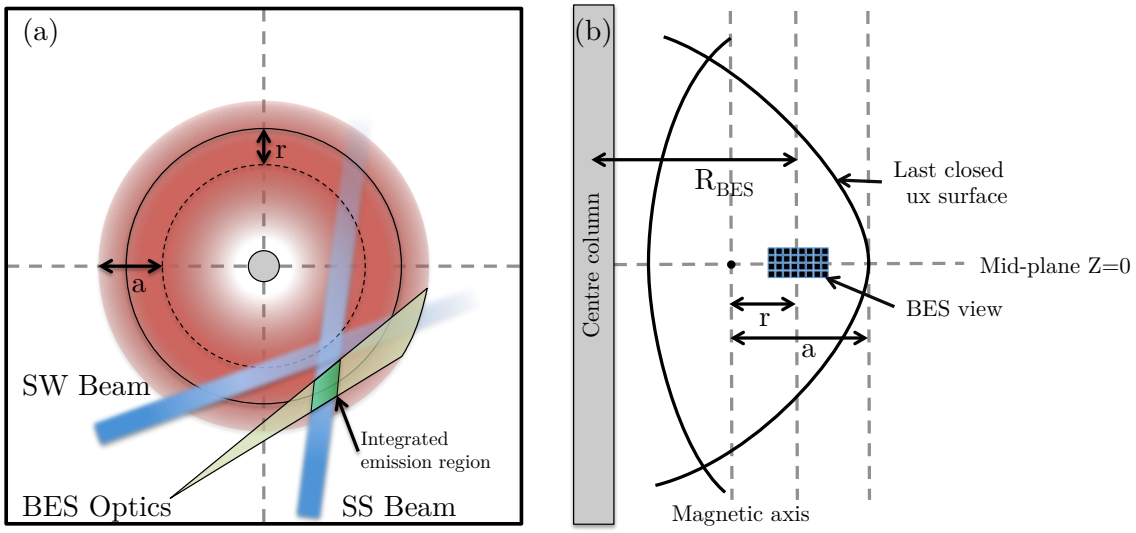


Figure 1.2: Sketch of BES view location in MAST: (a) from above, including the positions of the two neutral beams; (b) in the radial-poloidal plane.

together with radial profile measurements from the charge exchange recombination spectroscopy (CXRS) diagnostic [59] of the ion temperature (and toroidal velocity); from the Thomson scattering (TS) diagnostic [60, 61] of the electron temperature and density; and from the motional Stark effect (MSE) diagnostic [62] of the pitch angle of the magnetic field; in addition to external magnetic measurements from Mirnov coils [63] and the current in the magnetic field coils. The TS and CXRS systems both have a spatial resolution of $1\ \mathrm{cm}$, and the MSE system has a spatial resolution of $2.5\ \mathrm{cm}$, which gives high resolution equilibrium profiles, necessary for determining the gradients of temperature, density and velocity that drive and suppress turbulence.

1.6 Measuring turbulence using BES

Beam-Emission Spectroscopy (BES) allows us to image the ion-scale turbulence inside the plasma [64]. In MAST, emission from the D_α transition ($n = 3 \rightarrow 2$) of collisionally excited neutral beam atoms is used to diagnose density fluctuations, as the excited population of the $n = 3$ state is proportional to the local plasma density [65]. The wavelength of this emission is Doppler shifted from $\lambda = 656.1\ \mathrm{nm}$ to longer wavelengths, by between $2 - 3\ \mathrm{nm}$, dependent on the beam energy and tangency angle of the line of sight with the beam [54]. This Doppler shift is important, because it allows the beam emission to be distinguished from both the D_α emission from the edge and two C^{2+} emission lines (at $657.8\ \mathrm{nm}$ and $658.3\ \mathrm{nm}$), using

a bandpass interference filter.

As the beam has a finite width, of approximately $20\,\mathrm{cm}$, the emission is integrated along the line of sight through this width. The loss in spatial resolution due to this effect is mitigated by aligning the lines of sight parallel to the local magnetic field; then, as the turbulence is elongated in the parallel direction (see Section 1.3.3), the integration is localised to single fluctuations (see Figure 1.2). Unfortunately, as we will see in Chapter 4, the pitch angle of the magnetic field evolves and, therefore, the alignment changes with time during the experiment. As a result, the spatial response of the BES is also a function of time.

The spatial response is quantified by the point-spread functions (PSFs) of the system [66]. In addition to the integration through the beam width, the PSFs also include spatial de-localisation effects from the finite lifetime of the excited atomic state, and the finite solid angle of the optical system, though both these effects are small compared to the misalignment of the lines of sight with the magnetic field.

The optical system is designed to maximise the photon throughput, with a large aperture and steerable mirror system to focus the incoming light onto the detector [67]. A set of 32 avalanche photodiode (APD) detectors [68], arranged into an 8×4 radial-poloidal grid, see Figure 1.2(b), is employed to record the photons at a frequency of $2\,\mathrm{MHz}$. The back projection of a single detector channel on to the neutral beam line illuminates a region of approximately $1.5 \times 1.5\,\mathrm{cm}^2$, providing a constraint on the spatial resolution of the system (ignoring the effects discussed in the previous paragraph). The BES is capable of viewing a $16\,\mathrm{cm} \times 8\,\mathrm{cm}$ region of the plasma, which, in the radial direction, covers approximately one quarter of the minor radius.

The system is, therefore, capable of imaging the two-dimensional spatial structure of the turbulent density field. The fluctuations observed in this field often have a large apparent velocity in the poloidal direction. This velocity is, in fact, a result of the combination of two factors: the bulk toroidal motion of the plasma, and the alignment of the elongated turbulent structures parallel to the magnetic field, which is at a finite angle ($\sim 30^\circ$) to the toroidal direction. The result is a projection of the toroidal motion onto the poloidal plane, causing the so-called 'barber pole' effect [23]. This apparent poloidal velocity has been measured experimentally and has been used to calculate the toroidal velocity, which has been compared with the toroidal velocity measured using CXRS and DBS systems, showing good agreement [55].

As discussed in Section 1.4, theoretical expectations are that flow shear should increase the radial wavenumber of the turbulent field. Therefore, measuring the radial wavenumber should be of primary importance to any investigation into the

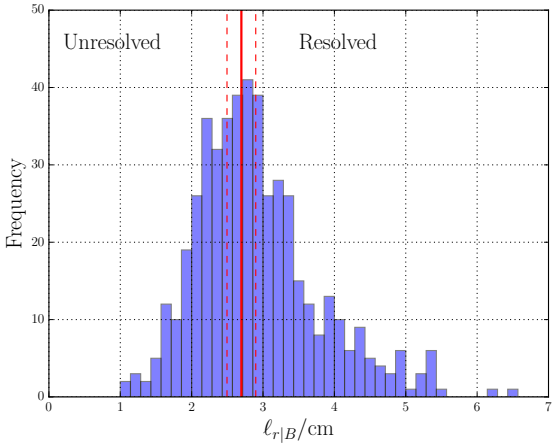


Figure 1.3: Histogram of radial correlation lengths, $\ell_{r|B}$, of the intensity field measure from the MAST BES. The red vertical line indicates the radial resolution limit (7.6), as calculated in Section 7.3, averaged over 487 measurements. Less than half (274) of these measurements are above their own resolution limit.

effects of flow shear. The two-dimensional array of channels of the BES system is, in principle, able to measure the spatial structure, and therefore radial wavenumber of the intensity field that it detects. However, before looking for relationships between turbulence parameters and flow shear (or other equilibrium parameters), which will be done in Part III of this thesis, it is necessary to understand whether the structure of the measured intensity field is representative of the structure of the underlying turbulent density field of the plasma.

The reason that this question arises is because the radial correlation length of the turbulence[1] is often measured to be similar to the spatial size of the PSFs. This is illustrated in Figure 1.3, where the measured radial correlation length $\ell_{r|B}$ is compared to the resolution limit calculated from analysing the PSFs (see Section 7.3). The peak of the distribution of radial correlation lengths occurs at the same length as the mean radial resolution limit, strongly suggesting that most of these measurements are dominated by the effect of PSFs.

Before ending this introduction and moving onto investigating the effects of PSFs on the measurement of turbulence parameters in Part II, it is necessary to introduce the gyrokinetic equation.

[1]The radial correlation length is measured independently from the radial wavenumber, and in Fourier space is the reciprocal of the width of the radial wavenumber spectrum, while the radial wavenumber itself gives the position of the peak in this spectrum.

1.7 Modelling turbulence with the gyrokinetic equation

As turbulence is a non-linear process, for most problems only numerical solutions can be found. Hence, we look for the simplest set of equations (in terms of solving numerically) that provide the most complete physical description of the problem. For tokamak plasmas this is the gyrokinetic equation. This equation retains the kinetic effects required to accurately model the behaviour of trapped particles (whose population depends on the distribution in parallel and perpendicular velocity space), whilst neglecting the fast variation of the gyrophase[2]

The gyrokinetic equation is used in Part III of this thesis to provide the context for the experimental observations, through a discussion of the symmetry properties of the equation, and how the symmetry is broken by the presence of flow shear. Numerical simulations of a turbulent density field using the gyrokinetic equation are used in both Parts II and III. In Chapter 7, the simulations are used to test the PSF correction method and, in Chapter 12, they are used to help interpret the experimental results of Chapter 11. In this section, we introduce the gyrokinetic equation and discuss briefly how it is solved using the code GS2 [69].

1.7.1 The gyrokinetic equation

A full derivation of the gyrokinetic equation is available in [70]. In the low-Mach-number ($M \equiv v_\zeta / v_{\mathrm{th}i} \ll 1$) and electrostatic ($\delta B = 0$) limits, the gyrokinetic equation takes the form:

$$\begin{aligned}\underbrace{\frac{\partial h_s}{\partial t}}_{1} \;+\; & \underbrace{\mathbf{u}\cdot\frac{\partial h_s}{\partial \mathbf{R}_s}}_{2} + \underbrace{v_\parallel \mathbf{b}\cdot\frac{\partial h_s}{\partial \mathbf{R}_s}}_{3} + \underbrace{\mathbf{V}_{Ds}\cdot\frac{\partial h_s}{\partial \mathbf{R}_s}}_{4} + \underbrace{\langle \mathbf{V}_E\rangle_{R_s}\cdot\frac{\partial h_s}{\partial \mathbf{R}_s}}_{5} - \underbrace{\langle C_L[h_s]\rangle_{R_s}}_{6} \\ = \; & \underbrace{\frac{Z_s e F_{0s}}{T_s}\frac{\partial\langle\delta\varphi\rangle_{R_s}}{\partial t}}_{7} + \underbrace{\frac{Z_s e F_{0s}}{T_s}\mathbf{u}\cdot\frac{\partial\langle\delta\varphi\rangle_{R_s}}{\partial \mathbf{R}_s}}_{8} \\ & - \left[\underbrace{\frac{\partial F_{0s}}{\partial\psi}}_{9} + \underbrace{\frac{m_s I(\psi) v_\parallel F_{0s}}{T_s B}\frac{\mathrm{d}\omega}{\mathrm{d}\psi}}_{10}\right]\langle\mathbf{V}_E\rangle_{R_s}\cdot\nabla\psi. \end{aligned} \tag{1.6}$$

It describes the evolution of h_s, the fluctuating part of the distribution function that is independent of the gyrophase, i.e., h_s only depends on the three spatial coordinates and two velocity coordinates: parallel and perpendicular to the field. The third velocity coordinate, the gyrophase, which describes the angle in velocity space of

[2]Unless an extension has been made, fluid models, such as magnetohydrodynamics (MHD), do not include the trapped-particle or finite-gyroradius effects, which can cause both new instabilities and increased damping, respectively.

the perpendicular velocity, is averaged over, as the frequency at which this changes is taken to be asymptotically higher than all other frequencies in the problem (this gyroaverage is denoted using $\langle ... \rangle_{R_s}$).

The second term in (1.6) describes the advection of h_s by the bulk (toroidal and poloidal) velocity of the plasma, $\mathbf{u}$, and where $\mathbf{R}_s$ is the position of the gyrocentre (guiding centre of a particle). The third term represents the parallel drift of particles with velocity $v_\parallel$ along the field lines, with unit vector $\mathbf{b} = \mathbf{B}/B$. The fourth term includes the effect of the drift velocities, $\mathbf{V}_{Ds}$, of the particles due to inhomogeneities in the magnetic field. In the fifth term $\mathbf{V}_E = \frac{c}{B}(\mathbf{b} \times \nabla \delta\varphi)$ is the $\mathbf{E} \times \mathbf{B}$ velocity of the fluctuating electric field, with c the speed of light. This describes the nonlinear interaction between h_s and the fluctuating part of the electric potential $\delta\varphi$, which is related to h_s through quasi-neutrality

$$\sum_s \frac{Z_s^2 e^2 n_s \delta\varphi}{T_s} = \sum_s Z_s e \int \mathrm{d}^3\mathbf{v} \langle h_s \rangle_{r_s}, \tag{1.7}$$

where the sums are over all species, s, the integral is over all velocity space, $\mathbf{v}$, the gyroaverage $\langle ... \rangle_{r_s}$ is evaluated at the particle position $\mathbf{r}_s = \mathbf{R}_s + \mathbf{b} \times \mathbf{v}_\perp / \Omega_s$, not the guiding centre position, $Z_s e$ is the charge on the species, n_s is the unperturbed density of the species, and T_s is the unperturbed (Maxwellian) temperature of the species.

The sixth term in (1.6) is the linearised collision operator, which models small angle collisions between particles whilst conserving number (no fusion of particles is included), momentum and energy . The seventh and eighth terms represent the Boltzmann response of the plasma, with F_{0s} the Maxwellian distribution. The ninth and tenth terms are sources of free energy for the system. The ninth term is the gradient of the background Maxwellian across a flux surface labelled by ψ, and can be written in terms of temperature and density gradients. The tenth term is the source of the PVG instability, where $I(\psi)$ is the toroidal magnetic field flux function.

For the analysis performed in this thesis, we are only interested in three quantities: the fluctuating density field, which is calculated by taking the zeroth moment of h_s:

$$\frac{\delta n_s}{n_s} = \int h_s \mathrm{d}^3\mathbf{v} \Big/ \int F_{0s} \mathrm{d}^3\mathbf{v}; \tag{1.8}$$

the fluctuating radial velocity field [71]

$$\delta v_r = \overline{\langle \mathbf{V}_E \rangle_{R_s} \cdot \nabla\psi}, \tag{1.9}$$

and the turbulent (ion) heat flux

$$Q_i = \overline{\int \mathrm{d}^3\mathbf{v} \frac{1}{2} m_i v^2 \langle h_i \rangle_{r_s} \mathbf{V}_E \cdot \frac{\nabla\psi}{|\nabla\psi|}}, \tag{1.10}$$

where the overline is a spatial and temporal average.

1.7.2 Solving the gyrokinetic equation

There are two main approaches used for solving the gyrokinetic equation. The first is an implicit method that solves an initial-value problem for the distribution function and electrostatic potential on a discrete grid of points [69, 71]. The second is the particle-in-cell (PIC) method [72], where the positions and velocities of 'super-particles' are calculated at each time step under the action of the Lorentz force. The electric and magnetic fields are calculated on a discrete grid, with values updated from the distribution of the super-particles and the process iterated.

Each method has its own advantages and disadvantages, as well as a myriad of subtleties in the implementations of specific codes. One key issue is how to deal with boundary conditions in the simulation domain, which broadly fall into one of two categories: global or local. Global simulations attempt to simulate the entire torus, whilst local simulations identify a specific 'flux tube' of interest where equilibrium gradients can be assumed constant. Generally, PIC codes are of the global type, whilst initial-value codes use the local-flux-tube approach (though a few of these codes have been extended to also be global). The advantage of the local approach is that the boundary conditions are taken to be periodic, whilst, in the global approach, assumptions have to be made as to how the plasma interacts with neutral particles at edge of the plasma and with the wall. The code, GS2, used in this work is of the local type, which solves the initial-value problem[3].

The quantities of interest (1.8-1.10) are outputted by the code GS2, which solves (1.6) for h_s and $\delta\varphi$ on a grid in Fourier space for the spatial coordinates perpendicular to the magnetic field and in real space for the direction parallel to the magnetic field, and for the two velocity coordinates. A coordinate transformation is performed that maps the fields from the plasma frame (see Section 3.1), in which they are solved, to the laboratory frame (Section 3.2), so that then they can be compared with experiment.

1.8 Structure of this work

This thesis is organised as follows. In Part II, we focus on the measurement of the correlation parameters of the turbulent field. We start, in Chapter 2, by describing the how the density field is related to the intensity field via the point-spread functions (PSFs) of the BES system, and how we measure the correlation parameters of the intensity field from the BES signal. Then, in Chapter 3, we derive the relation between the correlation parameters in the plasma frame (which is the physical field we

[3]The non-linear term is incorporated as a source for the initial-value solver at each time step.

are interested in) and in the laboratory frame, which, in the absence of PSF effects, would fully describe how to reconstruct the plasma-frame correlation parameters. In Chapter 4, we discuss how the PSFs are calculated, taking our examples from the BES system on MAST, characterising the PSFs using principal-component analysis, and introducing a simplified Gaussian model of the PSFs. These Gaussian-model PSFs are then used in Chapter 5 to calculate analytically the effect of the PSFs on the measured laboratory-frame correlation parameters. The validity of these calculations are tested in Chapter 6 by comparing them to the correlation parameters measured from synthetic-BES data generated numerically using a model of a fluctuating density field. Having established that this comparison is reasonably successful, in Chapter 7 we present equations that allow one to reconstruct the plasma-frame spatial correlation parameters and the fluctuation amplitude from BES measurements, and we test successfully this reconstruction procedure using a gyrokinetic simulation of MAST turbulence. In Chapter 8, we find that the PSFs have an effect also on the measurement of the correlation time and establish that this can be due to the presence of a fluctuating radial component of velocity. Then, in Chapter 9, we summarise, and discuss the implications of, the results of Part II.

In Part III, the results of Part II are used to investigate the effect of flow shear on the structure of ion-scale turbulence in MAST. The effect of flow shear is interpreted by considering the symmetry properties of the gyrokinetic equation (1.6), which are discussed in Chapter 10. In Chapter 11, we consider three experimental cases that illustrate the effect of flow shear. In Chapter 12, the same analysis as has been performed on the experimental data in Chapter 11 is repeated on the turbulent density field from gyrokinetic simulations, the results of which are used to gain a more detailed (and more physical) understanding, through studies varying both the flow shear and the ion-temperature gradient systematically, how these two parameters affect the skewness of the distribution of δn and the tilt of its correlation function. In Chapter 13, we summarise the findings, with a discussion of their implications. Finally, in Chapter 14, we present the conclusions of this thesis and possible directions of future work.

Technical details are given in the Appendices. In Appendix A, we test our improved method for measuring the poloidal correlation length. In Appendix B, we present the model of fluctuating fields that we use for the tests in Chapter 6. In Appendix C, we calculate the correlation time and apparent poloidal velocity inferred from our assumed form of the correlation function. In Appendix D, we quantify the differences between the real and Gaussian-model PSFs. In Appendix E, we discuss spurious sources of skewness in the experimentally measured distributions of the fluctuating intensity field, as well as the effect of the PSFs on this distribution.

1.9 Author's contributions

1.9.1 Published papers

[73]: M F J Fox, A R Field, A A Schekochihin, F van Wyk and the MAST Team, 2017 Plasma Phys. Control. Fusion accepted (ArXiv:1609.09534).

[74]: M F J Fox, F van Wyk, A R Field, Y-c Ghim, F I Parra, A A Schekochihin and the MAST Team, 2017 Plasma Phs. Control. Fusion 59 034002 (ArXiv:1609.08981).

Part II of this Thesis is largely based on [73] and Part III is based on [74]. The author of this work has created the model of fluctuating fields (Chapter 6), derived the expressions to correct for PSF effects (Chapter 7), and performed the data analysis on the model fields (Part II), the BES data in Chapter 11 and the gyrokinetic simulation data in Chapter 12.

The software to generate the PSFs was written by Y.-c. Ghim. The BES system was designed, installed and operated by A. R. Field, D. Dunai, and S. Zoletnik. C. Michael generated the EFIT data. F. van Wyk performed the gyrokinetic simulations used in Chapters 7 and 12. Theoretical insights have been provided by A. A. Schekochihin, F. I. Parra, M. Barnes, and E. G. Highcock.

1.9.2 Conference submissions

2015

Princeton Plasma Physics Lab, Princeton, NJ, USA (seminar)

APS, DPP Conference: Savannah, GA, USA (poster)

European Fusion Theory Meeting: Lisbon, Portugal (poster)

Culham PhD Showcase: Culham, UK (presentation)

2014

Wigner Institute: Budapest, Hungary (seminar)

EU-US Transport Task Force Meeting: Culham, UK (poster)

Gyrokinetic Theory Working Group Meeting: Madrid, Spain (presentation)

EPS Conference on Plasma Physics: Berlin, Germany (poster)

2013

International Spherical Torus Workshop: York, UK (poster)

Part II

Measuring turbulence using Beam-Emission Spectroscopy

CHAPTER 2

Introduction and measurement methods

The link between theory and experiment is made through the spatial and temporal correlation functions of the turbulent fields, which are often characterised using correlation lengths and times. However, correlation functions of experimentally measured fluctuating quantities are not directly comparable to the correlation functions of the physical fields that we are interested in. Thus, Beam-Emission-Spectroscopy (BES) systems [64, 75, 76, 77, 54, 78] measure the fluctuating intensity, δI_i, of the Doppler-shifted D_α emission from excited neutral beam atoms, which is nontrivially related to the density field in the plasma via the Point-Spread Functions (PSFs) of the diagnostic [23], see Figure 2.1,

$$\delta I_i = \int P_i(r - r_i, Z - Z_i)\beta\delta n(r, Z)\mathrm{d}r\mathrm{d}Z, \tag{2.1}$$

where $\delta n(r, Z)$ is the fluctuating (laboratory-frame) density field inside the plasma at the focal plane of the BES optics, r and Z are the radial and poloidal coordinates, respectively, $P_i(r-r_i, Z-Z_i)$ is the PSF for channel i with focal point at (r_i, Z_i) and β is a coefficient weakly dependent on the atomic physics of the line emission [66, 65] ($\beta = 1$ is assumed throughout Part II of this thesis [23]). The physical field we are interested in is the plasma-frame density field, which can be reached from the laboratory-frame density field by a transformation into field-aligned and rotating (with the mean plasma flow) coordinates. It is clear from (2.1) that if the PSFs are taken to be delta functions then the measured intensity will be directly proportional to the density field in the laboratory frame. However, the PSFs of BES systems have typical widths greater than the ion gyro-radius, ρ_i, and, therefore, are of a similar size to the ion-scale turbulence that is being measured. This raises the following two questions, which will be answered in this part of the thesis:

1. What is the difference between the correlation parameters of the density field in the plasma frame (P), namely, the radial, $\ell_{x|P}$, and binormal, $\ell_{y|P}$, correlation lengths, the radial, $k_{x|P}$, and binormal, $k_{y|P}$, wavenumbers, the correlation time, $\tau_{c|P}$, and the root-mean square (RMS) fluctuation amplitude, $\overline{\delta n/n}$, and the respective correlation parameters of the intensity field measured by the BES system (B): the radial, $\ell_{r|B}$, and poloidal, $\ell_{Z|B}$, correlation lengths, the radial, $k_{r|B}$, and poloidal, $k_{Z|B}$, wavenumbers, the correlation time, $\tau_{c|B}$, and the

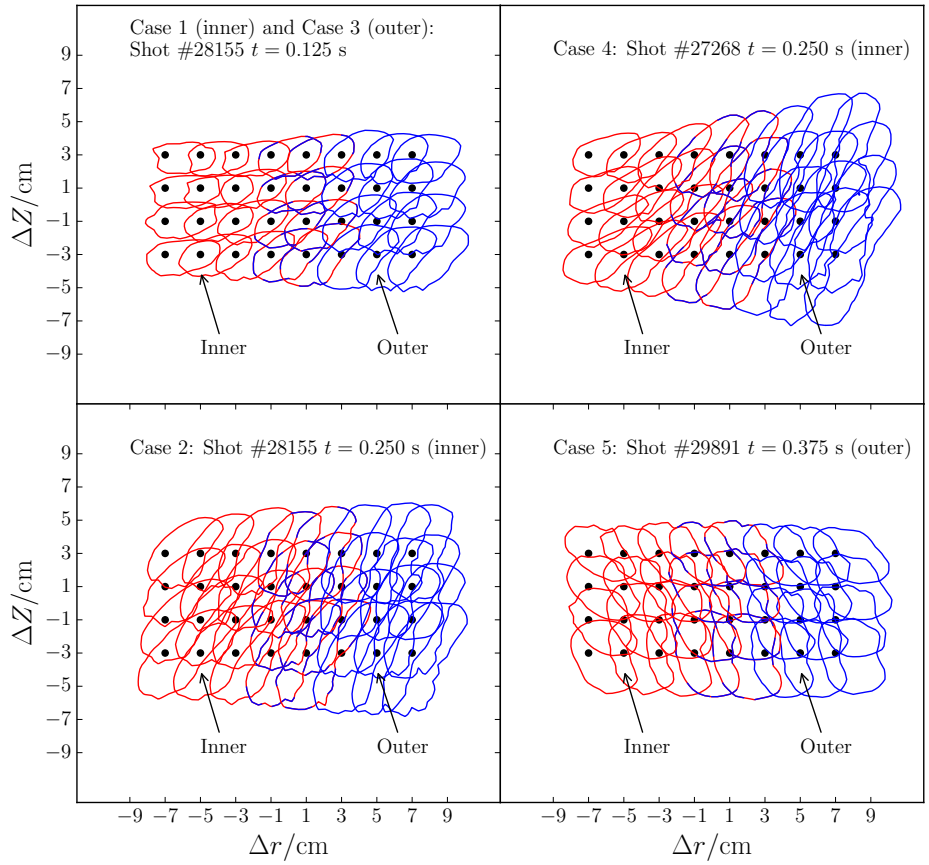


Figure 2.1: Example e^{-1} amplitude contours of PSFs [66] for five specific cases taken from MAST shots and described in Section 4.3. The dots mark the locations of the focal points of the detector channels.

RMS fluctuation amplitude, $\overline{\delta I/I}$? I.e., what is the effect of the PSFs?

2. Given BES measurements of the intensity field's correlation parameters, is it possible to reconstruct the plasma-frame correlation parameters of the density field?

The rest of this part of the thesis is focused on answering these questions. To proceed, we first describe, in Section 2.1, how the correlation parameters of the intensity field are measured from the BES signal.

2.1 Correlation parameters of the measured BES signal

A BES system consists of an array of detector channels each of which receives photons from a spatially localised region within the plasma. This region is assumed

to lie in a plane described by the radial r and poloidal Z coordinates (the plane of detection). BES systems are designed to resolve fluctuations that vary on the turbulent-fluctuation timescale of a few microseconds. Therefore, both spatial and temporal properties of the turbulence can be investigated. In this section, we describe the operational definitions of the parameters that characterise the correlation function of the signals detected by a BES diagnostic.

Each BES detector channel i measures the intensity of photons as a function of time,

$$I_i(t) = \langle I_i(t) \rangle + \delta I_i(t), \tag{2.2}$$

where we have split the signal into its temporal mean $\langle I_i(t) \rangle$ and fluctuating part $\delta I_i(t) \equiv I_i(t) - \langle I_i(t) \rangle$. The detector channel i can be associated with a viewing location in the radial-poloidal plane given by the coordinates (r_i, Z_i), which are determined by the focal point of the optical system for that channel.

All the parameters of the turbulence that we will be considering are determined from measurements of the covariance function of the fluctuating part of the time series. The covariance between two detector channels (i, j) is defined as

$$C_{ij}^{\mathrm{cov}}(\Delta t) = \frac{\langle \delta I_i(t) \delta I_j(t + \Delta t) \rangle}{\langle I_i(t) \rangle \langle I_j(t + \Delta t) \rangle}, \tag{2.3}$$

where Δt is the time delay between the signals. Thus, the covariance function is a function of the time delay Δt and of the spatial separation of the two channels $(\Delta r_{ij}, \Delta Z_{ij}) = (r_i - r_j, Z_i - Z_j)$. When the auto-covariance ($i = j$) is calculated, (2.3) needs to be corrected for auto-correlated photon noise, as described in [23] and Section 11.4. The correlation function is defined as the normalised covariance function

$$C_{ij}(\Delta t) = \frac{\langle \delta I_i(t) \delta I_j(t + \Delta t) \rangle}{\sqrt{\langle \delta I_i^2(t) \rangle \langle \delta I_j^2(t + \Delta t) \rangle}}. \tag{2.4}$$

2.1.1 Fluctuation amplitude

The fluctuation amplitude of the signal is the square root of the mean, over a set of N channels, of the auto-covariance function (2.3) at $\Delta t = 0$,

$$\overline{\delta I / I} \equiv \sqrt{\frac{1}{N} \sum_{i=1}^{N} \frac{\langle \delta I_i^2(t) \rangle}{\langle I_i(t) \rangle^2}} = \sqrt{\frac{1}{N} \sum_{i=1}^{N} C_{ii}^{\mathrm{cov}}(0)}. \tag{2.5}$$

2.1.2 Correlation time

The standard technique [79, 23] for extracting a correlation time from BES measurements relies on the toroidal rotation of the plasma with velocity v_ζ to advect turbulent structures, which are field-aligned and anisotropic [20, 21, 22] (the correlation

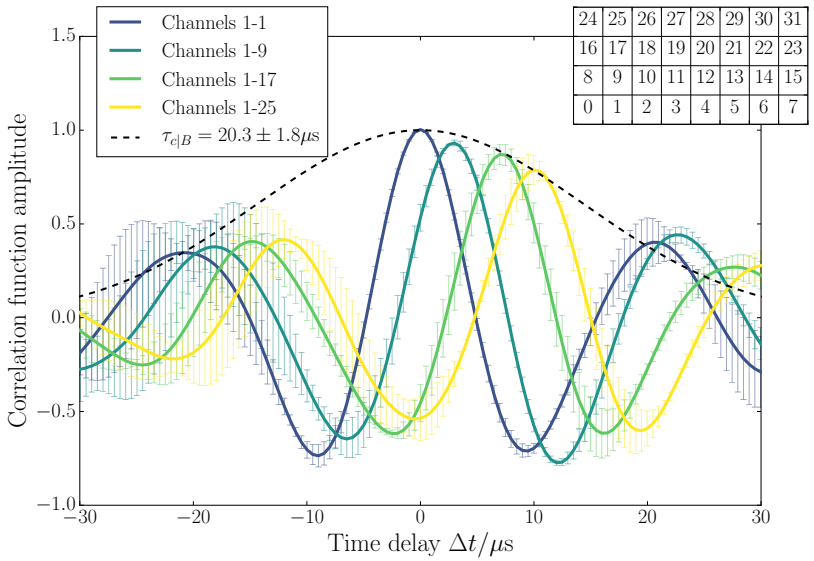


Figure 2.2: Time delay auto- and cross-correlation functions taken from shot #28155 at $t = 126$ ms using channels 1, 9, 17 and 25, with channel 1 as the reference channel (see inset for their positions in the BES array). The black dashed line is the result of the CCTD technique where (2.7) is fit to the global maxima (peaks) of the cross-correlation functions.

length parallel to the magnetic field is much greater than the perpendicular lengths), past the plane of detection. The structures, therefore, appear to move in the poloidal direction in the plane of detection with velocity $v_\zeta \tan\alpha$, where $\alpha = \arctan(B_Z/B_\zeta)$ is the pitch angle of the magnetic field, with B_Z the poloidal and B_ζ the toroidal components of the magnetic field. Provided that the minimum passing time of a turbulent structure, $\tau_{\min} = \Delta Z_{\min}/(v_\zeta \tan\alpha)$, where $\Delta Z_{\min}$ is the minimum poloidal distance between detector channels, is less than the correlation time of the turbulence, the turbulent structure will be seen to decay as it passes multiple detector channels.

By considering the correlation function between poloidally, but not radially, separated detector channels (such that $\Delta r_{ij} = 0$), the decay in the amplitude can be observed, an example of which is shown in Figure 2.2. To measure this decay, we first identify the amplitude, $A_{\text{peak}|B}(\Delta Z_{ij})$, and the time delay, $\Delta t_{\text{peak}|B}(\Delta Z_{ij})$, of the peak of the time-delay correlation function, $C(\Delta Z_{ij}, \Delta t)$, for each value of poloidal separation, ΔZ_{ij}, by fitting the function

$$f_{\text{peak}}(\Delta t) \equiv A_{\text{peak}|B}(\Delta Z_{ij}) \exp\left(-\frac{[\Delta t - \Delta t_{\text{peak}|B}(\Delta Z_{ij})]^2}{\tau_{\text{eff}}^2}\right) \tag{2.6}$$

to the data points selected in the vicinity of the peak, where the fitting parameter τ_{eff} is an effective decay time of the peak. We have introduced the subscript B to iden-

tify parameters that describe the covariance/correlation properties of the measured intensity field (i.e., the BES signal). Then, using the pairs of amplitudes and time delays $(A_{\mathrm{peak}|B}(\Delta Z_{ij}), \Delta t_{\mathrm{peak}|B}(\Delta Z_{ij}))$ for each ΔZ_{ij}, we find the correlation time of the BES-measure intensity signal, $\tau_{c|B}$, by minimising

$$\chi^2 = \sum_{\Delta Z_{ij}} \left[A_{\mathrm{peak}|B}(\Delta Z_{ij}) - \exp\left(-\frac{\Delta t^2_{\mathrm{peak}|B}(\Delta Z_{ij})}{\tau^2_{c|B}} \right) \right]^2 . \tag{2.7}$$

This technique is known as the cross-correlation time-delay (CCTD) method [79] and the parameter $\tau_{c|B}$ can be considered, by definition, to be the correlation time of the BES signal, although, as we will see, the interpretation of this in terms of physical turbulent fields is complicated (see Chapter 8 and Appendix C.1).

2.1.3 Apparent poloidal velocity

Using the CCTD technique, it is also possible to measure the apparent poloidal velocity, given that we know the distances between the viewing locations of the detector channels ΔZ_{ij}, and the time delays of the peaks $\Delta t_{\mathrm{peak}|B}(\Delta Z_{ij})$ of the cross-correlation functions. Then,

$$v_{\mathrm{pol}|B} \equiv \frac{\Delta Z_{ij}}{\Delta t_{\mathrm{peak}|B}}, \tag{2.8}$$

assuming that neither the toroidal velocity nor pitch angle change during the measurement time.[1] Practically, as multiple values of ΔZ_{ij} are available, a linear fit is used to find $v_{\mathrm{pol}|B}$. The efficacy of this measurement method is supported by successful cross-diagnostic comparisons with charge-exchange recombination spectroscopy [23] and, more recently, with Doppler backscattering [55].

2.1.4 Two-dimensional spatial correlation parameters

We now consider the spatial properties of the correlation function (2.4) by setting the time delay to zero, $\Delta t = 0$. We also make the assumption that the turbulence is homogeneous, drop the indices i, j, and treat the correlation function as a function of Δr and ΔZ only. In order to extract the spatial correlation parameters, the following function, which is similar in form to that used in [80], is fitted to the correlation function (2.4):

$$C_{\mathrm{fit}}(\Delta r, \Delta Z) = p + (1-p) \exp\left(-\frac{\Delta r^2}{\ell^2_{r|B}} - \frac{\Delta Z^2}{\ell^2_{Z|B}} \right) \cos(k_{r|B}\Delta r + k_{Z|B}\Delta Z), \tag{2.9}$$

where $\ell_{r|B}$ is the radial correlation length, $\ell_{Z|B}$ is the poloidal correlation length, $k_{r|B}$ is the radial wavenumber, and $k_{Z|B}$ the poloidal wavenumber. The parameter p is used with experimental data to account for offsets caused by global MHD

[1] We use $v_{\mathrm{pol}|B}$ here to distinguish this apparent velocity, mainly due to $v_\zeta \tan\alpha$, from the 'true' poloidal velocity v_Z, which we introduce later in Section 3.1.

modes [23] or beam-fluctuation effects [81]. The choice of the function (2.9) is purely empirical. Similar functional forms, which may have a more physical motivation, such as a Lorentzian function [82], could have been used, however, the mathematical properties of the Gaussian function prove to be useful later in this Thesis (see Appendices B and C). We also define, for later convenience, the tilt angle of the correlation function as

$$\Theta_B = -\arctan\left(\frac{k_{r|B}}{k_{Z|B}}\right). \tag{2.10}$$

As the spatial distribution of viewing locations is often sparse for BES systems (the MAST BES has only 8×4 radial-poloidal channels), the fit of (2.9) to the measured correlation function (2.4) can be insufficiently constrained. Therefore, we impose a further constraint by fixing the product $k_{Z|B}\ell_{Z|B}$ in the above fitting procedure. The value of this product is determined from the shape of the time-delayed auto-correlation function, using the fact that a turbulent perturbation is advected past a single detector channel by the bulk velocity of the plasma (Section 2.1.2), therefore encoding the spatial structure of the perturbation in the temporal domain of the detected signal [83, 84].

The procedure for determining $k_{Z|B}\ell_{Z|B}$ is as follows. First we measure the correlation time $\tau_{c|B}$ as described in Section 2.1.2. Then we calculate the time-delayed auto-correlation function (2.4) and multiply it by the correction factor $\exp(\Delta t^2/\tau_{c|B}^2)$, which accounts for the fact that the amplitude of the turbulence decays in time, so that the resulting corrected auto-correlation function only includes information about the decay due to the poloidal correlation length. Finally, the following function is fitted to this corrected auto-correlation function (see discussion in Appendix A and Section 3.2.2):

$$C_{\text{auto}}(\Delta t) = \exp\left[-\frac{v_\zeta^2 \Delta t^2 \tan^2\alpha}{\ell_{Z|B}^2}\right]\cos\left(k_{Z|B} v_\zeta \Delta t \tan\alpha\right), \tag{2.11}$$

$$= \exp\left[-\frac{\Delta t^2}{\ell_{Z|B}'^2}\right]\cos\left(k'_{Z|B}\Delta t\right), \tag{2.12}$$

where the primed quantities are the fitting parameters, which have the property that $k'_{Z|B}\ell'_{Z|B} = k_{Z|B}\ell_{Z|B}$ and, therefore, the requirement to know $v_\zeta \tan\alpha$ is eliminated. This method is tested successfully in Appendix A using our model of a fluctuating density field (described in Section 6.1 and Appendix B).

Spatial correlation parameters from the MAST BES

The BES system on MAST has a set of 32 channels arranged into an 8×4 radial-poloidal array, with spacing between channels of approximately $2\ \text{cm}$. As this BES array covers almost a quarter of the minor radius of the tokamak, it is not expected

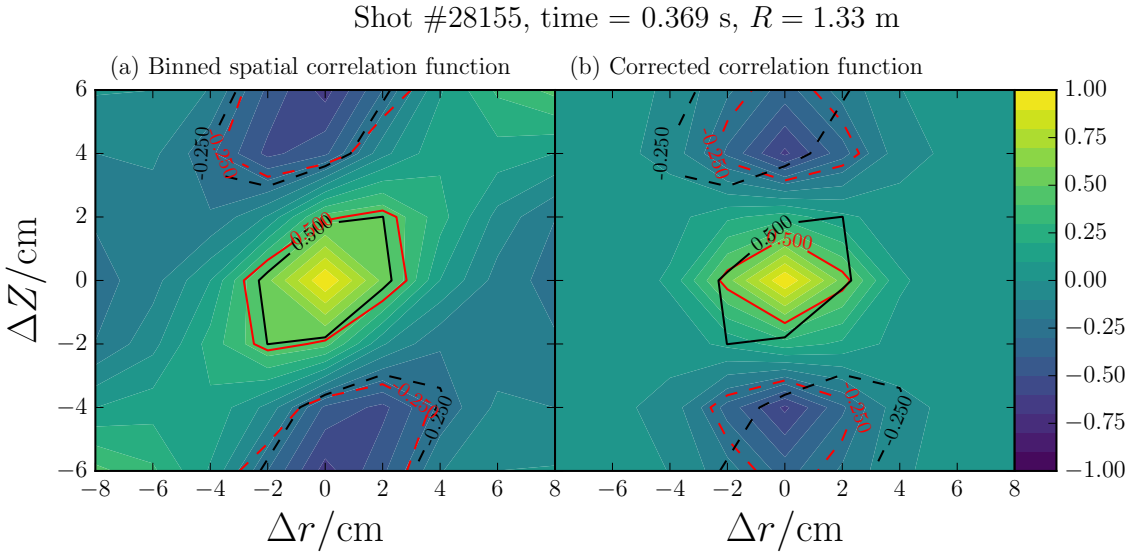


Figure 2.3: (a) The zero-time-delay binned spatial correlation function (see Section 2.1.4) of the BES intensity signal in MAST shot #28155 at $t = 0.369$ s plotted using the outer set of channels. The red contours show the fit (2.9) to the data. (b) The corrected correlation function using (7.1-7.5) and the PSF parameters $L_1 = 3.1$ cm, $L_2 = 1.5$ cm, and $\alpha_{\text{PSF}} = -24°$ (defined in Section 4.2). These PSF parameters are similar to those of Case 2, described in Section 4.3 and shown in Figure 2.1. In (b) the black contour line is the same as that in (a), the red contour line is for the corrected parameters. The fitted and corrected parameter values are given in Table 2.1. The results in this figure are used in Chapter 11.

Parameter	ℓ_r/cm	ℓ_Z/cm	k_r/cm^{-1}	k_Z/cm^{-1}	Θ/deg
(a) BES fit value	3.7 ± 0.5	8.6 ± 0.7	-0.20 ± 0.07	0.53 ± 0.01	21 ± 7
(b) Corrected value (lab)	2.6 ± 0.7	7.7 ± 0.8	0.03 ± 0.20	0.66 ± 0.03	-2 ± 17

Table 2.1: Fitting parameters, using (2.9), for Figure 2.3.

that the turbulence is precisely homogeneous across the entire array. Therefore, we split it into two radial-poloidal subarrays of 5×4 channels each, referred to here as "inner" and "outer" arrays.

A complete set of spatial correlation functions (2.4) for a single subarray can be represented by a 20×20 matrix. In order to visualise this matrix, it is necessary to associate spatial coordinates with each matrix element. As the spacing between BES channels is uniform, and we are assuming that the turbulence is homogeneous, a single pair of relative coordinates $(\Delta r, \Delta Z)$ can correspond to multiple values in the spatial-correlation-function matrix. To resolve this problem, a binned spatial correlation function is constructed by averaging over all values of the spatial correlation function matrix that have the same relative coordinates. An example binned corre-

lation function is shown in Figure 2.3(a). The slight difference between the binned correlation function contours and the contours of the fit (2.9), shown in red, is due to the fact that this fit, along with all others in this work, has been made to the complete set of values of the spatial correlation function, with no binning.

As stated in Chapter 1, the nature of turbulence depends on the local equilibrium parameters. The strong radial variation of the equilibrium profiles (see, for example Figure 11.1) suggests that the resulting turbulence will also vary with radius, and is, therefore, not homogeneous. In this case, by performing the fit with (2.9) to the two-dimensional spatial correlation function, the resulting turbulence parameters can be considered to be radially-averaged values.

CHAPTER 3

Correlation parameters of the physical density field

The physical field of interest is the ion number density. The correlation function of this field is most easily described in the plasma frame, which will be defined in Section 3.1. In Section 3.2, the transformation of correlation parameters from the plasma frame to the laboratory frame (that of the experimental observer) is made. The correlation parameters of the density field in the laboratory frame would be equivalent to those of the intensity field measured by a BES system if the PSFs in (2.1) were delta functions. However, as we will show, making this assumption is rarely justified, and, therefore, the distinction between the laboratory-frame and BES measurements is emphasised here: the "laboratory frame" refers specifically to the correlation properties of the density field, whilst BES measurements are of the correlation properties of the intensity field.

3.1 Plasma frame

The plasma frame is a coordinate system aligned with the magnetic field and moving with the mean velocity of the plasma, i.e., rotating with the toroidal v_ζ and poloidal v_Z plasma velocities. The coordinates (x, y, z) describe the spatial position of a plasma element in this frame in the radial $(\hat{\mathbf{x}})$, binormal $(\hat{\mathbf{y}})$ and parallel to the magnetic field $(\hat{\mathbf{z}})$ directions. We assume that the correlation function of the turbulent density field in these coordinates can be fitted by[1]

$$C_P(\Delta x, \Delta y, \Delta z, \Delta t) = \exp\left(-\frac{\Delta x^2}{\ell_{x|P}^2} - \frac{\Delta y^2}{\ell_{y|P}^2} - \frac{\Delta z^2}{\ell_{z|P}^2} - \frac{\Delta t^2}{\tau_{c|P}^2}\right) \cos\left(k_{x|P}\Delta x + k_{y|P}\Delta y\right), \tag{3.1}$$

where $\ell_{x|P}$ is the radial correlation length, $\ell_{y|P}$ is the binormal correlation length, $\ell_{z|P}$ is the parallel correlation length, $\tau_{c|P}$ is the correlation time, $k_{x|P}$ is the radial wavenumber and $k_{y|P}$ is the binormal wavenumber. We have used the subscript P to label correlation parameters defined in the plasma frame.

[1] We assume there is no oscillatory structure in the parallel direction: $k_{z|P} = 0$; and note that the inclusion of a finite $k_{z|P}$ should not considerably alter our results, as it will be ordered (see Section 3.2.3) the same size as $\ell_{z|P}^{-1}$, which is small compared to the lengths $\ell_{x|P}^{-1}$ and $\ell_{y|P}^{-1}$.

3.2 Laboratory frame

In the laboratory frame, we measure a fluctuating time series in a radial-poloidal cross-section described by the coordinates (r, Z). Therefore, as well as transforming out of the plasma frame, we also have to consider the projection onto this two-dimensional plane. In Appendix B.3, the full expression (B.39) for the laboratory-frame correlation function $C_L(\Delta r, \Delta Z, \Delta t)$ is given. For clarity, here we consider the spatial and temporal laboratory-frame correlation functions separately, in order to relate measurable parameters in the laboratory frame to the plasma-frame parameters.

3.2.1 Spatial correlation function

The spatial laboratory-frame correlation function defined from (B.39) as $C_{\text{spatial}|L}(\Delta r, \Delta Z) \equiv C_L(\Delta r, \Delta Z, \Delta t = 0)$, can be written in the form

$$C_{\text{spatial}|L}(\Delta r, \Delta Z) = \exp\left(-\frac{\Delta r^2}{\ell_{r|L}^2} - \frac{\Delta Z^2}{\ell_{Z|L}^2}\right) \cos\left(k_{r|L}\Delta r + k_{Z|L}\Delta Z\right), \tag{3.2}$$

where the relationships of the laboratory-frame correlation parameters to the plasma-frame correlation parameters of (3.1) are

$$\ell_{r|L} = \ell_{x|P}, \tag{3.3}$$

$$\ell_{Z|L} = \left(\frac{\cos^2\alpha}{\ell_{y|P}^2} + \frac{\sin^2\alpha}{\ell_{z|P}^2}\right)^{-1/2}, \tag{3.4}$$

$$k_{r|L} = k_{x|P}, \tag{3.5}$$

$$k_{Z|L} = k_{y|P}\cos\alpha, \tag{3.6}$$

and we have introduced the subscript label L to identify the laboratory-frame parameters. The correlation function (3.2) has the same functional form as the fit function (2.9), used to extract the BES correlation parameters (with $p = 0$).

3.2.2 Temporal correlation function

The time-delayed, single-point auto-correlation function defined from (B.39) as $C_{\text{temporal}|L}(\Delta t) \equiv C_L(\Delta r = 0, \Delta Z = 0, \Delta t)$, is

$$C_{\text{temporal}|L}(\Delta t) = \exp\left(-\frac{\Delta t^2}{\tau_{\text{auto}}^2}\right) \cos\left(k_{y|P}v_\zeta\Delta t\sin\alpha + k_{y|P}v_Z\Delta t\cos\alpha\right), \tag{3.7}$$

where

$$\tau_{\text{auto}} \equiv \left[\frac{(v_\zeta\sin\alpha + v_Z\cos\alpha)^2}{\ell_{y|P}^2} + \frac{(v_\zeta\cos\alpha + v_Z\sin\alpha)^2}{\ell_{z|P}^2} + \frac{1}{\tau_{c|P}^2}\right]^{-1/2}, \tag{3.8}$$

is a function of the spatial correlation parameters as well as of the plasma-frame correlation time $\tau_{c|P}$. The functional form of $C_{\text{temporal}|L}$ above is different from the

C_{auto} in (2.11), because in (2.11) we have only kept the lowest-order (see Section 3.2.3) contributions to the full temporal correlation function (3.7).

The CCTD method (see Section 2.1.2) attempts to remove the spatial terms in (3.8) by assuming that the spatial properties of the turbulence remain constant in time and, therefore, the difference in the peak amplitudes of the time-delayed cross-correlation functions is only due to the temporal decorrelation. The correlation time resulting from the CCTD method is $\tau_{c|L}$. To interpret this correlation time, we have to find the relationship between $\tau_{c|L}$ and the plasma-frame correlation time $\tau_{c|P}$. To do this, we can simply find the maximum of the time-delayed cross-correlation function (B.39) at a fixed poloidal displacement ΔZ and with $\Delta r = 0$. However, it is informative, and will become useful for later discussions in Chapter 8, to approach the problem by using an asymptotic expansion based on the typical time and spatial scales of the problem.

3.2.3 Asymptotic ordering for the CCTD method

We start by assuming that the ion gyroradius ρ_i is small compared to the minor radius of the tokamak a, providing us with the small parameter

$$\epsilon \equiv \frac{\rho_i}{a}, \tag{3.9}$$

which is just the gyrokinetic ordering [70]. The perpendicular correlation lengths of the turbulence have been measured to be typically of order a few ion gyroradii (see Figure 2.3, where $\rho_i = 1.1\ \mathrm{cm}$), i.e., $\ell_{x|P}, \ell_{y|P} \sim \rho_i$, while the parallel correlation length is significantly longer $\ell_{z|P} \sim a$ [20, 21, 22]. Therefore, we order the perpendicular spatial correlation lengths to be shorter than the parallel correlation length: $\ell_{x|P}, \ell_{y|P} \sim \epsilon \ell_{z|P}$. The poloidal velocity is ordered to be smaller than the toroidal velocity $v_Z \sim \epsilon v_\zeta$ [29, 85, 35]. The toroidal velocity is taken to be the same order of magnitude as the thermal velocity, $v_{\mathrm{th}i} = \sqrt{2T_i/m_i}$, where T_i is the ion temperature, and m_i is the ion mass. This then leaves space for a subsidiary expansion in low-Mach number $M \equiv v_\zeta / v_{\mathrm{th}i}$, which will be performed in Section 3.2.5.

We relate the lengths, times and velocities to each other by noting that the poloidal displacement of a perturbation ΔZ scales with the toroidal velocity and laboratory-frame time delay of the peak of the cross-correlation function $\Delta t_{\mathrm{peak}|L}$: $\Delta Z \sim v_\zeta \Delta t_{\mathrm{peak}|L}$, and that this poloidal displacement is typical of the perpendicular correlation lengths $\ell_{x|P}$ and $\ell_{y|P}$. In addition to this, we use the critical balance conjecture [27, 28, 86] to relate the parallel correlation length to the thermal velocity and the plasma-frame correlation time $\ell_{z|P} \sim v_{\mathrm{th}i} \tau_{c|P}$. Critical balance is an assumption that the length of a correlated structure parallel to the magnetic field is determined by the time taken for the structure to decorrelate in the perpendicular plane, $\tau_{c|P}$, be-

ing comparable to the time taken to transmit information along the magnetic field line, $\ell_{z|P}/v_{\mathrm{th}i}$.

Combining all these relations, we arrive at the following asymptotic ordering:

$$v_\zeta \tau_{c|P}, v_{\mathrm{th}i}\tau_{c|P} \sim \ell_{z|P} \sim \mathcal{O}(R), \tag{3.10}$$

$$v_\zeta \Delta t_{\mathrm{peak}|L} \sim \Delta Z, \Delta r, \ell_{x|P}, \ell_{y|P} \sim \mathcal{O}(\epsilon R), \tag{3.11}$$

$$v_Z \Delta t_{\mathrm{peak}|L} \sim \mathcal{O}(\epsilon^2 R), \tag{3.12}$$

where the parameter R is the tokamak major radius, representing the scale of the longest structures in the system. From (3.10-3.12), we see that the time delay of the peak of the cross-correlation function is ordered small compared to the correlation time of the turbulence $\Delta t_{\mathrm{peak}|L} \sim \epsilon\tau_{c|P}$. Inspection of the time-delayed cross-correlation functions measured from experiment, in Figure 2.2, shows that this approximation may be considered reasonable, as all $\Delta t_{\mathrm{peak}|B} \lesssim \frac{1}{2}\tau_{c|B}$.

3.2.4 Laboratory-frame correlation time

The full details of the calculation of the laboratory-frame correlation time, $\tau_{c|L}$, are given in Appendix C.1. The outline of the procedure is as follows: the exponent of the correlation function (B.39) is expanded order by order in ϵ, and at each order the global maximum of the time-delayed cross-correlation function found. The time-delay envelope, described by the peaks $A_{\mathrm{peak}|L}(\Delta Z)$ of the time-delayed cross-correlation functions, which occur at a time delay $\Delta t_{\mathrm{peak}|L}(\Delta Z)$, is then calculated as a function of spacing between poloidal channels, ΔZ. It is found that there is no decay in the peak amplitude of the time-delayed cross-correlation function until second order in the expansion. At second order, the time-delay envelope has a decay time given by

$$\frac{1}{\tau_{c|L}^2} \equiv \frac{1}{\tau_{c|P}^2} + \frac{v_\zeta^2}{\ell_{z|P}^2 \cos^2\alpha}, \tag{3.13}$$

thus defining the laboratory-frame correlation time measured using the CCTD method.

3.2.5 Low-Mach-number ordering

The expression for the laboratory-frame correlation time (3.13) can be further simplified if we adopt, as an ordering subsidiary to (3.10-3.12), the assumption that the Mach number is small $M = v_\zeta/v_{\mathrm{th}i} \sim v_\zeta\tau_{c|P}/\ell_{z|P} \ll 1$. As a result, the second term in (3.13) can be neglected and we find that the laboratory-frame correlation time coincides with the plasma-frame correlation time.

3.2.6 Laboratory-frame poloidal velocity

Using $\Delta t_{\mathrm{peak}|L}(\Delta Z)$ and ΔZ, the laboratory-frame apparent poloidal velocity is calculated as $v_{\mathrm{pol}|L} = \Delta Z / \Delta t_{\mathrm{peak}|L}$, analogous to the BES measurement of $v_{\mathrm{pol}|B}$, described in Section 2.1.3. The resulting apparent poloidal velocity is

$$v_{\mathrm{pol}|L} \equiv v_\zeta \tan\alpha + v_Z. \tag{3.14}$$

To lowest order in the ϵ expansion (3.10-3.12), the apparent poloidal velocity is purely the projection of the toroidal velocity on to the poloidal plane

$$v_{\mathrm{pol}|L} = v_\zeta \tan\alpha + \mathcal{O}(\epsilon v_\zeta). \tag{3.15}$$

Another corollary of the ϵ expansion is that the lowest-order expression for the laboratory-frame poloidal correlation length (3.4) is

$$\ell_{Z|L} = \ell_{y|P} / \cos\alpha + \mathcal{O}(\epsilon \ell_{y|P}), \tag{3.16}$$

which can be used to extract the plasma-frame binormal correlation length, without knowledge of the parallel correlation length.

CHAPTER 4

Point-Spread Functions

As described in Chapter 2, the BES indirectly measures the density field via the intensity of light emitted from excited neutral-beam atoms. The transformation between these two fields is dictated by the Point-Spread Functions (PSFs) of the instrument, see (2.1). In this chapter, we introduce the PSFs and explain how we model their structure.

To understand how the PSFs affect the BES measurements of turbulent quantities, it is necessary to have a good description of the properties of the PSFs. The complicated dependence of the PSFs on the plasma equilibrium, neutral-beam profile, and atomic physics (see variation of the PSFs in Figure 2.1) means that a phenomenological approach is highly beneficial. In Section 4.2, we describe how the shape of the PSFs is characterised, in terms of only three parameters. Then, in Section 4.3, we describe how these parameters vary in MAST. We then introduce, in Section 4.4, an idealised form of a PSF as a tilted Gaussian function, using the three derived parameters and the peak amplitude of the PSF. In order to calculate analytically the effect of PSFs on the measured turbulence parameters, we further assume that all the PSFs have the same shape. Therefore, we approximate the PSFs for a specific time and set of channels (inner or outer — see Section 2.1.4) by using the mean of the PSF parameters. The accuracy of these approximations is tested in Section 4.5, where we introduce a measure to quantify the difference between the real PSFs and the Gaussian-model PSFs.

4.1 Calculation of PSFs for BES systems

A full description of how the PSFs for MAST are calculated is available in [66][1], however, given that the structure of the PSFs is important for the current work, we review the most important aspects here. The PSFs are calculated by considering the emission from the $n = 3 \rightarrow 2$ excited state of the primary-beam atom (Deuterium) on a series of two-dimensional planes aligned perpendicular to the line of sight (LoS) of a detector channel. The emission from each of the two-dimensional planes is integrated on to the focal plane of the optical system by using the fact

[1]This calculation is also similar to that for the BES diagnostics on NSTX [84] and DIII-D [87], though both these use optical fibres in their collection systems.

that the density fluctuations are extended along the parallel direction of the magnetic field [20, 21, 22]. This is equivalent to interpolating a two-dimensional field of density fluctuations along the magnetic field line, to construct a three-dimensional field, and then integrating along the LoS, through this density field, to determine the line-integrated emissivity. Therefore, any misalignment of the LoS and the magnetic field line in the sampling volume would cause smearing of the image. This is the main factor affecting the shape of the PSFs in MAST, as will be discussed in Section 4.3.

Additionally, the radial motion of the beam atoms within the finite lifetime ($3 - 10$ ns) of the excited state causes the radial width of the PSFs to be in the range of $0.5 - 1.5$ cm, with the exact width depending on the velocity of the beam and the plasma density [65].

The finite collection area of the optical system is also included in the calculation of the PSF response. The detector channels receive light from an area of approximately 1.5 cm $\times$ 1.5 cm at the focal plane of the system. The precise collection area depends on the view location of the BES, as the size of the back-image of each detector channel on the beam-line varies with the viewing radius.

The amplitude of the PSFs is proportional to both the local density of the plasma and the beam density. The beam density decreases as the atoms in the neutral beam penetrate the plasma and are ionised by collisions, primarily by charge exchange with the plasma ions. Therefore, the emissivity decreases with decreasing major radius and this is reflected in a decrease in the amplitude of the PSFs. In this work, we normalise each set of PSFs by the maximum amplitude in this set of PSFs, so that we only consider differences between the PSFs.

4.2 Characterisation of the PSFs

The shape of the PSFs can be characterised by two orthogonal vectors, $\mathbf{p}_1$ and $\mathbf{p}_2$, using principal-component analysis [88]. For this purpose, each PSF is normalised to produce a probability distribution from which a sample of points is generated. The principal-component analysis can then be applied to this distribution of points to find the direction of the principal vector $\mathbf{p}_1 = (p_{1r}, p_{1Z})$ in the radial-poloidal plane. The tilt of the PSF is given by the angle

$$\alpha_{\mathrm{PSF}} = \arctan\left(\frac{p_{1r}}{p_{1Z}}\right) \tag{4.1}$$

from the positive Z-axis in the anti-clockwise sense (this is defined in the same sense as the tilt of the correlation function, Θ, see (2.10), and means that all $\alpha_{\mathrm{PSF}} < 0$). The secondary component is defined to be perpendicular to the principal component. We can determine the 'size' of a PSF by constructing a line with the gradient of

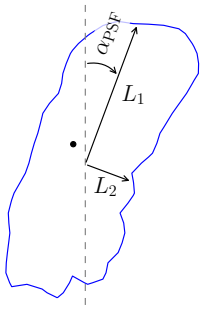


Figure 4.1: A schematic to illustrate the PSF angle $\alpha_{\rm PSF}$, the principal component L_1, and the secondary component L_2. The characterisation of the PSFs in terms of these three parameters is described in Section 4.2.

the principal component that passes through the peak amplitude of the PSF. The segment of this line bounded by the points of intersection with the e^{-1}-amplitude contour of the PSF then defines the length $2L_1$. Following the same procedure with the secondary component defines the length $2L_2$. A schematic of this analysis is given in Figure 4.1.

The three parameters L_1, L_2 and $\alpha_{\rm PSF}$ cannot be used to reconstruct precisely the contour of the real PSF from which they have been calculated, because they describe the shape of a tilted ellipse. As can be seen in Figure 2.1, the PSFs in MAST are clearly not elliptical. However, the characterisation in terms of the three PSF parameters can be used in a simplified model (Section 4.4) that allows us to construct the correlation function of the intensity field analytically (Chapter 5). We will later check how important the neglected effects are, by comparing with numerical calculations that use the real PSFs (Chapter 6).

4.3 PSFs in MAST: 5 representative cases

Case	1	2	3	4	5
Shot	28155	28155	28155	27268	29891
Sub-array	in	in	out	in	out
Time/ms	125	250	125	250	375
L_1/cm	2.0	3.1	2.2	2.8	2.4
L_2/cm	1.1	1.4	1.3	1.3	1.5
$\alpha_{\rm PSF}$/deg	-70	-33	-59	-46	-144

Table 4.1: The mean characteristics of the PSFs from the 5 cases that we are considering (see Figure 2.1). The PSF parameter values in the table are averages over all the PSF parameter values from each channel in the respective subarray, which have been calculated using principal-component analysis (Section 4.2)

In Spherical Tokamaks (STs), such as MAST, because of their tight aspect ratio, the magnetic pitch angle varies significantly over the radial extent of the BES system, which causes, through the misalignment of the LoS and the magnetic field line (see Section 4.1), the shape of the PSFs to vary from channel to channel. As examples we consider the five cases shown in Figure 2.1, with their measured parameters given in Table 4.1. Cases 1-4 are taken from Double-Null Divertor (DND) discharges, where the BES views on the mid-plane of the plasma. Case 5 is from a Lower-Single-Null Divertor (LSND) configuration, where the BES views above the magnetic axis. In the DND cases (especially Case 4), it is clear that the pitch angle of the magnetic field increases with radius, causing the poloidal extent of the PSFs to increase. In Case 5, the different viewing geometry means the magnetic field causes the PSFs to be tilted in the opposite sense to the DND cases. We include Case 5 because of this feature, as it will be useful to see how the different tilts of the PSFs affect the correlation parameters of the intensity field (see Section 6.2.4).

The time evolution of the q profile in MAST causes the PSFs also to vary in time, as can be seen by comparing Case 1 and Case 2, taken from the same shot at two different times. The temporal evolution is mainly due to the increase in the poloidal component of the magnetic field, B_Z, during the shot, causing $\alpha_{\rm PSF}$ to increase. This variation of B_Z in space and time is typical for the majority of DND shots on MAST.

The four DND PSF cases (Cases 1-4) cover most of the possible variation in the PSF parameters for DND discharges, as will be shown in Section 4.5. We focus on DND discharges because the symmetry around the mid-plane implies that magnetic-shear effects on the turbulence do not need to be taken into account when measuring the turbulence parameters.

4.4 Gaussian-model PSFs

Gaussian-model PSFs are constructed from the measured characteristics of the real PSFs from each BES channel i: the principal components L_{1i}, L_{2i}, the tilt angle $\alpha_{{\rm PSF}i}$, and the peak amplitude $A_{{\rm PSF}i}$. These are given by

$$P_i^{\rm Gauss}(\mathbf{r}-\mathbf{r}_i, A_{{\rm PSF}i}, L_{1i}, L_{2i}, \alpha_{{\rm PSF}i}) = A_{{\rm PSF}i}\exp\left(-\frac{\Delta Z'^2}{L_{1i}^2}-\frac{\Delta r'^2}{L_{2i}^2}\right), \qquad (4.2)$$

$$\begin{aligned} \text{with} \quad \Delta r' &= \Delta r\cos(\alpha_{{\rm PSF}i}) + \Delta Z\sin(\alpha_{{\rm PSF}i}), \\ \text{and} \quad \Delta Z' &= \Delta Z\cos(\alpha_{{\rm PSF}i}) - \Delta r\sin(\alpha_{{\rm PSF}i}), \end{aligned}$$

where $\mathbf{r}-\mathbf{r}_i = (\Delta r, \Delta Z) = (r-r_i, Z-Z_i)$, and r_i, Z_i are the positions of the peak amplitudes of the PSFs (assumed to be at the focal points of the BES system — see Appendix D.4). This thesis will make much use of these Gaussian-model PSFs, because of their analytic tractability. From here onwards, unless otherwise stated, we

assume that each set of the Gaussian-model PSFs have the same values of L_1, L_2, and $\alpha_{\rm PSF}$, and these are taken to be the mean of the L_{1i}, L_{2i}, and $\alpha_{{\rm PSF}i}$, respectively, over the inner or outer set of channels. However, we keep the amplitude dependence in $P_i^{\rm Gauss}$ to show, in Section 5.1, that the BES covariance function (5.2) is independent of the PSF amplitude. The requirement for using the mean values is also specified in Section 5.1. Before moving on, let us investigate how good an approximation these Gaussian-model PSFs are to the real PSFs.

4.5 Difference between real and Gaussian-model PSFs

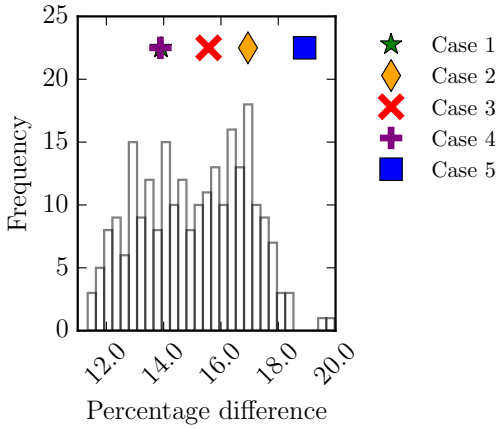


Figure 4.2: Difference between the real PSFs and the Gaussian-model PSFs using the difference measure (4.3) for 245 sets of PSFs calculated at various times in 20 MAST shots in DND configuration. The values for each of the cases presented in Figure 2.1 are indicated with the coloured symbols. Case 5 is not included in the calculation of the histogram, yet is labelled for comparison. Cases 1 and 4 have almost the same value of (4.3).

We define a measure of the difference between a set of the real PSFs, $P_i^{\rm real}$, and the Gaussian-model PSFs, $P_i^{\rm Gauss}$, in order to determine the quality of the approximation (4.2). The measure is the average over the set of real PSFs of

$$\Delta P_0 = \frac{1}{A_{{\rm PSF}i}} {\rm RMS}\left[P_i^{\rm real}(\mathbf{r}-\mathbf{r}_i) - P_i^{\rm Gauss}(\mathbf{r}-\mathbf{r}_i, A_{{\rm PSF}i}, L_1, L_2, \alpha_{\rm PSF})\right]_{\mathbf{r}}, \qquad (4.3)$$

i.e., the root-mean-square (RMS) difference between a real PSF and the Gaussian model (4.2) of the set of PSFs, relative to the peak amplitude of the real PSF. The central position $\mathbf{r}_i$ of the real PSF is defined in Appendix D.1. The measure (4.3) is plotted in Figure 4.2 for 245 sets of PSFs taken from a database of MAST shots [28], and shows that the difference between the real and Gaussian-model PSFs lies in the range 12-18%. There are two key factors that contribute to this difference: the use of the average values for the PSF parameters (ignoring the spatial variation across the

subarray) and the assumption of a Gaussian shape. In Appendix D, we show that the main contribution to this difference comes from the assumption of a Gaussian shape for the PSFs rather than from their spatial variation. We note that the percentage differences given in Figure 4.2 do not represent the error in the measured correlation parameters associated with using the Gaussian-model PSFs in place of the real PSFs when applying these to a fluctuating density field, which will be discussed in Section 6.3.

	Case 1	Case 2	Case 3	Case 4	Case 5
Difference from Gaussian/%	14	17	16	14	19
RMS / deg.	2.4	3.9	3.6	3.1	5.4

Table 4.2: Table of values for the difference measure (4.3) defined in Section 4.5 for each of the five cases described in Section 4.3. Additionally, values are given for the root-mean-square (RMS) of the differences between the tilt angle Θ_B measured from synthetic-BES data generated using real and Gaussian-model PSFs. The mean is taken over the difference in values for each PSF case in Figure 6.1(d), see Section 6.3.4 for the relevant discussion.

On the histogram plot of Figure 4.2, we also indicate the values of the difference measure (4.3) for the five PSF cases introduced in Section 4.3. The numerical values are given in Table 4.2. The example cases have been chosen so that they span as large a range of the difference measure as possible and can, therefore, be used to quantify how the difference between the effect of real and Gaussian-model PSFs on correlation parameters (see Section 6.3) depends on how well the Gaussian-model PSFs agree with the real PSFs.

CHAPTER 5

Analytic calculations of the effect of PSFs

5.1 Effect of PSFs on the 2D spatial structure of the correlation function

In this section, we calculate analytically the relationship between the laboratory-frame correlation lengths and wavenumbers to those measured by the BES system by taking account of PSF effects. Using (2.1) and (2.3), we write the covariance function between two BES detector channels, located at positions $\mathbf{r}_i$ and $\mathbf{r}_j$, as

$$\begin{aligned} C_B^{\mathrm{cov}}(\mathbf{r}_i, \mathbf{r}_j) &= \frac{\left\langle \int P_i(\mathbf{r}-\mathbf{r}_i)\delta n(\mathbf{r},t)\mathrm{d}^2\mathbf{r} \int P_j(\mathbf{r}'-\mathbf{r}_j)\delta n(\mathbf{r}',\mathbf{t})\mathrm{d}^2\mathbf{r}' \right\rangle}{\left\langle \int \mathrm{d}^2\mathbf{r} P_i(\mathbf{r}-\mathbf{r}_i)\langle n(t)\rangle \int \mathrm{d}^2\mathbf{r}' P_j(\mathbf{r}'-\mathbf{r}_j)\langle n(t)\rangle \right\rangle}, \\ &= \frac{1}{\hat{P}_i\hat{P}_j} \int\int \mathrm{d}^2\mathbf{r}\mathrm{d}^2\mathbf{r}' P_i(\mathbf{r}-\mathbf{r}_i)P_j(\mathbf{r}'-\mathbf{r}_j) \left\langle \frac{\delta n(\mathbf{r},t)\delta n(\mathbf{r}',t)}{\langle n(t)\rangle^2} \right\rangle, \qquad (5.1) \\ &= \int \mathrm{d}^2\Delta\mathbf{r} \tilde{P}_{ij}(\Delta\mathbf{r}, \Delta\mathbf{r}_{ij}) C_L^{\mathrm{cov}}(\Delta\mathbf{r}), \qquad (5.2) \end{aligned}$$

where $n(\mathbf{r},t) = \langle n(t)\rangle + \delta n(\mathbf{r},t)$ is the total density field, which is split into a mean part independent of time and constant in space $\langle n(t)\rangle$, and a fluctuating part $\delta n(\mathbf{r},t)$, analogously to the intensity field (2.2) in Section 2.1. In (5.1), we assumed that the PSFs do not vary over the ensemble (time) average and have suppressed the dependence on time delay Δt. The denominator terms are calculated explicitly using (4.2):

$$\hat{P}_i \equiv \int \mathrm{d}^2\mathbf{r} P_i(\mathbf{r}-\mathbf{r}_i) = A_{\mathrm{PSF}i}\pi L_{1i}L_{2i}. \qquad (5.3)$$

In (5.2), we introduced the quantity

$$\tilde{P}_{ij}(\Delta\mathbf{r}, \Delta\mathbf{r}_{ij}) \equiv \frac{1}{\hat{P}_i\hat{P}_j} \int \mathrm{d}^2\Delta\mathbf{a} P_i(\Delta\mathbf{r}+\Delta\mathbf{a}) P_j(\Delta\mathbf{a}+\Delta\mathbf{r}_{ij}), \qquad (5.4)$$

which is independent of the PSF amplitudes, and, therefore, so is C_B^{cov}. We have also assumed that the covariance function given by (B.30): $C_L^{\mathrm{cov}}(\Delta\mathbf{r}) = \langle \delta n(\mathbf{r})\delta n(\mathbf{r}')/\langle n(t)\rangle^2\rangle$, is only a function of the relative position, $\Delta\mathbf{r} = \mathbf{r}-\mathbf{r}'$, i.e., the turbulence is spatially homogeneous, consistent with our assumption in Section 2.1.4. We have changed the integration variables from $(\mathbf{r},\mathbf{r}')$ to $(\Delta\mathbf{r}, \Delta\mathbf{a} = \mathbf{r}'-\mathbf{r}_i)$ so that the BES covariance function becomes a function of the difference $\Delta\mathbf{r}_{ij} = \mathbf{r}_i - \mathbf{r}_j$. However, this does not mean that the BES covariance function is indepen-

dent of the absolute measurement position, as the $\Delta\mathbf{r}_{ij}$ are still dependent on the PSF indices. In order for the BES covariance function to be dependent only on relative position, we also have to require that the PSFs not vary between channels, i.e., that L_{1i}, L_{2i} and $\alpha_{\mathrm{PSF}i}$ should all be the same, as postulated in Section 4.4. The correlation function is then simply

$$C_B(\Delta\mathbf{r}_{ij}) = \frac{C_B^{\mathrm{cov}}(\Delta\mathbf{r}_{ij})}{C_B^{\mathrm{cov}}(0)}, \tag{5.5}$$

where we assume that the correlation function is independent of the channel indices, but retain them to distinguish the discrete BES channel spacing from the continuous density field in the plasma.

In order to proceed, we use the Gaussian-model PSFs given by (4.2). This allows us to compute (5.4) explicitly:

$$\begin{aligned}\tilde{P}(\Delta\mathbf{r}, \Delta\mathbf{r}_{ij}) = \frac{1}{2\pi L_1 L_2} \exp\left\{-\frac{\left[(\Delta r - \Delta r_{ij})\sin\alpha_{\mathrm{PSF}} - (\Delta Z - \Delta Z_{ij})\cos\alpha_{\mathrm{PSF}}\right]^2}{2L_1^2}\right\} \\ \times \exp\left\{-\frac{\left[(\Delta r - \Delta r_{ij})\cos\alpha_{\mathrm{PSF}} + (\Delta Z - \Delta Z_{ij})\sin\alpha_{\mathrm{PSF}}\right]^2}{2L_2^2}\right\}.\end{aligned} \tag{5.6}$$

In order to evaluate the integral in (5.2), we use the laboratory-frame covariance function (B.30), with time delay $\Delta t = 0$. We then compute (5.5) to find the spatial correlation function that the BES would measure:[1]

$$C_{\mathrm{spatial}|B}(\Delta\mathbf{r}_{ij}) = \exp\left(-\frac{\Delta r_{ij}^2}{\ell_{r|B}^2} - \frac{\Delta Z_{ij}^2}{\ell_{Z|B}^2} - \frac{\Delta r_{ij}\Delta Z_{ij}}{\ell_{rZ|B}^2}\right)\cos\left(k_{r|B}\Delta r_{ij} + k_{Z|B}\Delta Z_{ij}\right), \tag{5.7}$$

where

$$\ell_{r|B}^2 = \ell_{r|L}^2 + \frac{4L_1^2L_2^2 + 2\ell_{Z|L}^2(L_1^2\sin^2\alpha_{\mathrm{PSF}} + L_2^2\cos^2\alpha_{\mathrm{PSF}})}{\ell_{Z|L}^2 + 2(L_1^2\cos^2\alpha_{\mathrm{PSF}} + L_2^2\sin^2\alpha_{\mathrm{PSF}})}, \tag{5.8}$$

$$\ell_{Z|B}^2 = \ell_{Z|L}^2 + \frac{4L_1^2L_2^2 + 2\ell_{r|L}^2(L_1^2\cos^2\alpha_{\mathrm{PSF}} + L_2^2\sin^2\alpha_{\mathrm{PSF}})}{\ell_{r|L}^2 + 2(L_1^2\sin^2\alpha_{\mathrm{PSF}} + L_2^2\cos^2\alpha_{\mathrm{PSF}})}, \tag{5.9}$$

$$\ell_{rZ|B}^2 = \frac{D^4}{2(L_1^2 - L_2^2)\sin 2\alpha_{\mathrm{PSF}}}, \tag{5.10}$$

$$\begin{aligned}k_{r|B} = \frac{1}{D^4}\big[&k_{r|L}\ell_{r|L}^2\ell_{Z|L}^2 + 2L_1^2\cos\alpha_{\mathrm{PSF}}(k_{r|L}\ell_{r|L}^2\cos\alpha_{\mathrm{PSF}} + k_{Z|L}\ell_{Z|L}^2\sin\alpha_{\mathrm{PSF}}) \\ &+2L_2^2\sin\alpha_{\mathrm{PSF}}(k_{r|L}\ell_{r|L}^2\sin\alpha_{\mathrm{PSF}} - k_{Z|L}\ell_{Z|L}^2\cos\alpha_{\mathrm{PSF}})\big],\end{aligned} \tag{5.11}$$

$$\begin{aligned}k_{Z|B} = \frac{1}{D^4}\big[&k_{Z|L}\ell_{r|L}^2\ell_{Z|L}^2 + 2L_1^2\sin\alpha_{\mathrm{PSF}}(k_{r|L}\ell_{r|L}^2\cos\alpha_{\mathrm{PSF}} + k_{Z|L}\ell_{Z|L}^2\sin\alpha_{\mathrm{PSF}}) \\ &-2L_2^2\cos\alpha_{\mathrm{PSF}}(k_{r|L}\ell_{r|L}^2\sin\alpha_{\mathrm{PSF}} - k_{Z|L}\ell_{Z|L}^2\cos\alpha_{\mathrm{PSF}})\big],\end{aligned} \tag{5.12}$$

[1] It is also possible to get to (5.7) by using (3.2) in (5.2), as the result is normalised in (5.5).

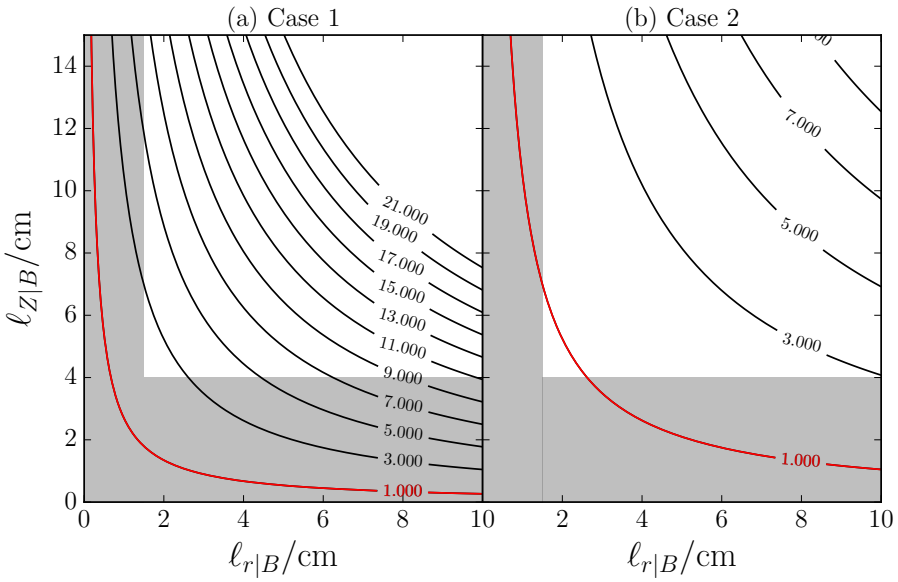


Figure 5.1: Contour lines of Ω, defined by (5.14), for (a) Case-1 PSFs and (b) Case-2 PSFs (see Table 4.1). The regions outside the grey areas indicate the range of typical correlation lengths measured by the MAST BES system. The red contour line shows $\Omega = 1$, which indicates the boundary below which the cross-term (5.10) becomes non-negligible.

and

$$D^4 = 4L_1^2L_2^2 + \ell_{r|L}^2\ell_{Z|L}^2 + 2L_2^2(\ell_{r|L}^2\sin^2\alpha_{\mathrm{PSF}} + \ell_{Z|L}^2\cos^2\alpha_{\mathrm{PSF}}) + 2L_1^2(\ell_{r|L}^2\cos^2\alpha_{\mathrm{PSF}} + \ell_{Z|L}^2\sin^2\alpha_{\mathrm{PSF}}). \tag{5.13}$$

Equations (5.8-5.12) can be easily inverted (see Section 7.1) to express the laboratory-frame parameters as functions of the measured BES parameters and the PSF parameters only. It is clear from the expressions for the BES correlation lengths (5.8) and (5.9) that in the limit of small PSFs, i.e., when $L_1, L_2 \ll \ell_{r|L}, \ell_{Z|L}$, the measured BES and laboratory-frame values are equal. Furthermore, we see that the second terms on the right-hand sides of (5.8) and (5.9) are both positive definite, therefore, the effect of PSFs is always to increase the radial and poloidal correlation lengths above the laboratory-frame values. Consequently, if we take the limit of the radial and poloidal laboratory-frame correlation lengths becoming small compared to the PSF lengths, $\ell_{r|L}, \ell_{Z|L} \ll L_1, L_2$, then the BES-measured correlation lengths will be functions only of the PSF parameters.

The way in which the PSFs affect the wavenumbers is more complicated: from (5.11) and (5.12), we see that the BES-measured wavenumbers depend on the sign of the laboratory-frame wavenumbers, as well as on the sign of the tilt angle of the PSFs. This relationship will be further elucidated in Section 6.2.4.

The appearance of a cross-term (5.10) between Δr_{ij} and ΔZ_{ij}, parametrised by the scale $\ell_{rZ|B}$, is a result purely of the PSFs, as no such term is present in the laboratory-frame correlation function (3.2). Operationally, including the cross-term as an independent fitting parameter causes the fit of (5.7) to (2.4) to become under-constrained and, therefore, reduces our ability to extract the parameters of interest. For this reason, it is opportune to neglect the cross-term in the fitting function. Provided that $\ell_{rZ|B}^2 \gg \ell_{r|B}\ell_{Z|B}$, it is reasonable to do so. This requirement can be written in terms of the BES-measured and the PSF parameters as follows

$$\Omega \equiv \frac{\ell_{Z|B}\ell_{r|B}\left(1+\sqrt{1+(2/\ell_{r|B}\ell_{Z|B})^2(L_1^2-L_2^2)^2\sin^2(2\alpha_{\mathrm{PSF}})}\right)}{4|(L_1^2-L_2^2)\sin 2\alpha_{\mathrm{PSF}}|} \gg 1. \tag{5.14}$$

This is trivially satisfied when $\alpha_{\mathrm{PSF}} = m\pi/2, m \in \mathbb{Z}$, or when $L_1 = L_2$. Figure 5.1 shows that for most measured values of $\ell_{r|B}$ and $\ell_{Z|B}$, the requirement (5.14) is satisfied. Generally speaking, we can always use the fitting function (2.9) without the cross-term and then calculate Ω for fitted BES-measured correlation parameters to check that it is sufficiently large. However, this post-fitting test does not guarantee that the cross-term could have been safely neglected, because the inputs into the evaluation of Ω are calculated from fitting (2.9) and not from fitting (5.7) to the correlation function (2.4).

5.2 Effect of PSFs on the fluctuation amplitude

The effect of the PSFs on the mean-square fluctuation amplitude can be quantified by considering the auto-covariance function, setting $\Delta\mathbf{r}_{ij} = 0$ in (5.2):

$$\sigma_{\mathrm{amp}|B}^2 \equiv \int \mathrm{d}^2\Delta\mathbf{r}\,\tilde{P}(\Delta\mathbf{r},0)C_L^{\mathrm{cov}}(\Delta\mathbf{r}), \tag{5.15}$$

where we have introduced the notation $\sigma_{\mathrm{amp}|B}$, to distinguish the amplitude calculated using Gaussian-model PSFs from the equivalent quantity $\overline{\delta I/I}$ measured in experiment or from numerically generated synthetic-BES data, see (2.5), as these are only guaranteed to be the same if the assumptions of Section 5.1 are satisfied, i.e., that the turbulence is homogeneous and all the PSFs in a subarray are the same. Then, using (2.9) and (5.6) to complete the integral in (5.15), we find

$$\begin{aligned}\frac{\sigma_{\mathrm{amp}|B}^2}{\sigma_{\mathrm{amp}|L}^2} = \frac{\ell_{r|L}\ell_{Z|L}}{D^2}\exp\Bigg\{-\frac{1}{2D^4}\Big[&2L_1^2L_2^2(k_{r|L}^2\ell_{r|L}^2+k_{Z|L}^2\ell_{Z|L}^2)\\ &+\ell_{r|L}^2\ell_{Z|L}^2L_1^2(k_{r|L}\sin\alpha_{\mathrm{PSF}}-k_{Z|L}\cos\alpha_{\mathrm{PSF}})^2\\ &+\ell_{r|L}^2\ell_{Z|L}^2L_2^2(k_{r|L}\cos\alpha_{\mathrm{PSF}}+k_{Z|L}\sin\alpha_{\mathrm{PSF}})^2\Big]\Bigg\},\end{aligned} \tag{5.16}$$

where $\sigma_{\mathrm{amp}|L}^2 \equiv C_L^{\mathrm{cov}}(0)$ is the mean-square fluctuation amplitude in the laboratory frame (B.41). The quantity $\sigma_{\mathrm{amp}|L}$ is the analytic equivalent of the fluctuation am-

plitude of the density field $\overline{\delta n/n}$, defined analogously to $\overline{\delta I/I}$ in (2.5) replacing the intensity field with the density field.

Generally, we see that the BES-measured mean-square fluctuation amplitude $\sigma^2_{\mathrm{amp}|B}$ is a linear function of the laboratory-frame mean-square fluctuation amplitude $\sigma^2_{\mathrm{amp}|L}$, which means that inverting the relationship (5.16) is easy (see Chapter 7). As both $D^2 \geq \ell_{r|L}\ell_{Z|L}$ and the exponent in (5.16) is always negative, the PSFs always cause the fluctuation amplitude of the measured signal to be lower than the fluctuation amplitude of the laboratory-frame density field. For most standard values of turbulence parameters (see Chapter 6), the exponent in (5.16) is small and the dominant effect comes from the coefficient $\ell_{r|L}\ell_{Z|L}/D^2$.

5.3 Effect of PSFs on the correlation time and poloidal velocity

Following the CCTD method described in Section 2.1.2, the correlation time is computed by finding the envelope of the peaks of the time-delayed cross-correlation functions. We adopt the asymptotic ordering introduced in Section 3.2.3, with the additional ordering of the PSF lengths L_1, L_2 as the same order as the radial, $\ell_{x|P}$, and poloidal, $\ell_{y|P}$, correlation lengths. The derivation, including PSF effects, of the correlation time and apparent poloidal velocity using the CCTD method is given in Appendix C.2; here we simply present the results.

The apparent poloidal velocity is unaffected by PSFs:

$$v_{\mathrm{pol}|B} = v_\zeta \tan\alpha + v_Z + \mathcal{O}(\epsilon^2 v_\zeta), \tag{5.17}$$

where the second term is $\mathcal{O}(\epsilon^1)$ smaller than the first term and, therefore, under the assumptions of Section 3.2.3 any measurement will be dominated by the toroidal rotation.

The correlation time is also independent of the PSFs:

$$\frac{1}{\tau^2_{c|B}} = \frac{1}{\tau^2_{c|L}} = \frac{1}{\tau^2_{c|P}} + \frac{v_\zeta^2}{\ell^2_{z|P}\cos^2\alpha} + \mathcal{O}(\epsilon), \tag{5.18}$$

where the term containing v_ζ can be neglected if, in addition to (3.10-3.12), we assume a subsidiary ordering in small Mach number, as was done in Section 3.2.5. Then the correlation time measured using the CCTD method on the intensity field, $\tau_{c|B}$, is the same as the plasma-frame correlation time.

CHAPTER 6

Characterising the effect of PSFs on correlation parameters

We wish to understand how PSFs affect the turbulent parameters and also whether, in determining this, spatially invariant Gaussian-model PSFs (4.2) are a good approximation for the real PSFs. In order to determine the effects of real PSFs, a fluctuating density field must be generated to which the real PSFs can be applied. Our model for such a fluctuating density field is described in Section 6.1. Then, in Section 6.2, we apply the real PSFs (Cases 1-5) to this numerically generated model field using (2.1), measure the resulting correlation parameters as described in Section 2.1, and discuss how the correlation parameters of this synthetic-BES data differ from the correlation parameters in the laboratory frame of the model fluctuating field (i.e., before applying the real PSFs). In Section 6.3, we use the analytically derived laboratory-frame correlation parameters of the model field (Appendix B), and the measured PSF parameters for the five MAST representative cases (Table 4.1), to calculate the analytic BES correlation parameters using (5.8-5.12) and (5.16). We then compare these with the correlation parameters measured from the synthetic-BES data of Section 6.2 and quantify how well the Gaussian-model PSFs reproduce the effects of the real PSFs. In Section 6.4, we summarise the results.

6.1 Model fluctuating density field

We will use a model fluctuating density field designed so that the correlation function of its time series is exactly the plasma-frame correlation function (3.1) or the laboratory-frame correlation function (3.2) and (3.7), depending on which frame it is calculated in. This is shown analytically in Appendix B, where the details of our model field are presented. We stress that this model is purely phenomenological and contains no physical prescription for the formation of turbulent structures, and is thus similar to the models used in other tests of measurement techniques [66, 89, 90].

A time series of density fluctuations is generated by constructing a signal from the sum of N localised perturbations. The initial locations at which the perturbations are formed are randomly chosen in space and time (uniformly distributed within the domain). Each individual perturbation has a functional form similar

to the plasma-frame correlation function (3.1), but with an amplitude taken from a Gaussian distribution with zero mean and standard deviation σ_{amp} and a phase taken from a uniform random distribution in the range $[0, 2\pi]$.

Each perturbation is allowed to grow and then decay over a finite number of correlation times. The radial wavenumber evolves with time as $k_x = k_{x0} + k_y S t$, where k_{x0} is the radial wavenumber at peak amplitude, S is the flow shear, and t is time. The flow shear does not appear in any of the following expressions because it is absorbed into the definition of the plasma-frame radial correlation length and correlation time, see (B.20) and (B.23), is kept constant throughout this work, and has only a minor effect on the measured quantities.

The perturbations are created in the plasma frame. To transform them into the laboratory frame, the toroidal velocity v_ζ, poloidal velocity v_Z, and the pitch angle of the magnetic field, must be specified. In this work, these are assumed to be constants in position and time. The pitch angle is set to $\alpha = 30°$, which is representative of the value in the outer-core of MAST plasmas.

The output of the model is a two-dimensional radial-poloidal fluctuating density field in the laboratory frame, to which the real PSFs can be applied by evaluating the integral (2.1). This then gives a radial-poloidal fluctuating intensity field (a synthetic "BES measurement") that can be analysed using the same methods that are applied to the experimental BES data, as described in Section 2.1.

6.2 The effects of real PSFs

In this section, we consider what effects the real PSFs have on the measurement of turbulence parameters. We consider each of the plasma-frame parameters in turn: the fluctuation amplitude, radial correlation length, binormal correlation length, tilt angle (the ratio of radial and binormal wavenumbers), correlation time, and apparent poloidal velocity. Proceeding through the panels in Figure 6.1(a-f), each of these plasma-frame correlation parameters is varied, keeping all other quantities constant. To start with, we are only concerned with the discrete data points (the solid lines will be discussed in Section 6.3). The laboratory-frame correlation parameters measured from the model fluctuating density field, using the methods of Section 2.1, are marked with filled black circles. The equivalent correlation parameters of the synthetic-BES intensity fields, generated using (2.1) with the five PSF cases (Figure 2.1 and Section 4.3), are marked with coloured shapes. By comparing the correlation parameters of these five PSF cases to the laboratory-frame correlation parameters, we see what effect the real PSFs have.

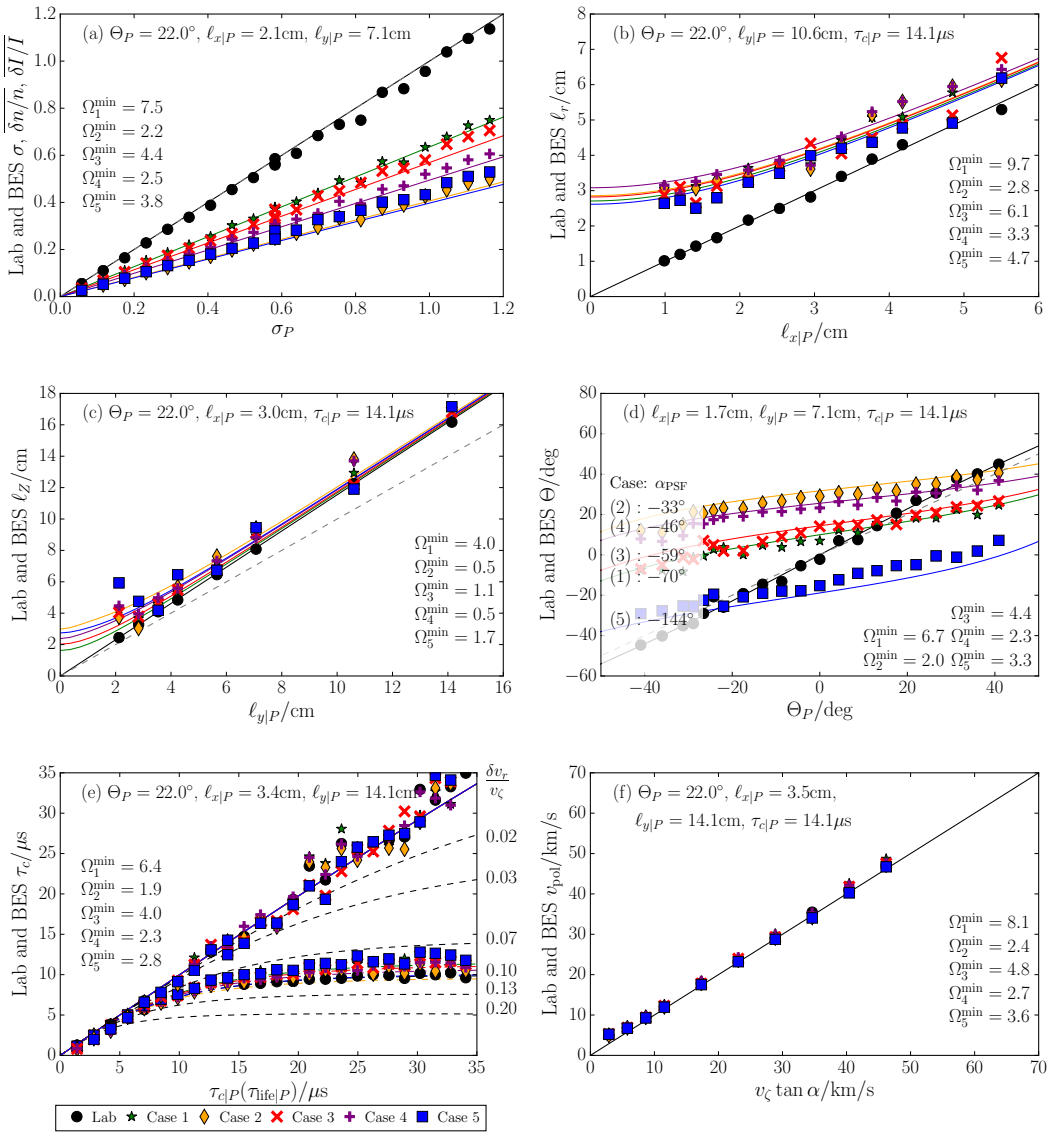


Figure 6.1: (a) Fluctuation amplitude, (b) radial correlation length, (c) poloidal correlation length, (d) tilt angle; (e) correlation time, and (f) apparent poloidal velocity in the laboratory-frame with and without PSF effects, plotted against their plasma-frame values. The markers correspond to numerical calculations using the model of fluctuating fields described in Section 6.1 and are discussed in Section 6.2. The black markers correspond to measurements of the correlation parameters made in the laboratory frame, whilst the different coloured markers correspond to measurements including the effects of the five PSF cases, which have been introduced in Section 4.3 and are illustrated in Figure 2.1. The black solid lines correspond to the laboratory-frame relations (B.41), (3.3), (3.16), (3.5-3.6), (3.13), and (3.15) in each of the panels, respectively. The coloured lines correspond to the Gaussian-model PSF calculations (5.16), (5.8), (5.9), (5.11-5.12), (5.18), and (5.17), respectively, which are discussed in Section 6.3. The lowest numerical values of Ω, from (5.14), are given in each panel for each PSF case. The lower set of curves in (e), labelled with values of $\delta v_r/v_\zeta$, are discussed in Section 8.3.

6.2.1 Fluctuation amplitude

In Figure 6.1(a), we see that the real PSFs cause the BES-measured fluctuation amplitude $\overline{\delta I/I}$ to decrease compared to the laboratory-frame density-fluctuation amplitude $\overline{\delta n/n}$. The extent of this decrease depends on the PSF case, and, by using the PSF parameters from Table 4.1, can be seen to be approximately proportional to the area, $A \simeq L_1 L_2$, of the PSFs. It is also evident that, for a given set of real PSFs, there is a linear relationship between the laboratory-frame and synthetic-BES fluctuation amplitude.

6.2.2 Radial correlation length

The radial correlation length measured from the synthetic-BES data is longer than the laboratory-frame radial correlation length, as can be seen in Figure 6.1(b). The increase in radial correlation length due to the PSFs is greater for shorter laboratory-frame radial correlation lengths. This occurs because the laboratory-frame radial correlation length becomes shorter than the size of the PSFs ($\simeq L_1$) and, therefore, the radial width of the spatial correlation function becomes dominated by the blurring due to the PSFs as they average over the small-scale perturbations.

The difference between the effect of the different real-PSF cases is small ($\simeq 0.5\ \mathrm{cm}$) for most laboratory-frame radial correlation lengths, suggesting that the detailed shape of the PSFs is not very important in determining to what extent the radial correlation length is increased by the PSFs.

6.2.3 Poloidal correlation length

In Figure 6.1(c), we see that the effect of the real PSFs on the laboratory-frame poloidal correlation length follows similar trends to the radial correlation length discussed in Section 6.2.2. However, at very small values, the poloidal correlation length measured from the synthetic-BES data can increase even as the laboratory-frame poloidal correlation length decreases. This occurs when both the laboratory-frame poloidal and radial correlation lengths are similar to the PSF size. As a result, when fitting (2.9) to extract the spatial correlation parameters, the parameters cannot be well constrained. This can be seen by considering the values of Ω (5.14), which are smallest at low $\ell_{y|P}$, and are given for each PSF case by $\Omega^{\min} \equiv \min \Omega$ in Figure 6.1(c). The values of $\Omega^{\min} \leq 1$, clearly do not satisfy the requirement (5.14), $\Omega \gg 1$, and, therefore, suggest that (2.9) is not the appropriate fitting function to use. Nevertheless, in most experimental measurements of turbulence in MAST, the poloidal correlation length is about three times longer than the radial correlation length [28, 91], and thus this non-monotonic regime is unlikely to be relevant.

6.2.4 Tilt angle of the correlation function

The ratio of the radial, $k_{x|P}$, to binormal, $k_{y|P}$, wavenumbers of turbulence is of particular interest in theories of suppression of turbulence by flow shear, see Part III and [92, 18]. Therefore, we consider the effect of PSFs on this tilt angle, rather than on the two wavenumbers separately. Thus, in addition to (2.10), we define the tilt angle in the laboratory frame to be

$$\Theta_L = -\arctan\left(\frac{k_{r|L}}{k_{Z|L}}\right), \tag{6.1}$$

and the plasma-frame tilt angle to be

$$\Theta_P = -\arctan\left(\frac{k_{x|P}}{k_{y|P}}\right), \tag{6.2}$$

where the wavenumbers in the laboratory frame are related to those in the plasma frame through (3.5) and (3.6).

In Figure 6.1(d), the tilt angles Θ_B of the correlation function of the synthetic-BES data generated using the five representative real-PSF cases are significantly different from the laboratory-frame tilt angle. Generally, the effect of the real PSFs is to decrease the range of possible values of tilt angle that can be observed. For example, consider Case 2, where the tilt angle ranges between $\simeq 10^\circ$ and 45°, despite the laboratory-frame tilt angle ranging between -45° and 45°. The reduction in the range of measurable tilt angles due to PSF effects can be understood by first realising that the radial and poloidal wavenumbers can be determined by the position closest to the peak of the correlation function where the correlation function changes sign. The effect of the PSFs is to change this zero-crossing position, by integrating (unevenly) over the positive and negative regions of the correlation function. Thus, when the tilt angle of the laboratory-frame correlation function is aligned with the PSF angle $\Theta_L \simeq \alpha_{\mathrm{PSF}} \pmod{180^\circ}$, large parts of both negative regions of the correlation function are integrated over (provided the sizes of the PSF and of the correlation function are similar), resulting in the correlation function of the synthetic-BES data having a significantly different zero-crossing position, and, therefore, a different tilt angle. Conversely, the synthetic-BES tilt angles are closest to the laboratory-frame tilt angles when the laboratory-frame tilt angle and the PSF angle are misaligned, i.e., $\Theta_L \simeq \alpha_{\mathrm{PSF}} + 90^\circ \pmod{180^\circ}$.

The tilt angle also differs significantly between the five real-PSF cases. In Figure 6.1(d), we have labelled each curve by the PSF angle from Table 4.1, which shows a clear correlation between the PSF angle and the systematic angular shift between the tilt angle of the correlation function for each of the PSF cases. The reason for these differences can be understood by following the same argument as presented

in the previous paragraph. Therefore, we see that the alignment between Θ_L and α_{PSF} can have a significant effect on the BES measured tilt angle Θ_B.

6.2.5 Correlation time

In this section, we only consider the upper set of data points in Figure 6.1(e); the lower set of data points will be discussed in Section 8.3. There is almost no difference between the laboratory-frame correlation time, $\tau_{c|L}$, and the correlation time measured from the synthetic-BES data, $\tau_{c|B}$, for each of the five PSF cases.

At correlation times above $\simeq 15\ \mu$s, the agreement between the laboratory-frame and synthetic-BES values worsens, but not in a systematic manner. This is because, for longer correlation times, the perturbations decay less quickly as they pass the poloidal detector channels, and, therefore, the change in amplitude that needs to be measured in order to calculate the correlation time becomes smaller. At sufficiently small changes in amplitude, statistical noise from the model fluctuating field can start to affect the measurement of the amplitude of the peak.

6.2.6 Apparent poloidal velocity

The apparent poloidal velocity measured in the laboratory frame and from the synthetic-BES data with the PSFs of all five cases shows considerable agreement, as manifested in Figure 6.1(f). Therefore, the real PSFs have almost no effect on the poloidal-velocity measurement, under the assumptions of our model of fluctuating fields.

6.3 Validity of using Gaussian-model-PSFs

As described in Section 4.4, using the Gaussian-model PSFs relies on the following modelling assumptions:

1. the shape of each PSF is well described by a 2D Gaussian function, parameterised by L_1, L_2 and α_{PSF};

2. all the PSFs in the subarray (inner/outer) of the BES being considered have the same Gaussian parameters;

It is the aim of this section to demonstrate that the above approximations are reasonable, by comparing the effects of the Gaussian-model PSFs, using the PSF parameters in Table 4.1, with the effects of the real PSFs on the turbulence correlation parameters that were discussed in Section 6.2.

6.3.1 Fluctuation amplitude

In Figure 6.1(a), for each of the PSF cases introduced in Section 4.3, the effect of the Gaussian-model PSFs given by (5.15) reproduce the observed effect of the real PSFs on the laboratory-frame fluctuation amplitude. Details of how this comparison is made are provided in Appendix B.4. The most significant difference between the fluctuation amplitudes calculated using the Gaussian-model PSFs and the real PSFs is for Case 5. Indeed, real PSFs of Case 5 show the largest difference from the Gaussian-model PSFs (Figure 4.2). The larger reduction in the fluctuation amplitude determined using the Gaussian model for Case 5 can be explained by the real PSFs for this case being more peaked than a Gaussian, and so behaving more like delta functions under the integral (2.1), reducing the effective area over which the PSFs average.

6.3.2 Radial correlation length

The radial correlation length calculated using the Gaussian-model PSFs (5.8) shows good qualitative agreement with the radial correlation length measured from the synthetic-BES data, as can be seen in Figure 6.1(b). The radial correlation length calculated using the Gaussian-model PSFs tends towards a non-zero constant, dependent on $\ell_{Z|L}$, L_1, L_2, and α_{PSF}, as the laboratory-frame radial correlation length decreases below the PSF size. The fact that (5.8) does not go to zero as the laboratory-frame radial correlation length goes to zero means that, if an experimentally measured radial correlation length is lower than the smallest value of (5.8), the corresponding laboratory-frame value cannot be recovered. Therefore, there is a resolution limit of the BES, which is formalised in Section 7.3.

6.3.3 Poloidal correlation length

The expression (5.9) for the poloidal correlation length with Gaussian-model PSFs is the same as that for the radial correlation length (5.8) when the labels r and Z are interchanged $r \leftrightarrow Z$ and the PSF lengths are interchanged $L_1 \leftrightarrow L_2$. Hence, the poloidal correlation length given by (5.9) has similar features to the radial correlation length (5.8) discussed in Section 6.3.2. However, in real experiments, the poloidal correlation length is longer than both the radial correlation length and the PSF lengths. In such a parameter regime, the laboratory-frame poloidal correlation length is similar to the BES poloidal correlation length, which can be seen in Figure 6.1(c), where (5.9) is plotted for each of the five PSF cases. We also see, in this figure, that the poloidal correlation length given by (5.9) is qualitatively the same as the poloidal correlation length measured from the synthetic-BES data, which has been discussed in Section 6.2.3.

6.3.4 Tilt angle of the correlation function

The tilt angle Θ_B defined in (2.10) is calculated using the radial (5.11) and poloidal (5.12) wavenumbers. In Figure 6.1(d), this analytic calculation shows good qualitative agreement with the tilt angles measured from the synthetic-BES data. The root-mean-square (RMS) differences between these two tilt angles, for each of the five PSF cases, are given in Table 4.2. By comparing these RMS values with the difference measure (4.3) between the shapes of the real and Gaussian-model PSFs, also given in Table 4.2, we see that there is a clear correlation between the two quantities. This suggests that the observed difference is due to the imperfect validity of the assumptions that we have listed at the beginning of this section. The largest RMS difference between the tilt angles is 5.4°, which corresponds to an approximate error of 10% due to using the Gaussian-model PSFs compared to using the real-PSFs.

6.3.5 Correlation time and apparent poloidal velocity

The correlation time given by (5.18) for Gaussian-model PSFs is exactly the same as the laboratory-frame correlation time (3.13). Indeed, in Figure 6.1(e), we see that (5.18) agrees well with the synthetic-BES correlation time for all five representative PSF cases.

The analytic calculation of the apparent poloidal velocity including Gaussian-model PSF effects (5.17) shows that there is no difference in this quantity from the laboratory frame. As the real-PSFs also have no effect on the measurement of the apparent poloidal velocity (see Section 6.2.6), there is, trivially, good agreement between the effects of the Gaussian-model and real PSFs.

6.4 Summary

As the evidence presented in the above sections shows good agreement between the real- and Gaussian-model-PSF effects for all measured turbulence parameters, it seems reasonable to conclude that the Gaussian-model PSFs describe the effects of the real PSFs on the measurement of the turbulent parameters well. More strongly, we have seen that the error in using Gaussian-model PSFs instead of the real PSFs (that was estimated in Section 6.3.4 to be approximately 10%) is smaller than the changes to the measured correlation parameters that are caused by the finite size of the PSFs (see Figure 6.1(a),(b), and (d) for changes over 100%). Therefore, it is worthwhile to use the Gaussian-model PSFs to assess and, in Chapters 7 and 11, correct for the PSF effects, even if they are not exactly the same as the real PSFs.

CHAPTER 7

Correcting for PSF effects

7.1 Laboratory-frame spatial correlation parameters and fluctuation amplitude

The equations (5.8-5.12) for the spatial properties of the turbulence can easily be inverted to find the laboratory-frame parameters as functions of the measured BES parameters:

$$\ell_{r|L}^2 = \frac{1}{2}\left[\ell_{r|B}^2 - 4(L_2^2\cos^2\alpha_{\mathrm{PSF}} + L_1^2\sin^2\alpha_{\mathrm{PSF}}) + \sqrt{\ell_{r|B}^4 + 4(\ell_{r|B}/\ell_{Z|B})^2(L_1^2 - L_2^2)^2\sin^2(2\alpha_{\mathrm{PSF}})}\right], \tag{7.1}$$

$$\ell_{Z|L}^2 = \frac{1}{2}\left[\ell_{Z|B}^2 - 4(L_1^2\cos^2\alpha_{\mathrm{PSF}} + L_2^2\sin^2\alpha_{\mathrm{PSF}}) + \sqrt{\ell_{Z|B}^4 + 4(\ell_{Z|B}/\ell_{r|B})^2(L_1^2 - L_2^2)^2\sin^2(2\alpha_{\mathrm{PSF}})}\right], \tag{7.2}$$

where the positive square roots are the only physically relevant choice, and

$$k_{r|L} = \left[1 + \frac{2(L_1^2\sin^2\alpha_{\mathrm{PSF}} + L_2^2\cos^2\alpha_{\mathrm{PSF}})}{\ell_{r|L}^2}\right]k_{r|B} - \left[\frac{(L_1^2 - L_2^2)\sin(2\alpha_{\mathrm{PSF}})}{\ell_{r|L}^2}\right]k_{Z|B}, \tag{7.3}$$

$$k_{Z|L} = \left[1 + \frac{2(L_1^2\cos^2\alpha_{\mathrm{PSF}} + L_2^2\sin^2\alpha_{\mathrm{PSF}})}{\ell_{Z|L}^2}\right]k_{Z|B} - \left[\frac{(L_1^2 - L_2^2)\sin(2\alpha_{\mathrm{PSF}})}{\ell_{Z|L}^2}\right]k_{r|B}. \tag{7.4}$$

The wavenumbers (7.3) and (7.4) can be combined to find the laboratory-frame tilt angle:

$$\tan\Theta_L = \frac{\ell_{Z|L}^2\left[\tan\Theta_B\sec 2\alpha_{\mathrm{PSF}}(L_1^2 + L_2^2 + \ell_{r|L}^2) - (L_1^2 - L_2^2)(\tan\Theta_B + \tan 2\alpha_{\mathrm{PSF}})\right]}{\ell_{r|L}^2\left[(L_1^2 + L_2^2 + \ell_{Z|L}^2)\sec 2\alpha_{\mathrm{PSF}} + (L_1^2 - L_2^2)(1 - \tan\Theta_B\tan 2\alpha_{\mathrm{PSF}})\right]}, \tag{7.5}$$

which for brevity has been written in terms of the laboratory-frame correlation lengths $\ell_{r|L}$ and $\ell_{Z|L}$, given by (7.1) and (7.2), respectively.

The laboratory-frame fluctuation amplitude can easily be determined from (5.16) once the laboratory-frame spatial parameters (7.1-7.4) have been calculated. One of the advantages of the above explicit expressions for the laboratory-frame parame-

ters is that the uncertainty in the resulting quantities can be derived from the uncertainties on the measurements of the parameters that characterise the BES turbulence and the PSFs.

7.2 Plasma-frame spatial correlation parameters and fluctuation amplitude

The transformations of the laboratory-frame spatial correlation parameters into plasma-frame spatial correlation parameters are described by (3.3-3.6), which require the pitch angle α of the magnetic field to be known. The only complication is in the reconstruction of the plasma-frame binormal correlation length (3.4), as we have no measurement of the plasma-frame parallel correlation length $\ell_{z|P}$. However, by using the asymptotic ordering (3.10-3.12), this parallel correlation length can be neglected and the plasma-frame binormal correlation length can be calculated from (3.16). As discussed in Appendix B.4, the fluctuation amplitude in the plasma frame is the same as that in the laboratory frame.

7.3 Resolution limit of BES

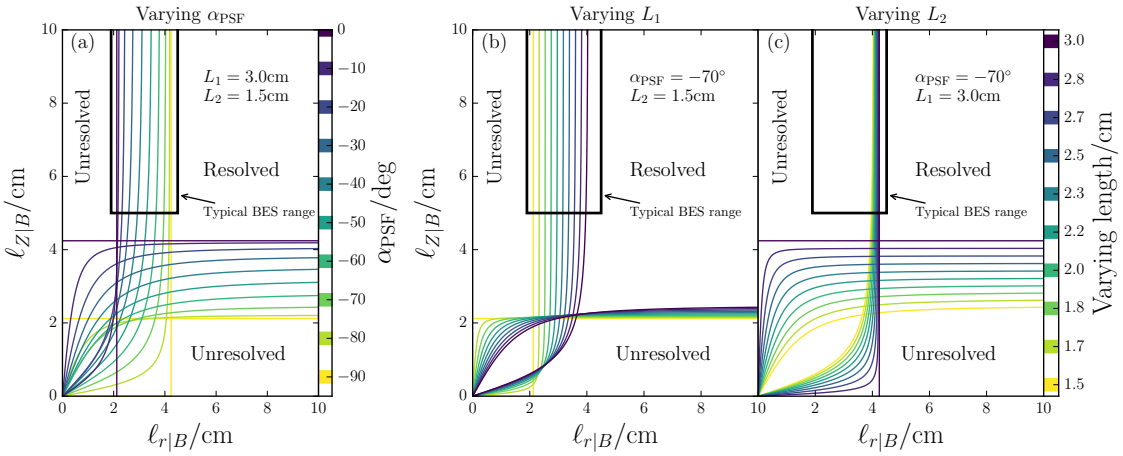


Figure 7.1: Plots of the resolution limits (7.6) and (7.7) showing: (a) the effect of the PSF angle α_{PSF}, (b) the effect of the length of the principal PSF component L_1, (c) the effect of the length of the secondary PSF component L_2, on the resolution limit of the BES system. The black box indicates the typical range of measured correlation lengths using the MAST BES system, see Figure 1.3 and [28].

In all of the above calculations (Chapters 5 and 6), provided the PSF parameters are known, it is always possible to convert between real-valued laboratory-frame parameters and BES parameters, however, this is not necessarily true for the data

taken from the real BES diagnostic. It is possible for the laboratory-frame parameters deduced from this inversion to be imaginary-valued, if the expressions in the right-hand-side of (7.1) and (7.2) are evaluated to be negative. This occurs when the BES-measured correlation length (either $\ell_{r|B}$ or $\ell_{Z|B}$) has a value that is smaller than the minimum value of the same length determined using Gaussian-model PSFs, as can be seen in Figures 6.1(b) and (c). We can, therefore, define the resolution limits as the minimum values of $\ell_{r|B}$ and $\ell_{Z|B}$ that can be obtained from (7.1) and (7.2), which we will refer to as $\ell^{\text{res}}_{r|B}$ and $\ell^{\text{res}}_{Z|B}$, respectively. These minima occur when the laboratory-frame values are zero ($\ell_{r|L} = 0$ or $\ell_{Z|L} = 0$). Equations (7.1) and (7.2) can then be solved for $\ell^{\text{res}}_{r|B}$ and $\ell^{\text{res}}_{Z|B}$, as functions of the measured BES spatial correlation lengths and the PSF parameters. The radial resolution limit is then

$$\ell^{\text{res}}_{r|B} = \frac{2\ell_{Z|B}(L_1^2 \sin^2 \alpha_{\text{PSF}} + L_2^2 \cos^2 \alpha_{\text{PSF}})}{\sqrt{2\ell^2_{Z|B}(L_1^2 \sin^2 \alpha_{\text{PSF}} + L_2^2 \cos^2 \alpha_{\text{PSF}}) + (L_1^2 - L_2^2)^2 \sin^2 2\alpha_{\text{PSF}}}}, \tag{7.6}$$

and the poloidal resolution limit is

$$\ell^{\text{res}}_{Z|B} = \frac{2\ell_{r|B}(L_1^2 \cos^2 \alpha_{\text{PSF}} + L_2^2 \sin^2 \alpha_{\text{PSF}})}{\sqrt{2\ell^2_{r|B}(L_1^2 \cos^2 \alpha_{\text{PSF}} + L_2^2 \sin^2 \alpha_{\text{PSF}}) + (L_1^2 - L_2^2)^2 \sin^2 2\alpha_{\text{PSF}}}}. \tag{7.7}$$

As the laboratory-frame correlation lengths are required to calculate the laboratory-frame wavenumbers, these expressions also determine when the wavenumbers, $k_{r|B}$ and $k_{Z|B}$, are resolved.

Possible reasons why the experimentally measured BES correlation lengths can be below the resolution limits (7.6) and (7.7) include uncertainties in the measurement from the BES, such as background D_α emission and electronic noise in the detector, as well as uncertainties in the equilibrium profiles that are used to calculate the PSFs.

Even measurements above, but near, the resolution boundaries may be unreliable. For example, when the laboratory-frame radial correlation length is calculated using (7.1) any small uncertainty in the BES-measured radial correlation length causes a large uncertainty in the laboratory-frame radial correlation length, see Figure 6.1(b). Therefore, the resolution limits (7.6) and (7.7) must be considered as the absolute lower boundaries of the diagnostic. In order to be confident in the reliability of a reconstruction, an additional constraint on the values of the reconstructed laboratory-frame correlation lengths may be used, such that the reconstructed values are above a certain threshold, e.g., $\ell_{r|L} \geq \ell^{\text{res}}_{r|B}$.

In Figure 7.1, expressions (7.6) and (7.7) are plotted for different combinations of PSF parameters. The region in the upper right side of each plot can be considered resolved. Figure 7.1(a) demonstrates that the tilting of the PSFs can cause a significant change to the position of the resolution limits in the range of $2\,\text{cm} < \ell_{r|B} < 4\,\text{cm}$. As

most of the MAST BES-measured radial correlation lengths lie in this interval, see Figure 1.3 and [28], it is clear that properly accounting for PSF effects is important. The closeness of the resolution boundary to the MAST BES-measured radial correlation lengths also means that a small error, in either of these two quantities, can result in the measurement being essentially unresolved.

In Figures 7.1(b) and 7.1(c), the PSF angle α_{PSF} is fixed and the lengths L_1 and L_2 are varied. From Table 4.1, we see that the principal length L_1 can increase from $2.0\ \mathrm{cm}$ to $3.1\ \mathrm{cm}$ during a shot (Case 1 to Case 2). When α_{PSF} is constant, this means that the radial resolution limit can lay anywhere in the entire range of typical MAST BES measurements of the radial correlation length. Fortunately, typical measured values of the poloidal correlation length tend to be greater than the poloidal resolution limit.

7.4 Testing the inversion method using gyrokinetic simulations

In this section, we discuss only the spatial correlation parameters and fluctuation amplitude, as the model of fluctuating fields that we have been using (Section 6.1) has shown that the PSFs have no effect on the temporal correlation parameters. Later, in Chapter 8, however, we find that PSFs do affect the correlation-time measurement, and attempt to extend our model to explain this.

7.4.1 Assumptions of our method

We have derived, in Chapter 5, the effect of PSFs on a specified correlation function and have tested numerically the validity of these analytic calculations by applying real PSFs to a time series generated by a model fluctuating density field in Chapter 6. Our conclusions about the effect of the PSFs on the turbulent correlation parameters rely on the functional form (3.1) that we have assumed for the correlation function. In order to test this assumption, we generate a density-fluctuation time series (in the laboratory frame) that is more physically motivated than that generated by our artificial model of fluctuating fields by using the turbulence data obtained in numerical simulations of a MAST-relevant plasma [40], with the local, nonlinear, gyrokinetic flux-tube code GS2 [69].

The correlation parameters for this numerical data are calculated, as in Section 2.1, both from the laboratory-frame data and from synthetic-BES data created by applying real PSFs using (2.1). We then use the analytic relations of Section 7.1 and the Gaussian model of the PSFs to estimate the spatial laboratory-frame correlation parameters (corrected parameters) from the correlation parameters of the synthetic-

BES data. By comparing the corrected parameters with the correlation parameters measured from the raw laboratory-frame density field calculated by GS2, we have a direct measure of the quality of the assumptions that underpin our procedure.

7.4.2 Gyrokinetic simulations

The full details of the gyrokinetic simulation that we use can be found in [40]. The equilibrium used for the simulation is taken from MAST shot $\#27268$ at $t = 0.250\ \mathrm{s}$ and at a major radius of $R = 1.32\ \mathrm{m}$ (see Table 11.1). The ion-temperature gradient is $a/L_{T_i} = 4.9$, where a is the minor radius of the last closed flux surface, and $L_{T_i}^{-1} = T_i^{-1}\partial T_i/\partial r$ is the ion (Deuterium) temperature gradient length, with T_i the ion temperature and r the radial coordinate used by GS2, as described in [40]. This simulation was performed with an experimentally relevant equilibrium flow shear $\gamma_E = 0.16\ v_{\mathrm{th}i}/a$. The ion and electron species are both treated kinetically with the true ion-electron mass ratio. Artificial damping is applied to separate the ion and electron spatial scales in order to reduce computation time.

The output of the simulation that we use is a two-dimensional field of density fluctuations spanning $40\ \mathrm{cm} \times 80\ \mathrm{cm}$ in the radial-poloidal plane.[1] The implementation of flow shear in GS2 introduces spurious temporal aliasing of the density field, which increases with radial distance from the centre of the simulation domain. Therefore, we only analyse data from the central region ($\pm 5\ \mathrm{cm}$) of the simulation output. This aliasing effect will be illustrated and discussed in more detail in Chapter 8.

7.4.3 Spatial correlation parameters

The laboratory-frame binned spatial correlation function (see discussion in Section 2.1.4) of the GS2 data calculated from (2.4) is plotted in Figure 7.2(a) and the corresponding fitting parameters measured using (2.9) are given in Table 7.1. We consider the application of two sets of PSFs to the GS2 data, Cases 4 and 5, as typical examples of DND and LSND PSFs, which have been introduced previously in Section 4.3. The correlation functions of the resulting synthetic-BES data for these two cases are shown in Figure 7.2(b) and (d), respectively. Both cases show nearly a factor of two increase of the radial correlation length in the synthetic-BES data, compared to the laboratory-frame correlation length in Figure 7.2(a). The broadening of the correlation function due to the PSFs is more pronounced in the radial direction

[1] The GS2 output for a single flux tube is generated using a single set of equilibrium parameters, however, we note that, when the PSFs are applied to the density field, the spatial variation of these PSFs is caused by radial variations in the equilibrium, thus introducing some inconsistency into the analysis. This would be of concern if we were comparing these simulations directly with experiment rather than simply using them to validate our data-reconstruction technique.

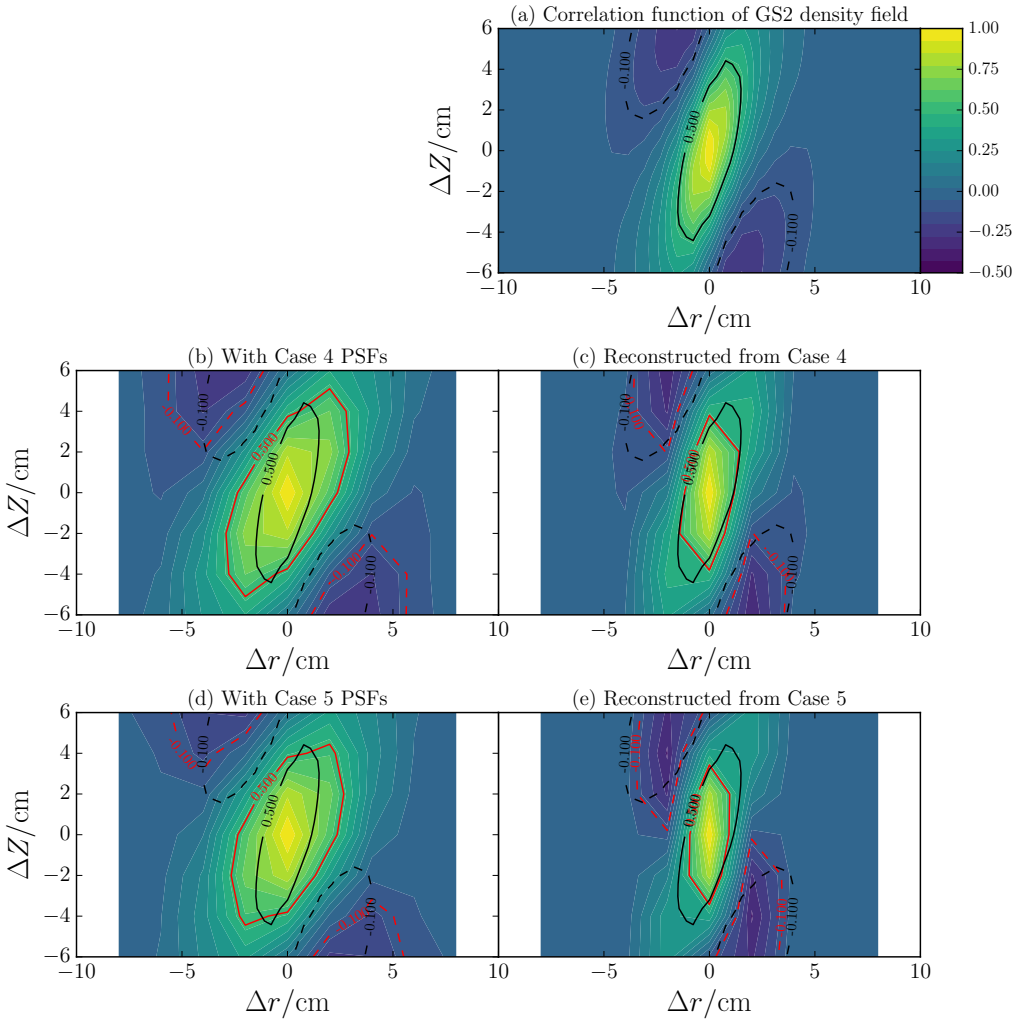


Figure 7.2: Binned spatial correlation functions from a GS2 simulation of MAST [40]: (a) raw GS2 laboratory-frame binned correlation function, also given as black contours in all other panels for comparison; (b) and (d) the correlation function after application, using (2.1), of Case 4 and Case 5 PSFs, respectively (see Section 4.3); (c) and (e) the corrected correlation function after the analytic reconstruction (Section 7.1) is applied to (b) and (d), respectively. Values for the fitted correlation parameters using (2.9) are given in Table 7.1.

than the poloidal direction because the radial correlation length is nearer the PSF size, L_1, than the poloidal correlation length.

The radial wavenumber is a factor of two smaller in the synthetic-BES correlation function compared to the laboratory-frame correlation function. We note that Case-5 PSFs cause a slightly greater reduction of the radial wavenumber, because their principal component is more aligned with the tilt axis of the correlation function than that of the Case-4 PSFs (whose principal component is perpendicular to the tilt axis), see Figure 6.1(d). This is because Case-5 PSFs have a greater "averag-

Parameter	GS2 value	Case 4 →	Corrected	Case 5 →	Corrected
Fluc. amp. [%]	2.2	1.4	2.1	1.4	2.6
ℓ_r/cm	2.16	3.94	2.49	3.43	2.23
ℓ_Z/cm	8.53	10.1	9.78	10.1	9.67
k_r/cm^{-1}	-0.633	-0.341	-0.639	-0.299	-0.873
k_Z/cm^{-1}	0.280	0.246	0.248	0.244	0.278
$\Theta/\mathrm{deg.}$	66	54	69	51	72
$\tau_c/\mu\mathrm{s}$	7.8 ± 3.3	5.7 ± 1.4	–	8.0 ± 3.4	–
$v_{\mathrm{pol}}/km/s$	42.8 ± 9.3	41.9 ± 8.2	–	40.1 ± 8.2	–

Table 7.1: Correlation parameters measured from GS2 simulations with and without PSFs, and the corrected correlation parameters after using the reconstruction method described in Section 7.1. The correlation functions from which the spatial parameters are extracted are plotted in Figure 7.2. The temporal correlation properties are plotted in Figure 8.1.

ing" effect over the oscillatory structure of the correlation function, as discussed in Section 6.2.4.

The measured properties of the PSFs (Table 4.1) are used with the inversion equations of Section 7.1 to correct for the PSF effects. The results of this procedure are plotted in Figures 7.2(c) and (e). We see that these corrected correlation functions match the raw GS2 laboratory-frame correlation function, in Figure 7.2(a), much better than the uncorrected correlation functions of the synthetic-BES data. A closer inspection of the numerical values in Table 7.1 shows that, for both PSF cases, the corrected values of radial and poloidal correlation lengths are near, but overestimate slightly, the raw GS2 correlation lengths.

For Case-4 PSFs, the correction procedure works well for the radial wavenumber ($<1\%$ difference), but not as well for the poloidal wavenumber (11% difference). Conversely, for Case-5 PSFs, the corrected radial wavenumber shows a significant mismatch with the raw-GS2 value (38% difference), whilst the poloidal wavenumber shows good agreement ($<1\%$ difference). The large magnitude of some of these differences between the corrected and raw-GS2 wavenumbers is due to the fact that the radial correlation length is approximately the same size as the principal component of the PSFs and, therefore, any small errors in the fitting of the correlation function, combined with the differences between the Gaussian-model PSFs and the real PSFs, are amplified. The worse performance of the correction procedure for Case 5 compared to Case 4 is also related to the fact that the Gaussian model is a better approximation to the Case-4 real PSFs than to the Case-5 real PSFs (see Section 4.5).

7.4.4 Fluctuation amplitude

The fluctuation amplitude is calculated using (2.5) and is given in the first row of Table 7.1. As expected from Section 6.2.1, the PSFs reduce the observed fluctuation amplitude. Correcting for the PSF effects using (5.16) works well in the analysis of Case 4. In contrast, the correction for Case-5 PSFs overestimates the fluctuation amplitude, which is consistent with (5.16) overestimating the reduction in the fluctuation amplitude when using Gaussian-model PSFs for this case, compared to the numerical evaluation using the real PSFs, as seen in Figure 6.1(a).

CHAPTER 8

Temporal correlation parameters: further refinements

In Table 7.1, the mean correlation times measured with and without the PSFs of Case 4 are significantly different from each other. This appears to contradict the calculation of Section 5.3, where the PSFs were shown not to affect the measurement of the correlation time.

The measurements of the correlation time and apparent poloidal velocity are made at each radially separated array of poloidal channels in the 2D BES array, and similarly at each radially distinct set of poloidal grid points in the GS2 numerical domain. Therefore, it is possible to plot radial profiles of $\tau_{c|B}$ and $v_{\mathrm{pol}|B}$ resulting from these measurements, which is done in Figure 8.1. In Figure 8.1(a), we see that the GS2 laboratory-frame correlation time decreases when $|r| \gtrsim 2$ cm. This has been identified as a numerical effect due to aliasing caused by the algorithm used to implement flow shear in GS2. Therefore, we will not consider data points outside of

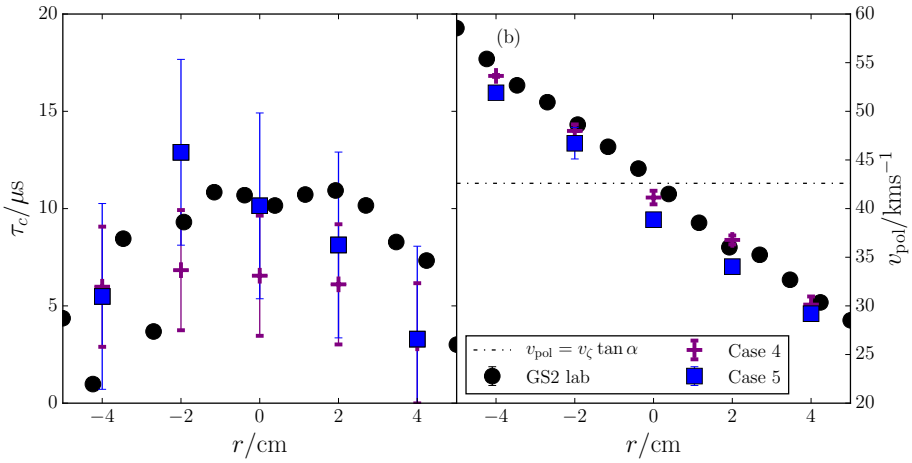


Figure 8.1: The effect of PSFs on the correlation time measured from the GS2 simulation of MAST shot #27268: (a) Correlation time calculated using the CCTD technique (Section 2.1.2) in the laboratory-frame (black circles) and from synthetic-BES data with the Case 4 (purple crosses) and the Case 5 (blue squares) PSFs, against radial position relative to the centre of the GS2 simulation domain. The errors on the PSF data are calculated from (8.5). (b) Apparent poloidal velocity measured from the same simulation. The nominal toroidal rotation projected onto the poloidal plane $v_{\mathrm{pol}} = v_\zeta \tan\alpha = 42.6\mathrm{km/s}$ is shown by the horizontal dot-dashed line.

this radial range in the following discussion.

As we see in Figure 8.1(a), the correlation times calculated with the Case-5 PSFs are similar to the laboratory-frame correlation times, which is possibly because these PSFs have a narrower shape, closer to a delta function, as discussed in Section 6.3.1. However, the correlation times calculated using the Case-4 PSFs have values that are approximately half of the true laboratory-frame correlation times. Additionally, in Figure 8.1(b), we see that both Case-4 and Case-5 PSFs produce apparent poloidal velocities that have a small, but noticeable, difference from the laboratory-frame apparent poloidal velocities. In this chapter, we attempt to explain these differences.

8.1 Physical interpretation of the correlation time

The correlation time in the plasma frame is defined in (3.1) to be $\tau_{c|P}$, which can be 'measured' by calculating the time-delay auto-correlation function of the density field (by replacing δI in (2.4) with δn) at a fixed spatial point in the plasma frame, and fitting this function by (3.1) with $\Delta x = \Delta y = \Delta z = 0$. The value of the correlation time $\tau_{c|P}$ is determined by two effects: (1) the Lagrangian decay of a moving perturbation with time, and (2) the Eulerian decorrelation of a perturbation as it is advected past the measurement location by the turbulent velocity field. These two effects are related, as the turbulent velocity field is determined from the electrostatic potential related to the perturbed density field, and, therefore, the velocity field will decorrelate at a similar rate to the density perturbations. Therefore, the correlation time $\tau_{c|P}$ can be defined to be the fundamental decorrelation timescale associated with the turbulence.

In our model of fluctuating fields (see Section 6.1), which has a correlation function that is exactly the plasma-frame correlation function (3.1), we did not give the individual perturbations (B.2) any small random velocities, and, therefore, it was assumed that there was no Eulerian contribution to the correlation time. In the following section we describe how we refine our model to include such velocities, and discuss the consequences of doing so for the functional form of the correlation function.

8.2 Introducing a fluctuating radial velocity into the model of fluctuating fields

In Appendix B.1, we describe how to include the effect of a fluctuating radial velocity v_r on the motion of our model perturbations; in Appendix B.2, the plasma-frame correlation function (B.19) is calculated assuming that this radial velocity is a Gaussian-distributed random variable with zero mean and standard deviation δv_r.

We do not include a fluctuating binormal velocity, because, for typical binormal correlation lengths, the effect of PSFs on the binormal correlation length has been shown to be small (Section 6.2.3).

In Appendix B.2, the plasma-frame correlation time of our model is found to be

$$\frac{1}{\tau_{c|P}^2} = \frac{1}{\tau_{\text{life}|P}^2} + \frac{1}{\tau_{\text{eddy}|P}^2}, \tag{8.1}$$

where $\tau_{\text{life}|P}$ is the Lagrangian lifetime of a perturbation defined by (B.23) and

$$\tau_{\text{eddy}|P} = \frac{\ell_{x|P}}{\delta v_r} \frac{\sqrt{2}}{\sqrt{2 + k_{x|P}^2 \ell_{x|P}^2}}, \tag{8.2}$$

is the eddy turn-over-time. In order to calculate $\tau_{c|P}$, we assume, in addition to the ordering (3.10-3.12), that the fluctuating radial velocity is small, $\delta v_r / v_\zeta = \mathcal{O}(\epsilon^1 = \rho_i/a)$, compared to the toroidal velocity. This assumption is reasonable, as the fluctuating radial velocity (1.9) in the gyrokinetic simulation used in Section 7.4 is found to be 2% of the toroidal velocity.

In Appendix C.1, the laboratory-frame correlation time $\tau_{c|L}$ is calculated and found to be the same as the plasma-frame correlation time $\tau_{c|P}$ in the low-Mach number limit (Section 3.2.5), just as we found before in (3.13). The appearance of both the lifetime and the eddy-turn-over time in (8.1) means that the measured correlation time in the laboratory frame $\tau_{c|L}$ will be dominated by the smaller of $\tau_{\text{life}|P}$ or $\tau_{\text{eddy}|P}$. We demonstrate this effect in Figure 6.1(e), where the laboratory-frame correlation time $\tau_{c|L}$ is plotted against the lifetime $\tau_{\text{life}|P}$. We see that, as the fluctuating radial velocity increases relative to the toroidal velocity, the correlation time $\tau_{c|L}$ becomes less sensitive to changes in the lifetime.

In Appendix C.2, the PSF effects on the temporal parameters are calculated from the laboratory-frame correlation function (B.39), whilst retaining the radial-velocity effects. The resulting BES-measured correlation time is then (C.19)

$$\frac{1}{\tau_{c|B}^2} = \frac{1}{\tau_{\text{life}|P}^2} + \frac{1}{\tau_{\text{eddy}|B}^2}, \tag{8.3}$$

where the BES eddy-turn-over time is

$$\tau_{\text{eddy}|B} \equiv \left[(2 + k_{r|L}^2 \ell_{r|L}^2) \frac{\delta v_r^2}{2\ell_{r|B}^2} + \left(\frac{k_{Z|L}^2 \ell_{Z|L}^2}{2\ell_{r|B}^2} - \frac{k_{Z|L}^2 \ell_{Z|L}^4}{2D^4} \right) \delta v_r^2 \right]^{-1/2}, \tag{8.4}$$

where D is given by (5.13), and we have written (8.4) in terms of both laboratory-frame and BES-measured correlation parameters, in order to be concise (the relationships between these two sets of parameters are given by (7.1-7.4)).

The reason why the BES eddy-turn-over time (8.4) is different from the plasma- and laboratory-frame eddy-turn-over times (8.2) is because, by introducing the fluctuating radial velocity into our model of fluctuating fields, the plasma-frame cor-

relation function (B.19) of the individual perturbations is no longer equal to (3.1). The difference between these two correlation functions is that in (B.19) cross terms (e.g, $\Delta x \Delta t$) between spatial and temporal relative coordinates are introduced by the fluctuating radial velocity. Then, when the PSF integral (2.1) is calculated in (5.1), mixing occurs between the spatial and temporal correlation parameters.

As the fluctuating component of the radial velocity is not measured experimentally, quantifying how large the difference is between the laboratory-frame and BES-measured correlation times becomes difficult. However, we may estimate the maximum size of the PSF effects if we assume that the plasma-frame correlation time is dominated by the eddy-turn-over time. Then the fractional difference between the laboratory-frame (8.1) and BES-measured (8.3) correlation times is independent of δv_r, and given by

$$\hat{\tau}_{\rm err} \equiv \frac{\left|\tau_{c|B} - \tau_{c|L}\right|}{\tau_{c|B}} \simeq \left|1 - \frac{\tau_{{\rm eddy}|L}}{\tau_{{\rm eddy}|B}}\right| \simeq \left|1 - \frac{\ell_{r|L}}{\ell_{r|B}}\right|, \tag{8.5}$$

where the final expression is reached by assuming that the poloidal correlation length $\ell_{Z|L} \gg \ell_{r|L}, L_1, L_2$, which is reasonable based on experimental measurements (see Table 2.1 and [28]). The error calculated using (8.5) gives an order-of-magnitude estimate of the error associated with the PSF effects (we discuss the sign of the error in Section 8.3). The errors on the correlation times of the synthetic-BES data plotted in Figure 8.1(a), have been calculated using (8.5), which shows that these are the correct size to account for the differences between the synthetic-BES and the laboratory-frame correlation times. This error estimate can be considered to be independent of our model for v_r, as the result (8.5) can also be reached by simply arguing that the typical size of PSF effects can be given by the ratio $\ell_{r|L}/\ell_{r|B}$.

8.3 Limitations of our model

Unfortunately, the laboratory-frame correlation time cannot be reconstructed from the synthetic-BES correlation time measured from the gyrokinetic simulations using (8.4), even if the value of the fluctuating radial velocity δv_r is known. There are two reasons why this is the case. The first is our assumption of Gaussian-model PSFs, and the second is our assumption that the fluctuating velocity field follows a Gaussian distribution.

We demonstrate the discrepancy that arises due to using Gaussian-model PSFs by applying the real PSFs to the density field generated by our model of fluctuating fields, just as we did in Section 6.2. From Figure 8.2, which is an enlargement of Figure 6.1(e), we see that the correlation times calculated with the real PSFs and with the Gaussian-model PSFs (8.3) do not agree (most notably for Case 5). The difference

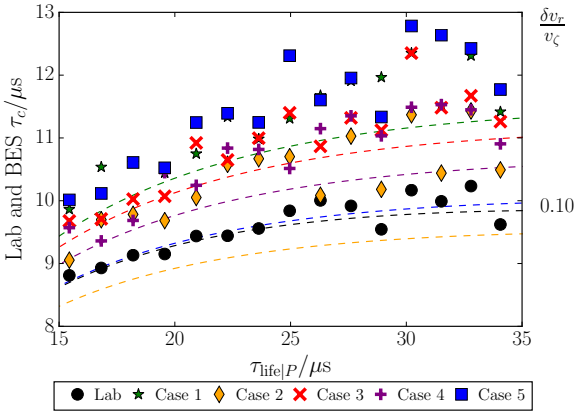


Figure 8.2: Enlargement of Figure 6.1(e) around the $\delta v_r/v_\zeta = 10\%$ curve, to illustrate the difference between the Gaussian-model PSF calculation (8.3) of the effects of PSFs on the correlation-time measurement (coloured dashed lines) and the effect of the real PSFs (coloured markers). The length of the simulation was increased from $T = 2$ ms to $T = 20$ ms to calculate these data points in order to reduce the statistical noise in the measurement.

between the Gaussian-model and the real PSFs plays a more important role in the correlation-time measurement than in the measurements of spatial correlations in Section 7.4 because the change in amplitude of the correlation function required to measure the correlation time is a second-order effect (in $\epsilon = \rho_i/a$, see Section 3.2.3).

Furthermore, the modelling assumption of a Gaussian-distributed v_r that we have used is too limiting. This can be seen by comparing the change in the correlation time caused by the real PSFs for Case 4 in Figure 8.2, where the assumption of a Gaussian-distributed v_r has been used, to the change in the correlation time for the same real PSFs on the GS2 density field in Figure 8.1(a). In Figure 8.2, the synthetic-BES correlation time is longer than the laboratory-frame correlation time, whereas in Figure 8.1(a), the synthetic-BES correlation time is shorter than the laboratory-frame correlation time. As the exact same set of real PSFs has been used to generate both sets of synthetic data, the difference in behaviour between the correlation times of the two sets of synthetic data must be due to the different models used to generate the fluctuating fields. This is not surprising, given that our assumption of a Gaussian-distributed v_r with no interactions between the individual perturbations is a gross simplification of a truly turbulent velocity field.

Finally, we note that one of the key assumptions in this thesis is that the functional form for the time decay of the correlation function is a Gaussian; see (3.1). In previous work [28], an exponential decaying function, $f(t) = \exp(-|t|/\tau_{c|B})$, was used to measure the correlation time $\tau_{c|B}$ from the MAST BES signals. Indeed, this might in fact be a better fit to the experimental correlation function in Figure 2.2.

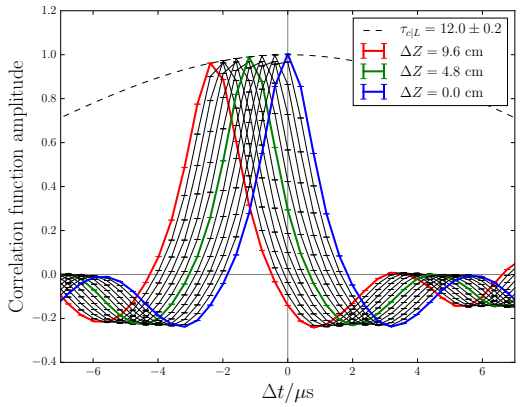


Figure 8.3: Time-delayed correlation functions from the gyrokinetic simulation introduced in Section 7.4.2, at $r = 0.35$ cm from the centre of the simulation domain, for a range of poloidal displacements ΔZ. The range of ΔZ used to generate this plot has been increased compared to that used to calculate the data in Table 7.1, in order to emphasise the quality of the Gaussian fit (2.7) to the peaks of the curves for each ΔZ. This should be compared to the time-delay correlation functions of the experimentally measured intensity field from the MAST BES data in Figure 2.2.

Therefore, it could be argued that the failure of our procedure to account for PSF effects on the correlation-time measurement was due to the failure of our underlying assumption on the structure of the time-delay correlation function. However, the peaks of the time-delay correlation function from the gyrokinetic simulations (shown in Figure 8.3) that were used in this section to identify these issues are, in fact, well fit by the Gaussian function (2.7).

8.4 Apparent poloidal velocity

We see in Figure 8.1(b) that the apparent poloidal velocity varies in the range of $30 - 60$ km/s across the radial extent of the analysis region. This is due to the flow shear in the simulated density field adding to the bulk toroidal rotation. The apparent poloidal velocities measured from the synthetic-BES data for the two PSF cases are also plotted in Figure 8.1(b) and show reasonably good agreement with the laboratory-frame apparent poloidal velocity, deviating, at most, by 5 km/s. Evidently, the effect of the PSFs on this measurement is smaller than on the correlation-time measurement, which is because the toroidal velocity is significantly greater than all other velocities in the GS2 simulation.

Nevertheless, the real PSFs do have a small systematic effect on the apparent-poloidal-velocity measurement, which is not included in our analytic expression (5.17) using Gaussian-model PSFs, even when one accounts for a fluctuating radial velocity field (see Appendix C.2). Therefore, we see, again, that our model is not

able to account fully for the effects of PSFs on the measurement of the temporal properties of the turbulence. We can, however, be reassured that measurements of apparent poloidal velocities can be accurate to within 10% of the laboratory-frame value, without having to be corrected for PSF effects.

CHAPTER 9

Conclusions of Part II

In Chapter 2, we posed two questions. The first of these was what effect PSFs have on the measurement of the correlation parameters of plasma turbulence (fluctuation amplitude, $\overline{\delta I/I}$, radial, $\ell_{r|B}$, and poloidal, $\ell_{Z|B}$, correlation lengths and wavenumbers, $k_{r|B},\ k_{Z|B}$, correlation time, $\tau_{c|B}$, and apparent poloidal velocity, $v_{\mathrm{pol}|B}$) using BES systems. The culmination of the analysis to answer this question occurs in Chapter 6, where it was found that:

1. The measured fluctuation amplitude (Section 2.1.1) of the intensity field differs from the fluctuation amplitude of the density field by a linear factor that is dependent on the area of the PSFs.

2. The measured radial correlation length (Section 2.1.4) of the intensity field can be significantly longer than the true radial correlation length of the density field, because the latter was often similar to the size of the PSFs.

3. As the poloidal correlation lengths are measured to be longer than the PSF length the effects of the PSFs on them is less significant than on the radial correlation lengths.

4. The tilt angle of the correlation function changes significantly due to PSF effects, and can even change sign.

5. The CCTD method for measuring the correlation time and apparent poloidal velocity (Section 2.1.2) can also be affected by PSF effects, as has been shown in Chapter 8.

In the process of investigating how to quantify these effects, we have developed

1. a new method for measuring the poloidal correlation length using information from a fit to the time-delayed auto-correlation function, which is subsequently used to help constrain the fit to the zero-time-delay spatial correlation function (see Section 2.1.4); and

2. a model of fluctuating fields (Section 6.1 and Appendix B) that uses randomly distributed perturbations to generate time series that real PSFs can be applied

to by numerically evaluating the integral (2.1); this model of fluctuating fields could be used to test instrument function effects on fluctuating fields of various kinds, including density, temperature, potential, etc. on other devices and aid the development of new turbulence diagnostics.

The second question posed in the Chapter 2 was whether it was possible to correct for the PSF effects identified above. Below we enumerate the findings in response to this question.

1. A simple, analytic method has been developed, designed to reconstruct the fluctuation amplitude (5.16) and the spatial correlation parameters (7.1-7.5) of the density field from measurements of the correlation parameters of the intensity field and the principal-component lengths and inclination angle of the PSFs; assuming a Gaussian model shape for the PSFs (Section 4.4). This is described in Section 7.1 and has been tested successfully on gyrokinetic simulations of turbulence in Section 7.4.

2. Our reconstruction method also provides a definition of the spatial resolution limits (7.6) and (7.7), of a BES system in terms of the principal components of the PSFs; see Section 7.3. In addition to post-hoc testing of the validity of measurements, these equations can also be used to optimise the design of new BES systems.

3. In Section 5.3, we found that the CCTD method measures exactly the plasma-frame correlation time of the turbulence and is unaffected by PSF effects, under the assumptions that the Lagrangian lifetime of individual perturbations is of order a/ρ_i longer than the time taken for a perturbation to be advected past the detector array by the bulk toroidal velocity, that the Mach number associated with the toroidal rotation is small, and that any fluctuating radial velocity is smaller than the bulk toroidal velocity by at least ρ_i^2/a^2.

4. The fluctuating radial velocity in gyrokinetic simulations of plasma turbulence in MAST is only ρ_i/a smaller than the bulk toroidal velocity. In Section 8.2, we showed that, in this case, the CCTD method measured a correlation time that was a combination of both Lagrangian and Eulerian times. The (Eulerian) eddy-turn-over time, in addition to depending on the fluctuating radial velocity, depends on the spatial scales of the turbulence and, therefore, provides a means through which PSFs can affect the measurement of the correlation time.

5. Due to the limitations of our model of fluctuating fields and our Gaussian-model PSFs, which are discussed in Section 8.3, it is not possible to reconstruct

the laboratory-frame correlation time precisely. Nevertheless, in Section 8.2, we have provided an estimate of the error on the measured correlation time that is associated with PSF effects.

6. The poloidal-velocity measurement is dominated by the bulk toroidal velocity. In Section 8.4, we saw that while it was affected by the real PSFs, these effects were, at least, ρ_i/a smaller than the bulk toroidal velocity. Therefore, within an accuracy of 10%, no corrections are required for measurements of the toroidal velocity.

The method we have developed in this part of the thesis can now be applied to turbulence measurements, as has been done, for example, in Figure 2.3(b), where the corrected spatial correlation function is plotted for real BES measurements from MAST shot #28155 and shows that both the tilt angle of the correlation function and the radial correlation length undergo substantial correction from the raw measured values. This measurement, and others, from the MAST BES will be used in Chapter 11 to investigate how flow shear affects the correlation parameters of turbulence.

We finish by noting that these results are not restricted in applicability just to MAST or just to spherical tokamaks. For example, the PSFs for the BES system on the conventional-aspect-ratio device DIII-D [93] can be of a similar size to the measured spatial correlation functions [87, 80], just as is the case for MAST turbulence and PSFs discussed here. Therefore, as discussed in [80], accounting for PSFs is also important for such devices. Indeed, using our method with the DIII-D BES data would probably produce better reconstructions of the correlation parameters of the turbulent density field than for the MAST BES, because the spatial variation of the PSFs across the BES array is smaller in DIII-D, due to the smaller variation in the pitch angle of the magnetic field, and, therefore, the assumption that all the PSFs are the same is better satisfied.

Part III

The effect of flow shear on turbulence

CHAPTER 10

Introduction

Mean flow shear associated with toroidal differential rotation is believed to play an important role in the suppression of turbulence and of the resulting transport in tokamak plasmas [47, 33, 94], most notably in the enhanced confinement regimes of the H-mode [42, 43] and Internal Transport Barriers (ITBs) [95, 96, 97]. A previous study of MAST plasmas [6] found that there was a significant correlation between higher flow shear and higher temperature gradients, suggesting reduced transport; the same trend has been reported in numerical simulations [19]. However, pinning down experimentally a precise manifestation of the effect of flow shear on the local properties of the turbulence, which, presumably, causes the transport, proved to be difficult [28] and remains so. In this part of the thesis, we show, both experimentally and numerically, that the flow shear does significantly alter the properties of plasma turbulence. Besides being an essential step towards learning why and how it does so and, therefore, how turbulent transport could be manipulated in practice, it is also of fundamental physical interest to quantify and understand how the statistical properties of a turbulent plasma respond to flow shear.

Let us start by observing that, in the absence of flow shear, the local dynamics of perturbations to an underlying Maxwellian equilibrium is constrained by a type of reflection symmetry, which follows from the up-down symmetry of the magnetic configuration [98, 99]. In the presence of flow shear, this symmetry will be broken and we shall see that the signature effects of the flow shear can be understood in terms of this symmetry breaking. Let us explain this more quantitatively.

Tokamak plasmas' local departures from equilibrium are described by the gyrokinetic theory (for a recent review, see [70]). The gyrokinetic equation (1.6) determines the evolution in time, t, of the perturbed distribution function of the gyrating particles, $h(x, y, z, v_\perp, v_\parallel, t)$, where x is the ("radial") coordinate perpendicular to a flux surface, z is the coordinate along a field line, y is the "binormal" (or "poloidal") coordinate, and $(v_\perp, v_\parallel)$ are the velocity components perpendicular and parallel to the magnetic field; the third velocity-space coordinate, the gyrophase angle, is averaged over in gyrokinetics. In an up-down symmetric equilibrium, with no toroidal rotation, the gyrokinetic equation is invariant with respect to the trans-

formations [98, 99]:

$$(x, y, z) \to (-x, y, -z), \quad v_\parallel \to -v_\parallel,$$
$$h \to -h, \quad \delta\varphi \to -\delta\varphi, \quad A_\parallel \to A_\parallel, \quad \delta B_\parallel \to -\delta B_\parallel, \tag{10.1}$$

where $\delta\varphi$ is the fluctuating part of the electrostatic potential, $A_\parallel$ is the perturbed parallel magnetic potential, and $\delta B_\parallel$ is the perturbed parallel magnetic field.

10.1 Symmetry of the field distribution

If a stochastic (turbulent) local state of a tokamak plasma is subject to the symmetry (10.1), an immediate consequence is that positive and negative amplitudes of h, $\delta\varphi$ and, therefore, via (1.8), of the density perturbation δn (which is the most experimentally accessible fluctuating field), must occur with the same probability, i.e., the distribution of $\delta n/n$ must be symmetric (even with respect to positive and negative $\delta n/n$). A finite flow shear breaks the symmetry of the gyrokinetic equation under the radial reflection $x \to -x$, allowing this distribution to become skewed towards either over- or underdensities.

In what follows, we will show both experimentally (Section 11.4) and numerically (Section 12.2) that this is indeed what happens, although how pronounced the skew is depends very strongly on the distance from the nonlinear stability threshold, with symmetry essentially restored far from it (Section 12.3). Our experimental proxy for the density field is the fluctuating intensity field measured using the Beam Emission Spectroscopy (BES) diagnostic [54] on the Mega-Amp Spherical Tokamak (MAST) [50, 100], while numerically the density field is computed using gyrokinetic simulations of a MAST plasma [40] that employ the local flux-tube code GS2.

10.2 Symmetry of the correlation function

Another consequence of the symmetry (10.1), this time relating to the spatial properties of the turbulent fluctuations, is that the two-point spatial correlation function of (for example) the fluctating density field in the (x, y) plane must be symmetric (even) with respect to reflection in the radial coordinate $x \to -x$. This symmetry too is broken when flow shear is present: the correlation function develops a finite tilt.

Indeed, consider the convective time derivative of the distribution function, which incorporates toroidal rotation (in the gyrokinetic equation, this derivative is equal to the evolution operator incorporating various drifts, nonlinearities and drive terms [70]):

$$\frac{\partial h}{\partial t} + \mathbf{u} \cdot \nabla h = \frac{\partial h}{\partial t} + x\gamma_E \frac{\partial h}{\partial y}, \tag{10.2}$$

where the toroidal rotation is locally approximated by $\mathbf{u}(x) = \mathbf{u}_0 + x\gamma_E\hat{\mathbf{y}}$, we assume that we are in a frame rotating with the $x = 0$ flux surface ($\mathbf{u}_0 = 0$), and γ_E is the flow shear (see the Appendix of [40] for a concise description of this term in the local flux-tube gyrokinetic equation). Under the transformations (10.1), the two terms in (10.2) have opposite signs, hence the breaking of the reflection symmetry.

The effect of the shear term in (10.2) on the properties of turbulence is best elicited by making the coordinate transformation into the "shearing frame" (e.g., [39, 18, 92])

$$x' = x, \quad y' = y - x\gamma_E t, \quad z' = z, \quad t' = t, \tag{10.3}$$

under which the convective derivative (10.2) becomes simply $\partial/\partial t'$. It is then legitimate[1] to represent the perturbed distribution (and all other fluctuating fields) as a Fourier sum

$$h = \sum_{k'} h_{k'}(t') e^{i\mathbf{k}'\cdot\mathbf{r}'} = \sum_{k'} h_{k'}(t') e^{i\mathbf{k}(\mathbf{k}',t')\cdot\mathbf{r}}, \tag{10.4}$$

whence, by comparing the exponents, the "Eulerian" wave number $\mathbf{k}$ can be expressed as a function of the "Lagrangian" wave number $\mathbf{k}'$ and time as

$$k_x = k'_x - k'_y\gamma_E t', \quad k_y = k'_y. \tag{10.5}$$

Thus, in the presence of flow shear, the radial wave number grows secularly in time. If a typical perturbation has a life time τ_{life}, then, using (10.5), we can estimate the typical value of the radial wave number of turbulent fluctuations to be

$$k_x \sim k_y\gamma_E\tau_{\text{life}}. \tag{10.6}$$

This tendency for perturbations with a given k_y to have a certain non-zero k_x (whose relative sign to k_y is set by the sign of the shear γ_E) manifests itself as a tilt in the two-point correlation function, with an angle

$$\Theta = -\arctan\left(\frac{k_x}{k_y}\right). \tag{10.7}$$

The presence of a non-zero tilt $\Theta \neq 0$ is a spatial manifestation of the symmetry breaking due to flow shear.

Tilting of the spatial correlation function by flow shear has been observed before, mainly in the edge of tokamak plasmas, with reports of the elongation [101] and the breaking apart [102] of turbulent perturbations. Similar observations have also been made in linear devices [103]. In the core region of a plasma, on the conventional-aspect-ratio tokamak DIII-D, a small tilt ($\sim 10^\circ$) of the spatial correlation function has been reported and attributed to flow shear [80]. Below, we will show, again both experimentally (Section 11.3) and numerically (Section 12.1), that flow shear on

[1] Ignoring for simplicity the effect of the magnetic shear [39, 92]. Note that in all measurements and simulations reported below we focus on turbulence at the mid-plane of the tokamak.

MAST can tilt the correlation function to large angles $> 45°$, making the symmetry breaking very clearly manifest and identifying the tilt as a clear signature of the presence of flow shear.

If $\gamma_E \tau_{\text{life}} \ll 1$, the life time τ_{life} will presumably be independent of γ_E and so

$$\Theta \sim \gamma_E \tau_{\text{life}} \tag{10.8}$$

will be proportional to the flow shear. Generally, at flow shears that are dynamically significant, τ_{life} will have a nontrivial dependence on γ_E. Various theories can be, and have been [44, 45, 18], constructed that provide predictions for the dependence of the life time on the flow shear. Testing such models experimentally and numerically can in principle be done by measuring the tilt Θ and then, by inverting (10.6), estimating the life time of the turbulence. We will give an example of such an analysis in Sections 11.3.4, 12.1.1, and 12.3.1, although it will fall short of validating any specific theory due to a certain deficit of currently available experimental data. Numerically, we will discover that, like skewness, the life time of the perturbations and, therefore, the tilt angle are strong functions of the distance to the threshold, with the life time becoming shorter and the tilt gentler as this distance is increased (Section 12.3).

CHAPTER 11

Symmetry breaking in experimentally measured plasma turbulence in MAST

11.1 The MAST BES system

The BES system on MAST [54] consists of a radial-poloidal (R, Z) array of 8×4 avalanche-photodiode (APD) detector channels [68], which image the South-South (SS) heating beam;[1] the separation between the detectors is approximately $2\ \mathrm{cm}$ in either direction. The detectors register Doppler-shifted D_α emission, digitised at a frequency of $2\ \mathrm{MHz}$, from collisionally excited neutral-beam atoms. The fluctuating part of the intensity of this emission is proportional to the local fluctuating number density of the plasma (at fixed mean density) [65].

The spatial localisation of the BES measurements within the beam line allows us to construct the spatial correlation function of the fluctuating density field. When this spatial correlation function is calculated (see Section 11.3.2), we assume that the turbulence is homogeneous. Since there is considerable variation of some of the equilibrium quantities across the full $16\ \mathrm{cm}$ radial extent of the BES array (see Figure 11.1), we do not use the full array, but, for the entirety of this analysis, only consider a subarray of 5×4 radial-poloidal channels, which is centred at the major radii given in Table 11.1.

The BES diagnostic is sensitive both to the local turbulent density field and to global MHD activity [28]. Since we are only interested in the former, we always select for analysis time intervals during which the magnetic signal, measured using a Mirnov coil at the outboard mid-plane of MAST [63], is below a certain threshold. The time windows that we analysed for the three representative cases described in Section 11.2 are: for the BLM case, $t \in 140.9210 + [0, 0.8340]\ \mathrm{ms}$; for the DLM case, $t \in 368.16 + [0, 2]\ \mathrm{ms}$; for the IFS case, $t \in 125.6855 + [0, 0.5995], [1.9670, 2.7110], [2.7215, 2.8095], [3.7975, 4.1255]\ \mathrm{ms}$. These time windows are long ($\gtrsim 100\times$) compared to the correlation time τ_c of the turbulence in all of these cases (see Table 11.2). As there are also 20 detector channels in a subarray, this means that a statistically large number of values of the turbulent density field is sampled.

[1] In both shots that we analyse below, the maximum SS beam power was $\simeq 2\ \mathrm{MW}$ and the maximum beam energy was $67\ \mathrm{keV}$.

11.2 Experimental example cases

Because the MAST BES instrument function size is quite close to the typical radial correlation length of the turbulence, it is quite hard to find long intervals of BES data that would be sufficiently resolved spatially in order for reliable two-dimensional correlation functions to be obtainable (see Chapter 7 and Figure 1.3). There is, therefore, relatively little data available and so it is not currently feasible to have an extensive, fully resolved parameter scan of MAST turbulence in a broad range of values of flow shear.[2] Thus, with what we have, a practical strategy for studying the effect of flow shear on turbulence is to identify a few representative cases and compare them. Namely, we would like to examine cases where there manifestly is or is not flow shear present and ask whether they are different in a clearly measurable and qualitatively understandable way.

The answer is that they are and to demonstrate this, we compare measurements made using the BES system on MAST from two times in the shot #28155. This shot is particularly useful for distilling the effect of flow shear because at $t = 0.36$ s a locked mode occurs, braking the rotation of the plasma [104]. The two times that we consider are before the locked mode (BLM) at $t = 0.141$ s and during the locked mode (DLM) at $t = 0.369$ s. Measurements of the toroidal velocity using the charge-exchange recombination spectroscopy (CXRS) diagnostic are plotted in Figure 11.1(d) for these two times. Before the locked mode, an ITB is present at the major radius $R \simeq 1.1$ m, resulting in a steep gradient in the toroidal velocity, however, the BES measurement location in that experiment is outside of the ITB at $R = 1.27$ m, where the flow shear is less strong. During the locked mode, the ITB no longer exists and the toroidal rotation profile flattens. The BES view is centred at $R = 1.33$ m for this latter analysis. In the centre of the BES viewing location, a magnetic island forms, within which there is no gradient in the toroidal rotation: see the inset of Figure 11.1(d). Therefore, by studying this shot, we have access to two clearly different regimes: one with (BLM) and one without (DLM) the flow shear.

The BLM case is quite typical of the sheared cases that can be found in the BES measurements data base—and most of this data base consists of sheared cases. Indeed, the BES diagnostic requires the SS neutral beam in order to measure the turbulence in MAST and the tangentially directed beam provides a torque to the plasma, causing it to rotate. Therefore, there is almost always some level of flow shear acting on the turbulent fluctuations measured by the BES. The DLM case is, thus, rather

[2] This is also because the range of values of shear that actually occurs in MAST is not huge anyway and, furthermore, as we will see in Section 12.3, the relevant parameter is likely not just γ_E, but the distance to the nonlinear stability threshold in a multidimensional local-equilibrium-parameter space, involving at a minimum also the ion-temperature gradient.

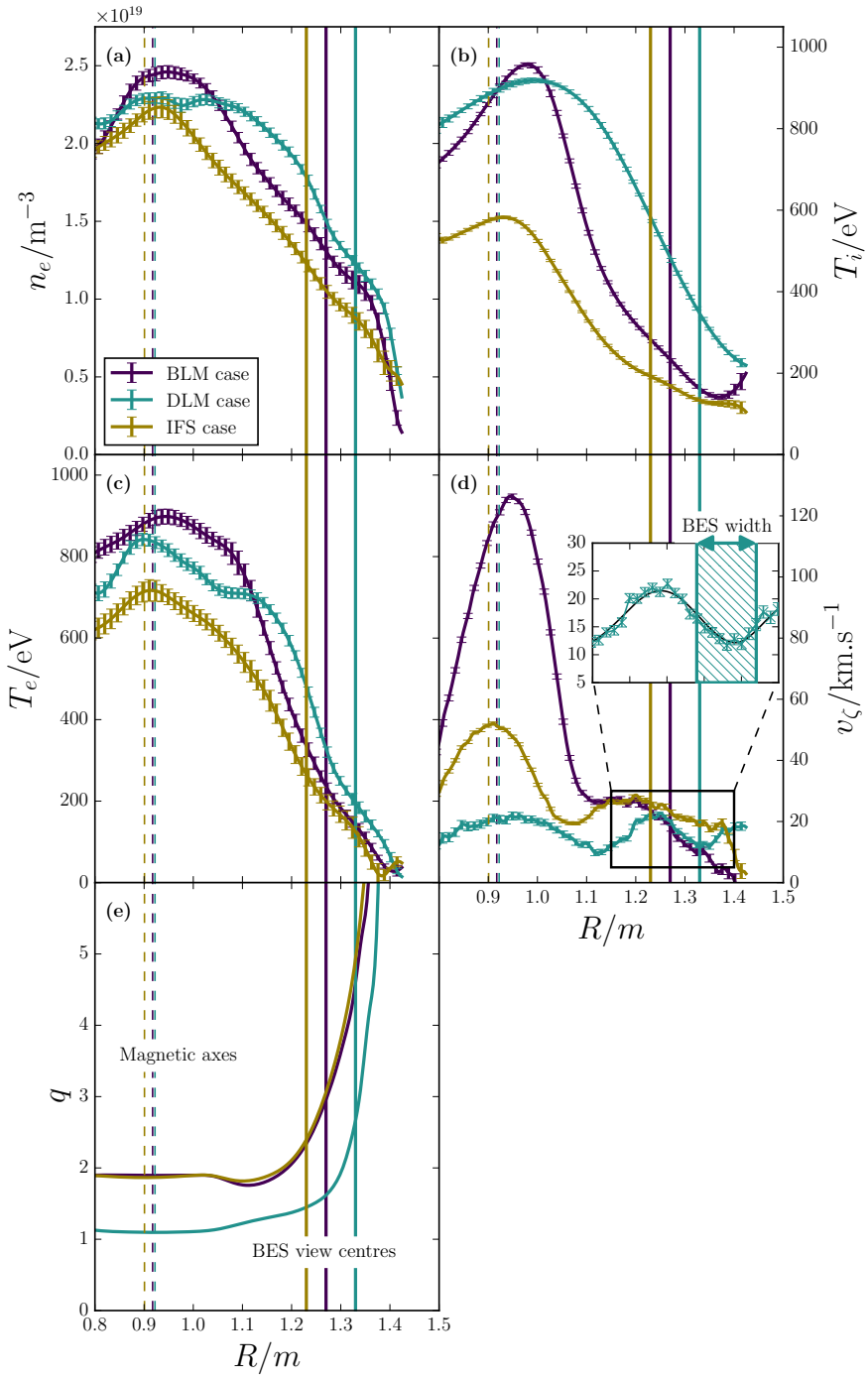


Figure 11.1: Cubic-spline-fitted equilibrium profiles for the BLM, DLM and IFS cases (described in Section 11.2): (a) electron density, measured using Thomson scattering (TS) [60, 61], (b) ion temperature, measured using Charge-Exchange Recombination Spectroscopy (CXRS) [59], (c) electron temperature (from TS), (d) toroidal velocity (from CXRS), and (e) q-profile, reconstructed by EFIT constrained by the motional-Stark-effect (MSE) [62] measurements. The vertical solid lines indicate, for each of the three cases, the centre of the BES viewing location for the subarray being used (the width of the subarray is $10\,\mathrm{cm}$). The vertical dashed lines indicate the position of the magnetic axis in each case. The black curve in the inset to (d) is the cubic-spline fit used for the calculation of (11.1).

Quantity	Symbol	BLM	DLM	IFS	EGK
Shot number	Shot	28155	28155	27278	27268
Time into shot/s		0.141	0.369	0.127	0.250
Major radius at centre of BES view/m	R	1.27	1.33	1.23	1.32
Normalised flow shear (11.1)	$\hat{\gamma}_E$	0.054	0.022	0.034	0.160
Electron-temperature gradient	a/L_{T_e}	4.8	5.3	4.3	5.8
Ion-temperature gradient	a/L_{T_i}	3.1	3.3	1.9	5.1
Electron-density gradient	a/L_{n_e}	1.7	1.9	2.1	2.6
Electron-ion temperature ratio	T_e/T_i	1.0	0.56	1.4	1.1
$\beta = 8\pi n_i T_i/B^2$	β	0.010	0.008	0.010	0.005
Minor radius/minor radius of LCFS	r/a	0.63	0.71	0.55	0.80
Safety factor	q	3.0	3.0	2.5	2.3
Magnetic shear	$\hat{s}$	2.2	5.2	1.7	4.0
Ion-ion collisionality	ν_{ii*}	0.014	0.006	0.020	0.020
Electron-ion collisionality	ν_{ei*}	0.79	0.85	0.74	0.59
Elongation	κ	1.6	1.4	1.4	1.5
Derivative of elongation	κ'	0.55	0.73	0.24	0.45
Triangularity	δ	0.22	0.19	0.21	0.21
Derivative of triangularity	δ'	0.081	0.86	0.49	0.46
Shafranov shift	Δ'	-0.33	-0.48	-0.27	-0.31
Mach number	M	0.12	0.074	0.19	0.43
Ion gyroradius/cm	ρ_i	0.88	1.1	0.78	0.66
Time normalisation $/\mu$s	$a/v_{\mathrm{th}i}$	3.8	3.2	4.4	4.0
Pitch angle of magnetic field/deg	α	23	30	21	34
Ion temperature/eV	T_i	230	350	190	220
Electron temperature/eV	T_e	250	200	270	240
Electron density/10^{19} m^{-3}	n_e	1.3	1.2	1.2	1.2
Toroidal velocity (from CXRS)/km/s	v_ζ	18	14	26	62
Toroidal velocity (from BES)/km/s	v_ζ^{BES}	13 ± 9	8 ± 4	19 ± 4	$-$

Table 11.1: Local equilibrium parameters for each of the experimental cases analysed (Section 11.2). The BLM and DLM cases are the main comparison cases discussed in Sections 11.3 and 11.4; the IFS case is first introduced in Section 11.3.5. The EGK case gives the parameters for the gyrokinetic simulations analysed in Chapter 12 and is also discussed there. Profiles of n_e, T_i, T_e, v_ζ, and q are plotted in Figure 11.1 for the BLM, DLM and IFS cases. The numerical values for these three cases are average quantities over the width of the BES subarray, whilst the values for the EGK case are taken at the centre of the BES array (those were the values used in simulations).

special, but that is the point: turbulence in MAST is rarely without a flow shear and so any such situation provides a very useful opportunity for a clean comparison. The special status of the DLM case cannot be overstated, especially due to the fact that, in such a locked mode, the characteristics of the turbulence may be sensitive to other effects that we have not been able to account for, including variations in the magnetic geometry (e.g. toroidal variation), in the local equilibrium gradients and zonal flow effects.

A third experimental example, which will be introduced in Section 11.3.5, is an intermediate-flow-shear (IFS) case, taken from shot #27278 at $t = 0.128\ \mathrm{s}$, with the BES measurement taken at $R = 1.23\ \mathrm{m}$. It represents a less clear-cut situation, which we include to highlight the range of behaviour that one encounters in MAST. While we do not claim to have identified all of the interesting cases, we did analyse a large number of intervals and the examples we have chosen do appear to us to be a worthwhile selection.

The profiles of the electron number density n_e, ion (T_i) and electron (T_e) temperatures and the safety factor q, in addition to the toroidal velocity v_ζ already discussed above, are plotted in Figure 11.1 for all three cases. In Table 11.1, a full set of equilibrium parameters is provided: the values quoted there are averages over the width of the BES subarray that we use for measurements (see Section 11.1). All three cases are plasmas with double-null-divertor (DND) geometries, and, therefore, the equilibria must be up-down symmetric, making the symmetry considerations of Chapter 10 relevant.

Together, the three cases described above provide examples across a typical (for MAST) range of values of the normalised flow shear

$$\hat{\gamma}_E = \frac{\gamma_E}{v_{\mathrm{th}i}/a} = -\frac{r}{q}\frac{\mathrm{d}\omega}{\mathrm{d}r}\frac{a}{v_{\mathrm{th}i}}, \tag{11.1}$$

where q is the safety factor, r is the distance from the magnetic axis to the BES viewing location, $v_{\mathrm{th}i} = \sqrt{2T_i/m_i}$ is the ion thermal speed, T_i the ion temperature, m_i the Deuteron mass, a the minor radius of the last-closed flux surface (LCFS), $\omega = v_\zeta/R$ the toroidal rotation frequency, v_ζ the toroidal velocity and R the major radius at the BES viewing location (these quantities can be found in Table 11.1). The definition (11.1) is the same as that used as an input parameter for the gyrokinetic simulations using GS2, however, it is different from the physical flow shear (1.5) by a factor of qRB_Z/rB, where B is the total magnitude of the magnetic field, and B_Z its poloidal component. In the large-aspect-ratio limit, this factor is close to unity, but, for a spherical tokamak such as MAST, there is a significant difference. For consistency with the standard definition of γ_E used in simulations [40] (Chapter 12), we will always use (11.1) as our flow-shear parameter.

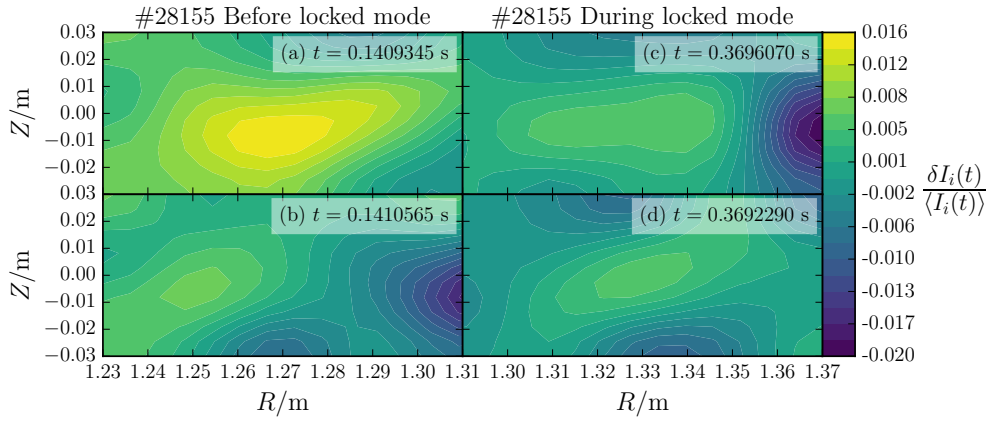


Figure 11.2: Snapshots of the raw (but 2D-spline-interpolated) BES fluctuating-intensity signal $\delta I_i/\langle I_i\rangle$ from shot #28155 at: (a) $t = 0.1409345$ s, (b) $t = 0.1410565$ s, (c) $t = 0.3696070$ s, (d) $t = 0.3692290$ s. Times (a) and (b) occur during the BLM time period (significant flow shear) and times (c) and (d) occur during the DLM time period (no flow shear). The correlation functions of these two cases are given in Figure 11.3, which include these snapshots in the temporal average.

Note that, from inspecting the raw velocity profile in Figure 11.3(d), we know that the flow shear in the DLM case is approximately zero across half of the BES subarray, however, the value for the DLM flow shear given in Table 11.1 is nearly two thirds of the flow shear for the IFS case. This apparent discrepancy occurs because a cubic-spline fit (see inset of Figure 11.1(d)) is performed in order to calculate the radial derivative of the toroidal velocity, and the spline fit underestimates the flatness (or, equivalently, the width) of the region due to the magnetic island. The resulting value of the flow shear, calculated as the average over the BES subarray, depends sensitively on the point at which the spline fit determines the minimum to occur, as the sign of the flow shear changes at this point, resulting in significant uncertainty in the calculated value of the flow shear in this case.

11.3 Two-dimensional spatial structure of the turbulence

11.3.1 Instantaneous turbulent density field

Before discussing statistical properties of turbulence, let us inspect the instantaneous spatial structure of the fluctuating density field during the time windows being studied. In Figure 11.2, example snapshots are plotted of the BES-measured intensity amplitude at certain chosen times. Each channel has been normalised by

its own mean, so these are essentially snapshots of the relative density perturbation $\delta n/n$.

While we know (and it will also become very obvious in Section 11.3.2) that the BLM case [Figures 11.2(a) and (b)] has flow shear and the DLM case [Figures 11.2(c) and (d)] does not, it is not easy (indeed, well-nigh impossible) to deduce that by inspection of such snapshots or by watching the full time-evolution sequences for these two cases. Indeed, comparing Figures 11.2(a) and (c), we see that similar untilted (and so seemingly unsheared) structures occur in both the BLM and the DLM cases; conversely, comparing Figures 11.2(b) and (d), we also see that similar tilted structures also occur in both cases.[3] Therefore, the morphology of particular realisations of the turbulence does not reveal in any especially glaring way that turbulence is different between the two cases. Statistically, however, it is very different, as we are about to discover.

11.3.2 Spatial correlation function

We now characterise the average spatial structure of turbulence using the spatial correlation function of the BES-measured intensity signal. Denoting by $I_i(t)$ the time-dependent intensity measured by the BES detector channel i, we split this signal into mean (averaged over time) and fluctuating parts, as in (2.2),

$$I_i(t) = \langle I_i(t) \rangle + \delta I_i(t). \tag{11.2}$$

The two-point correlation matrix of the fluctuating intensity field is then (2.4)

$$C_{ij} = \frac{\langle \delta I_i(r_i, Z_i) \delta I_j(r_j, Z_j) \rangle}{\sqrt{\langle \delta I_i^2(r_i, Z_i) \rangle \langle \delta I_j^2(r_j, Z_j) \rangle}}, \tag{11.3}$$

where r_i, and Z_i are the radial and poloidal (vertical) locations of the detector channel i, respectively, and the angle brackets again denote time averages (the autocorrelation functions for each detector, calculated for $i = j$, are corrected for photon-noise effects as described in [28] and at the beginning of Section 11.4). Assuming the turbulence is (approximately) spatially homogeneous across the BES subarray used for our analysis (see Section 11.1), its two-point correlation function depends only on the relative distances between channels $\Delta r = r_i - r_j$ and $\Delta Z = Z_i - Z_j$. We reconstruct this correlation function from the correlation matrix (11.3) by considering the relevant ranges of values of Δr and ΔZ and using the following fitting function

$$C(\Delta r, \Delta Z) = p + (1 - p) \exp\left[- \left(\frac{\Delta r^2}{\ell_r^2} + \frac{\Delta Z^2}{\ell_Z^2} \right) \right] \cos\left[k_r \Delta r + k_Z \Delta Z \right], \tag{11.4}$$

[3] In the case with no flow shear, instantaneous tilted structures could be due to (and indeed be a signature of) a fluctuating zonal flow shearing the density field; this also happens in numerical simulations with $\gamma_E = 0$, as discussed in Section 12.1.2.

which is the same functional form as (2.9) used in Part II. The parameter p is used to account for global modes [28], as well as for fluctuations in the neutral beam [81]. As we have selected times during which there is no MHD activity (see Section 11.1), the value of p should be small. Indeed, in all measured cases it is at most a few percent, therefore also indicating that neutral-beam fluctuations do not affect the measurements.

The fit (11.4) allows us to extract the spatial correlation parameters of the turbulence: the radial, ℓ_r, and poloidal, ℓ_Z, correlation lengths and the radial, k_r, and poloidal, k_Z, wavenumbers. Operationally, in order to constrain the fit (11.4), we fix the product $k_Z\ell_Z$, which is determined from the two-time, single-point correlation function of the intensity field (see Section 2.1.4 and Appendix A). To obtain correct values of the spatial correlation parameters of the true density field, one must take account of the finite spatial resolution of the BES system, which is quantified in terms of the point-spread functions (PSFs) of its detector channels. How to do this systematically is worked out in Part II; here ℓ_r, ℓ_Z, k_r, and k_Z are all corrected for PSF effects using the technique of Chapter 7.

Physically, we would like to work with the correlation function in terms of point separations in the plane (x, y) perpendicular to the mean magnetic field, where x is the coordinate perpendicular to the flux surface (so, in the outboard mid-plane of the tokamak, the same as the radial coordinate) and y is the "binormal" coordinate, perpendicular both to the field and to the x direction (the plasma frame of Section 3.1). Assuming that the correlation length of the fluctuating density field along the magnetic field is long compared to ℓ_Z, we then convert the correlation function (11.4) to

$$C(\Delta x, \Delta y) = \exp\left[-\left(\frac{\Delta x^2}{\ell_x^2} + \frac{\Delta y^2}{\ell_y^2}\right)\right] \cos\left[k_x \Delta x + k_y \Delta y\right], \tag{11.5}$$

where $\ell_x = \ell_r$, $\ell_y = \ell_Z \cos\alpha$, $k_x = k_r$, $k_y = k_Z/\cos\alpha$, and $\alpha = \arcsin(B_Z/B)$. These correlation lengths and wave numbers are given in Table 11.2. The spatial correlation function (11.5) is plotted in Figures 11.3(a) and (b) for the BLM and DLM cases, respectively. Note, in this part of the thesis we have dropped all subscripts for these correlation parameters (P, L, and B), and from now on all results are reported in the above defined plasma frame coordinates.

11.3.3 Symmetry breaking

The difference between the BLM case (with flow shear) and the DLM case (without flow shear) is manifest: the BLM correlation function is highly tilted whereas the DLM one is very nearly even in Δx. The tilt can be defined in terms of the tilt angle (10.7), where we now use the k_x and k_y parameters of the fitting function (11.5).

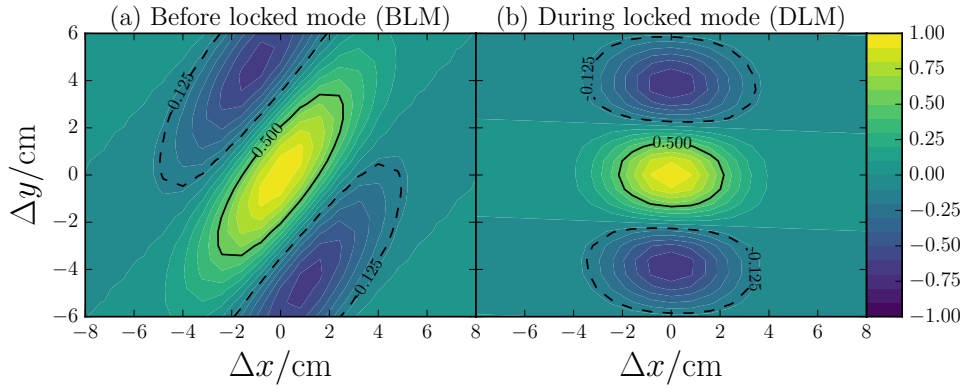


Figure 11.3: Spatial two-point correlation function (11.5) of the fluctuating density field for (a) the case before the locked mode (BLM, with flow shear) and (b) the case during the locked mode (DLM, no flow shear), both described in Section 11.2. The raw measurement for the DLM case is shown in Figure 2.3(a). Table 11.2 shows the parameters of these correlation functions calculated by fitting (11.4) to the spatial correlation function (11.3), correcting for PSF effects, and transforming into the (x, y) coordinates perpendicular to the magnetic field. These correlation functions should be compared to the correlation functions of the numerically simulated turbulence in Figure 12.1.

Name	BLM	DLM	IFS
$\hat{\gamma}_E$	0.054 ± 0.006	0.02 ± 0.04	0.034 ± 0.012
$\overline{\delta n/n}$	0.011 ± 0.002	0.03 ± 0.01	0.020 ± 0.003
Skewness	0.21 ± 0.03	0.01 ± 0.03	-0.17 ± 0.02
ℓ_x/ρ_i	3.9 ± 1.5	2.4 ± 0.6	3.3 ± 0.2
ℓ_y/ρ_i	9.7 ± 0.8	6.2 ± 0.7	10.7 ± 1.2
$k_x\rho_i$	-0.51 ± 0.14	0.03 ± 0.20	-0.21 ± 0.08
$k_y\rho_i$	0.43 ± 0.03	0.82 ± 0.03	0.43 ± 0.05
Tilt: Θ/deg	50 ± 8	-2 ± 15	26 ± 9
$\tau_{\text{life}}/(a/v_{\text{th}i})$	22 ± 7	$-$	14 ± 8
$\tau_{\text{c}}/(a/v_{\text{th}i})$	3 ± 2	6 ± 2	3 ± 1
τ_{c}/μs	12 ± 9	20 ± 6	19 ± 4

Table 11.2: Correlation parameters for BLM, DLM, and IFS cases, all described in Section 11.2. The correlation functions (11.5) with these parameters are shown in Figures 11.3 and 11.4. All lengths are normalised by the ion gyroradius $\rho_i = v_{\text{th}i}/\Omega_i$ ($v_{\text{th}i}$ is the ion thermal speed, Ω_i the ion cyclotron frequency), all times to $a/v_{\text{th}i}$; the values of both of these can be found in Table 11.1. The rms amplitude $\overline{\delta n/n}$ of the fluctuating density field is calculated from the rms amplitude $\overline{\delta I/I}$ of the fluctuating intensity field, as defined by (11.8), using the method described in Chapter 7. The skewness is calculated using (11.9) for the distribution of δI. The life time τ_{life} is defined in (11.6); the correlation time τ_{c} was calculated using the CCTD method [79, 23].

The values of Θ are given in Table 11.2. Thus, in line with the theoretical discussion in Section 10.2, the statistical symmetry of the plasma turbulence under radial reflection is broken in the presence of flow shear.

An interesting aside is the change in the radial correlation length between the BLM and DLM cases, where, as the flow shear decreases, the radial correlation length decreases by a factor of 1.6. This is contrary to how flow shear is believed to affect the radial correlation length of turbulence, perhaps suggesting that some other equilibrium factor (as discussed in Section 11.2) may be affecting the turbulence in the DLM case. However, we also note that this difference is within the uncertainty of the measurements, indicating that this is a less significant difference than that of the observed change in the tilt angle of the correlation function.

11.3.4 Correlation times and flow shear

As promised in Chapter 10, we may calculate the effective "life time" of a sheared structure, defined, in view of (10.6), by

$$\tau_{\text{life}} \equiv \left| \frac{k_x}{\gamma_E k_y} \right| = \left| \frac{\tan \Theta}{\gamma_E} \right|. \tag{11.6}$$

The values of this quantity for our experimental cases are given in Table 11.2. We also give there the correlation time τ_{c} of the fluctuating density field determined from its time-correlation function using the cross-correlation time delay (CCTD) method [79, 23]. We see that the values of τ_{life} and τ_{c}, while not wildly disparate, cannot really be declared to agree. We are going to be relaxed about this problem: first, because both the CXRS value of γ_E and the CCTD value of τ_{c} are subject to large errors (regarding the reliability of the CCTD method in the presence of non-negligible PSFs, see Chapter 8), and secondly, because (10.6) is obviously a relation allowing an arbitrary constant of order unity. However, if the measurement of γ_E is viewed as reliable, the life time defined by (11.6) can be meaningfully used as an effective measure of the (Lagrangian[4]) correlation time for comparative studies of turbulence at different equilibrium-parameter values, as it will be in Sections 12.1.1 and 12.3.1.

Correlation functions of MAST turbulence generically exhibit a tilt when flow shear is present, with a range of values of Θ—we have checked this in a number of

[4]The correlation time appearing in (10.6) is probably best interpreted as a Lagrangian correlation time (life time of a moving and sheared "eddy", which is reflected in our notation for τ_{life}), whereas the correlation time τ_{c} determined from the BES-measured time correlation function is obviously the Eulerian correlation time (albeit in the frame moving with the overall mean toroidal rotation velocity [23] — see discussion in Section 8.1). While in conventional (Kolmogorov-like) strong turbulence, one expects $\tau_{\text{life}} \sim \tau_{\text{c}}$, the relationship between the two times may be more subtle in a turbulent state where long-lived coherent structures play a prominent role—it was argued in [40] that MAST turbulence is in just such a state close to the (nonlinear) stability threshold (this will be further discussed in Section 12.2.1).

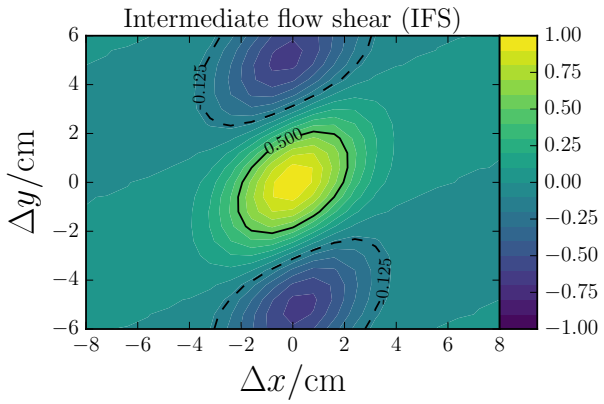


Figure 11.4: Same as Figure 11.3, but for the IFS case, whose normalised flow shear (11.1) is $\sim 40\%$ smaller than in the BLM case—the tilt of the correlation function is also smaller (see Table 11.2).

experimental cases, not shown here. This is a reliable feature, to the extent that it could be thought of as a way to find out whether a flow shear is present.[5] Given that the values of γ_E might not be computed very precisely from CXRS measurements of the rotation profiles, one might wonder whether in fact a more reliable (and dynamically relevant) measure of the local flow shear would be obtained from the tilt angle of the spatial correlation function and the correlation time τ_c computed from the time-correlation function, viz., $\gamma_E^{(\mathrm{eff})} = \tan\Theta/\tau_c$ (ignoring here the difference between Lagrangian and Eulerian correlation times; note that $\gamma_E^{(\mathrm{eff})}$ could also be the local shear associated with zonal flows, as will be discussed in Section 12.1.2).

11.3.5 Case of intermediate flow shear

The measurement uncertainties discussed above and a relatively limited range of values of γ_E for which well-resolved BES data is available[6] preclude us from being able to provide here a straightforward Θ vs. γ_E parameter study. Generally speaking, larger γ_E will give larger Θ, but the spread is large (in Section 12.3, we will argue that this is because Θ is a function not just of γ_E but also of how far from the stability threshold the system is). The case of relatively low, but measurable, values of shear is perhaps an interesting benchmark as in this case we expect the tilt to be small. We have found such a case, case IFS, described in Section 11.2 and documented in

[5] Note that the flow shear need not be dynamically significant in order for the correlation function to be tilted. At low shear, the tilt (small in this limit) would be a "passive" feature, proportional to γ_E, as per (10.8); see further discussion in Section 12.3.1.

[6] I.e., in the context of this study, the data for which the tilt angle Θ can be reliably calculated—the limiting factor is, in most cases, the radial resolution, with values of ℓ_x never very far from the distance between the BES detector channels and from the effective size of the PSFs (see discussion of resolution limits in Chapter 7).

Tables 11.1 and 11.2. This has normalised flow shear (11.1) that is $\sim 40\%$ smaller than that in the BLM case (with its other equilibrium parameters not differing in any particularly remarkable way from the BLM ones).

The correlation function for the IFS case is shown in Figure 11.4. Its tilt is in between that of the BLM and DLM cases and its $\tau_{\rm life}$ is shorter than for the stronger-sheared BLM case (see Table 11.2). Clearly, two points a parameter scan do not make, but this is the best one can do with current data. The salient message is that the transition from stronger flow shear (BLM) to no flow shear (DLM) is gradual in parameter space, with the tilt angle passing through a range of values—and a more comprehensive parameter study ought to be on experimentalists' agenda. The most interesting outcome from such a study would be the dependence of $\tau_{\rm life}$ on γ_E, telling us how the dynamical properties of turbulence change with shear (cf. Section 12.3.1).

11.4 Distribution of fluctuation field

In Section 10.1, we argued that the breaking of the radial-reflection symmetry by the flow shear can lead to the breaking of the symmetry (evenness) of the distribution of the fluctuating density and, therefore, BES-measured intensity field. Here we show that this is indeed the case.

We consider the fluctuating part $\delta I_i(t)$ of the intensity field (11.2) and, for each detector channel i, normalise it by its own standard deviation

$$\delta I_i^{\rm std} = \left[\langle \delta I_i^2(t)\rangle - \langle \delta I_{{\rm noise},i}^2\rangle\right]^{1/2}, \tag{11.7}$$

where we have subtracted the mean square amplitude $\langle \delta I_{{\rm noise},i}^2\rangle$ of the fluctuating part of the photon noise signal (determined from the signal at each channel during the calibration of the instrument [28]). The angle brackets signify averages over time. The normalisation to $\delta I_i^{\rm std}$ is required in order to account for a degree of variation of this quantity across the BES subarray used for our analysis. The total standard deviation (total rms fluctuation amplitude) over all $N = 20$ channels in the subarray is

$$\overline{\delta I/I} = \left[\frac{1}{N}\sum_{i=1}^{N}\left(\frac{\delta I_i^{\rm std}}{\langle I_i\rangle}\right)^2\right]^{1/2}. \tag{11.8}$$

This quantity is proportional to the total rms fluctuating density field $\overline{\delta n/n}$, whose value can be reconstructed from it by correcting for PSF effects (see Chapter 7) and is given in Table 11.2. The distribution of the normalised fluctuating intensities $\delta I_i/\delta I_i^{\rm std}$ can be affected by several different known experimental effects, including MHD activity, radiation spikes, and PSF effects. A discussion of these effects and how they have been accounted for in our present analysis is given in Appendix E.

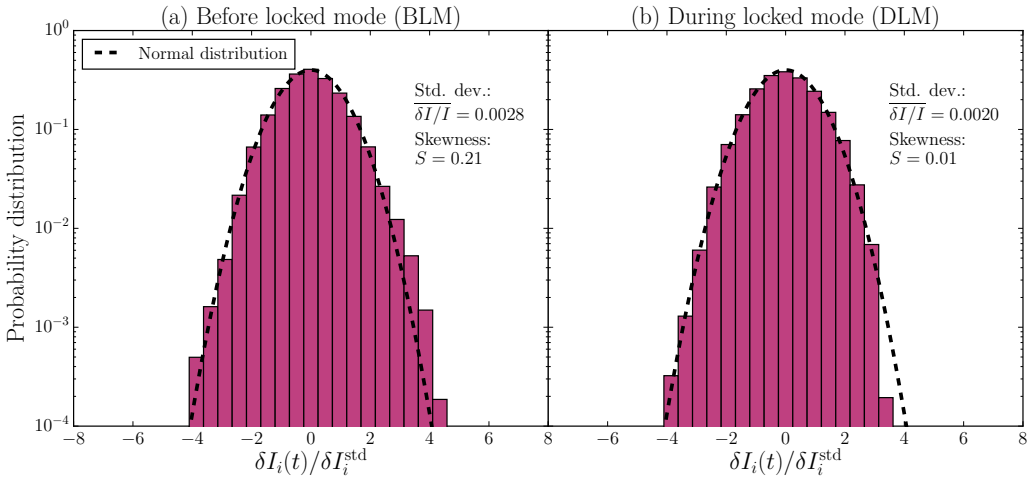


Figure 11.5: Distribution of the fluctuating intensity field for (a) the case before the locked mode (BLM, with flow shear) and (b) the case during the locked mode (DLM, no flow shear), both described in Section 11.2. For each detector channel, δI_i is normalised by its own root-mean-square (standard deviation) value (11.7). The black-dashed line in each case gives the unit normal distribution. The distribution function and its skewness for the DLM case (b) were calculated from 2 (rather than 5, as in all other cases) sets of 4 poloidal BES channels, located at $R = 1.33$ m and $R = 1.35$ m, where the toroidal rotation profile is completely flat, as seen in Figure 11.1(d).

11.4.1 Symmetry breaking

In Figure 11.5, we show the probability distribution of the normalised fluctuating intensities $\delta I_i/\delta I_i^{\mathrm{std}}$ for the BLM and DLM cases. In the case without flow shear (DLM), the distribution is even with respect to positive and negative δI (and very nearly normal). In contrast, the case with shear (BLM) exhibits a relatively small, but measurable preponderance of positive δI, i.e., overdensities are statistically somewhat more common than underdensities. This can be quantified as a positive value of the skewness of the distribution[7]

$$S = \frac{1}{N}\sum_{i=1}^{N}\frac{\langle \delta I_i^3(t)\rangle}{(\delta I_i^{\mathrm{std}})^3}. \tag{11.9}$$

For the BLM case, $S = 0.21$; for the DLM case, $S = 0.01$, but this is similar to the skewness in the background emission signal, as well as to the size of the error in the determination of the skewness that occurs due to PSF effects (see Appendix E.2), so cannot be considered significant.

In Figure 11.6, we show the fluctuating-intensity distribution for the IFS case,

[7]The fluctuating part of the photon noise is Gaussian distributed [68, 23] and so does not affect the third moment of δI.

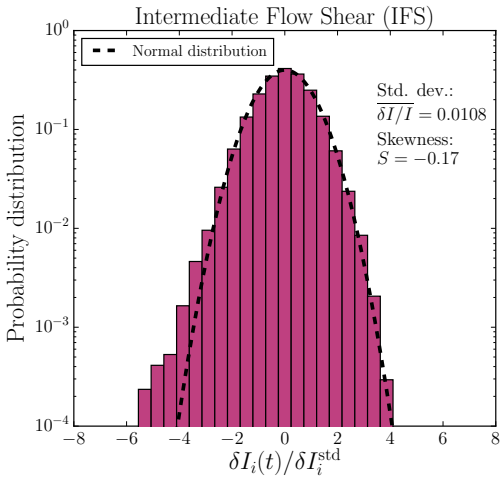


Figure 11.6: Same as Figure 11.5, but for the IFS case (lower flow shear than for BLM; see Table 11.2).

with flow shear lower than BLM, already discussed in the context of its lower tilt in Section 11.3.5. We see that the distribution is again skewed, with its skewness lower than for the BLM case (but still measurable), just as its tilt was (to identify a quantitative dependence between the skewness and flow shear, we will need to resort to simulations, in Section 12.2, as we do not have a sufficient range of data for a proper parameter scan). What is more interesting is that the sign of the skew is negative, i.e., here, underdensities are privileged compared to overdensities. Furthermore, the magnitude of the skewness is greater than what may be considered the 'noise' level, as will be seen later when considering the simulation results (Figure 12.8(b)). This emphasises the fact that, while the presence of a flow shear allows such asymmetric distributions, theory (at least in its current state) does not predict the sign of the asymmetry—we do not know how the sign of the skew depends on local equilibrium parameters. As we have neglected the effect of magnetic shear in this work, and it is known that this changes how the radial wavenumber evolves [39, 92], we postulate that the exact sign of the skewness may depend on a balance between contributions from both the magnetic shear and the flow shear.

Finally, we must stress a very strong caveat. The fact that the symmetry (10.1) is formally broken by flow shear does not necessarily imply that a skewed distribution should result, it merely allows it (in contrast to the case of zero flow shear, when a skewed distribution would clash with theory [98, 99]). Here we have demonstrated, as a proof of principle, that skewed distributions can indeed be found experimentally when flow shear is present. However, skewness is not as robust nor as inevitable an effect of flow shear as tilted correlation functions appear to be and we

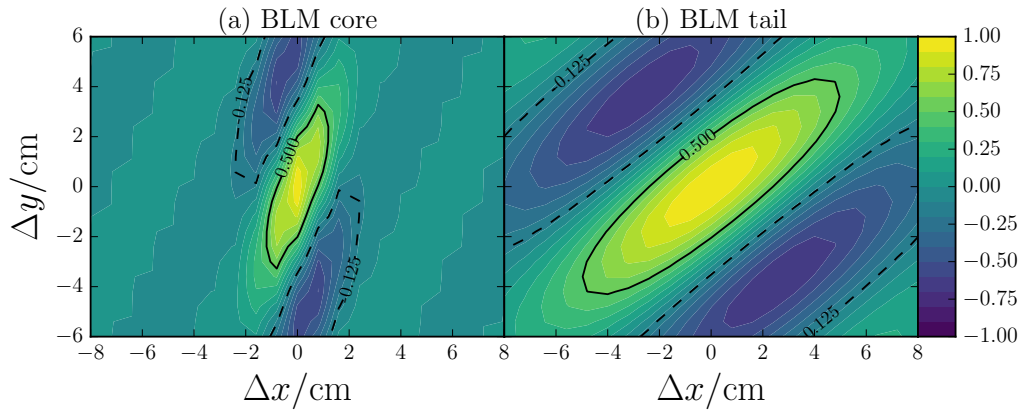


Figure 11.7: Same correlation function as in Figure 11.3(a), for the BLM case, but this time conditioned on (a) lower intensities (core of the distribution, $|\delta I_i/\delta I_i^{\mathrm{std}}| < 2.75$) and (b) higher intensities (tail of the distribution, $\max \delta I_i/\delta I_i^{\mathrm{std}} > 3$), in the way described in Section 11.4.2. The parameters of the fitting function (11.5) in each case are given in Table 11.3. The tail is manifestly less tilted than the core and also has a larger radial correlation length. These correlation functions should be compared to the ones for numerically simulated turbulence in Figures 12.6 and 12.7.

have found many experimental cases in which flow shear is present according to CXRS measurements but the skewness of the fluctuating-intensity distribution is so small that, in view of measurement uncertainties, it cannot be declared present beyond reasonable doubt. In Section 12.3, we will see, by analysing numerical simulations, that how skewed the distribution is depends quite strongly on how far from the nonlinear stability threshold the system finds itself, with only near-marginal cases showing significant skewness. Thus, while a tilt (possibly small) in the correlation function might be viewed as a signature of the presence of flow shear (as argued in Section 11.3.4), a noticeable skewness of the fluctuating-density distribution should perhaps be viewed as a signature of a sheared turbulent state being close to threshold. The physical reason for this is probably that, close to the threshold, the turbulent state in MAST is dominated (as shown in [40] and discussed in Section 12.2.1) by a finite number of long-lived, finite-amplitude coherent structures, whereas farther from the threshold, a more (evenly) distributed sea of fluctuations emerges.

11.4.2 Skewness vs. tilt: two-component turbulence?

The above discussion and the greater robustness of the tilted correlation functions than of the skewed distributions as signatures of flow shear suggest that these features describe the response to the flow shear of different types of turbulent fluctuations. Indeed, intuitively, as perturbations are sheared by the flow, their radial

wave number increases according to (10.5) and so then does $k_\perp \rho_i = (k_x^2 + k_y^2)^{1/2}\rho_i$. This will push them into a damped region of wave-number space (see, e.g., [18]), quickening their demise. It is these perturbations, which are on their way out, that would statistically contribute to the tilt in the correlation function. In contrast, one might imagine that rare but particularly strong perturbations whose presence skews the distribution of the fluctuating field, might be less vulnerable to (or simply not yet affected by) such destruction by flow shear and so would turn out to be less tilted. This view is perhaps reinforced by the observation, which we will be in a position to make when we consider the numerically simulated turbulence in Section 12.2, that the rms fluctuation level $\overline{\delta n/n}$ is significantly lower in the turbulence with flow shear than without it and so the tail of the distribution represents not some additional population appearing alongside the "core turbulence" but rather the "survivors"—sufficiently large structures that can create sufficiently large local velocity gradients to overcome the suppressing effect of the shear; these large structures would diffuse and disappear rapidly in the strong unsheared turbulence.

These speculations can be experimentally tested, if in a rather tentative manner, by constructing a correlation function conditional on the fluctuation amplitude. Indeed, the turbulent density field is continuously (and quickly) advected by the flow past our, relatively small, BES subarray, which can thus be thought of as sampling different types of turbulent structures at different times, rather than capturing a fully statistically representative spatial domain containing all types of structures at all times. Thus, we collect all snapshots of the turbulent field (such as those discussed in Section 11.3.1) in which the fluctuating intensities at all detector channels are below a certain threshold, specifically, $|\delta I_i/\delta I_i^{\rm std}| < 2.75$, and calculate the spatial correlation function of this collection, representing the "core" of the distribution, in the way described in Section 11.3.2. We repeat the same procedure for a complementary set of snapshots, in which at least one detector channel sees $\delta I_i/\delta I_i^{\rm std} > 3$, to extract the correlation parameters of the "tail" of the distribution. This analysis is necessarily crude, because the reduced number of snapshots (especially for the tail) reduces the quality of the statistics and the size of the BES window may have an effect that we cannot study systematically. Proceeding with it nevertheless, we find that the tilt angle for the core of the distribution in the BLM case is noticeably larger than in the tail (and also that the radial correlation length ℓ_x in the tail is much larger than in the core; see Table 11.3). For the DLM case, there is no significant difference between the tail and the core, the tilt angle is essentially zero for both. This result appears to support the line of reasoning proposed above, although obviously a much more extensive study of a large number of well-resolved cases with good statistics is called for.

Case	BLM core	BLM tail	IFS core	IFS tail
Condition	$\lvert\delta I_i/\delta I_i^{\mathrm{std}}\rvert < 2.75$	$\delta I_i/\delta I_i^{\mathrm{std}} > 3$	$\lvert\delta I_i/\delta I_i^{\mathrm{std}}\rvert < 2.75$	$\delta I_i/\delta I_i^{\mathrm{std}} < -3$
No. of snapshots	1434	123	3065	206
ℓ_x/ρ_i	1.9 ± 0.2	8.4 ± 0.3	2.9 ± 0.1	4.8 ± 0.3
ℓ_y/ρ_i	9.2 ± 0.1	9.2 ± 0.3	10.4 ± 0.1	11.0 ± 0.2
$k_x\rho_i$	-1.00 ± 0.14	-0.36 ± 0.01	-0.18 ± 0.02	-0.35 ± 0.02
$k_y\rho_i$	0.44 ± 0.01	0.43 ± 0.01	0.46 ± 0.01	0.43 ± 0.01
Tilt: Θ/deg	67 ± 3	40 ± 1	22 ± 3	39 ± 2

Table 11.3: Correlation parameters of the fitting function (11.5) for the BLM and IFS core and tail conditional correlation functions (for the BLM case, they are shown in Figure 11.7). The errors given here are for the fitting procedure only. The parameters for the overall correlation functions can be found in Table 11.2. Note that the number of snapshots does not represent the number of statistically independent instances: neighbouring snapshots are separated by $0.5\ \mu$s, so it takes approximately 20 snapshots for a given structure to pass through the BES subarray (due to the apparent poloidal motion caused by toroidal rotation [23]).

The need for such a study to make our argument fully convincing (or otherwise) is accentuated by the disconcerting failure of the IFS case to agree with the core vs. tail distinction seen in the BLM case: in fact, we find that the tilt angle in the tail is larger than in the core (see Table 11.3). We do not know why the IFS case has this behaviour: whether, for example, it might be related to the lower (dynamically unimportant?) flow shear, or to the preponderance of under-, rather than overdensities in the distribution of the fluctuating field, or to the presence of zonal flows.[8] In Section 12.2.2, we will see that the trend in numerical simulations appears to be broadly consistent with the BLM case.

Cognizant of all the uncertainties and of the clearly insufficient amount of experimental evidence on offer, we conclude this section with a cautious conjecture that turbulence under the action of flow shear consists of a tilted, sheared, statistically more ubiquitous, but smaller-amplitude component and less tilted, rarer, but stronger perturbations, which skew the distribution function of the fluctuating field. We shall test this idea further in the next section.

[8] As discussed in Section 12.1.2, turbulence in MAST is expected (based on numerical simulations) to develop both zonal flows and zonal density perturbations. Locally, zonal shears will cause correlation functions to become tilted in the same way as mean flow shear does. Depending on the life time of the zonal fields and on the high-pass frequency filter (i.e., effectively, on the definition of time average in (11.2)) applied to the intensity signal (see Appendix E.1), we have found numerically that the presence of a residual zonal density perturbation in the signal can bias conditional correlation functions calculated for stronger or weaker intensities towards regions of positive or negative zonal densities, which are also regions of stronger zonal shear. One can imagine that, when the mean flow shear is weak, this could matter and lead to greater tilt angles in the tail of the distribution, as found here for the IFS case.

CHAPTER 12

Symmetry breaking in numerically simulated gyrokinetic turbulence

Having established experimentally, at least as a proof of principle, that the presence of the flow shear breaks both the spatial symmetry of the turbulence and the symmetry of the distribution of the fluctuating density perturbations, we now turn to gyrokinetic simulations, both to check that modelling can reproduce what theory predicts and the experiment has revealed and to seek clearer guidance on the parameter dependence of these effects. These numerical results give us a degree of confidence in the validity of our interpretation of the experimental data, which, especially in what concerns the skewed distributions (Section 11.4), was perhaps not on its own sufficient to build a rock-solid case.

In this chapter, we use a set of local, flux-tube, electrostatic, two-species, ion-scale numerical simulations using the gyrokinetic code GS2[1] that were originally performed for a different, independent study of the transition to turbulence in MAST [40]. The experimental case whose equilibrium parameters served as input for these simulations has previously been used for validation and verification exercises involving both NEMORB [91] and GS2 [105]. This experimental case is labelled EGK and its parameters are given in Table 11.1. While the BES data from this case has been studied extensively using 1D reconstruction of various correlation parameters [91], it unfortunately turns out not to be suitable for a full-scale 2D analysis as developed in Part II, because calculation of k_x and, therefore, the tilt, suffers from insufficient resolution. However, it is not wildly different from our BLM case[2] and, in any event, our aim here is to determine qualitative trends rather than to claim precise agreement between simulations and experiment (although a more limited 1D analysis of the BES data for the EGK case does show respectable agreement with GS2 results [105]).

The obvious advantage accorded by (local flux-tube) simulations is that one can change individual equilibrium parameters at will, while keeping other parameters

[1] http://ter.ps/gs2

[2] It does have a substantially larger flow shear, which was the reason for all the numerical interest in it in the first place, but, in view of the arguments advanced below, the important parameter is not the absolute value of $\hat{\gamma}_E$ by itself but the distance to the stability threshold (see Section 12.3).

Run name	GKa5	GKa4	GKa3	GKa2	GKa1	Marginal
$\hat{\gamma}_E$	0.00	0.08	0.10	0.12	0.14	0.16
Q_i/Q_{gB}	35.1	24.6	18.0	13.0	13.0	1.4
$\delta n/n$	0.073	0.056	0.044	0.040	0.034	0.011
Skewness	-0.055	0.0057	0.097	0.053	0.22	2.3
ℓ_x/ρ_i	4.6	3.8	3.9	3.5	3.8	3.5
ℓ_y/ρ_i	10	8.9	8.7	8.8	8.8	10
$k_x\rho_i$	-0.0057	-0.16	-0.23	-0.22	-0.37	-0.51
$k_y\rho_i$	0.26	0.29	0.29	0.28	0.27	0.24
Tilt Θ/deg	1.5	35	44	44	59	69
τ_{life}	$-$	8.6	9.6	7.9	12	16
CORE						
ℓ_x/ρ_i	3.7	3.3	3.0	3.0	3.3	2.7
ℓ_y/ρ_i	8.9	7.8	7.7	7.8	7.7	9.3
$k_x\rho_i$	0.012	-0.19	-0.25	-0.28	-0.41	-0.56
$k_y\rho_i$	0.27	0.25	0.29	0.29	0.27	0.18
Tilt Θ/deg	-3.2	39	46	50	62	75
TAIL						
ℓ_x/ρ_i	5.1	4.4	4.0	4.1	4.5	3.6
ℓ_y/ρ_i	12	9.8	10	10	9.5	10
$k_x\rho_i$	-0.020	-0.14	-0.14	-0.17	-0.35	-0.50
$k_y\rho_i$	0.28	0.30	0.30	0.29	0.28	0.26
Tilt Θ/deg	5.1	29	30	35	56	67

Table 12.1: Various statistical characteristics of turbulence in a series of simulations corresponding to the equilibrium parameters of the EGK case (Table 11.1, except $a/L_{T_i} = 4.8$ in these runs) and a sequence of values of flow shear $\hat{\gamma}_E$. The Marginal case is the EGK case itself. The rms fluctuation amplitude $\overline{\delta n/n}$ is calculated using (11.8), but replacing $\delta I_i(t)$ with $\delta n_i(t)$; the summation is over all grid points i. Similarly, the skewness is calculated for the fluctuating density field using (11.9). The spatial correlation functions for the GKa5, GKa3, GKa1, and Marginal cases are plotted in Figure 12.1. The fluctuating-density distributions for the GKa5, GKa1, and Marginal runs (the latter two skewed) are shown in Figure 12.5. The conditional correlation functions (CORE and TAIL) are discussed in Section 12.2.2 and plotted in Figures 12.6 (run GKa1) and 12.7 (Marginal run).

constant, and thus look for trends. We will take this route by analysing a sequence of simulations in which the flow shear $\hat{\gamma}_E$ is varied compared to the nominal EGK case—and confirm that the gyrokinetic simulations are able to recover, qualitatively, both the tilted correlation functions (Section 12.1) and the skewed distributions (Section 12.2) observed in the experiment.

However, it must be clear that this does not, in fact, constitute a parameter scan that one might expect to achieve experimentally in a real plasma. Indeed, the sup-

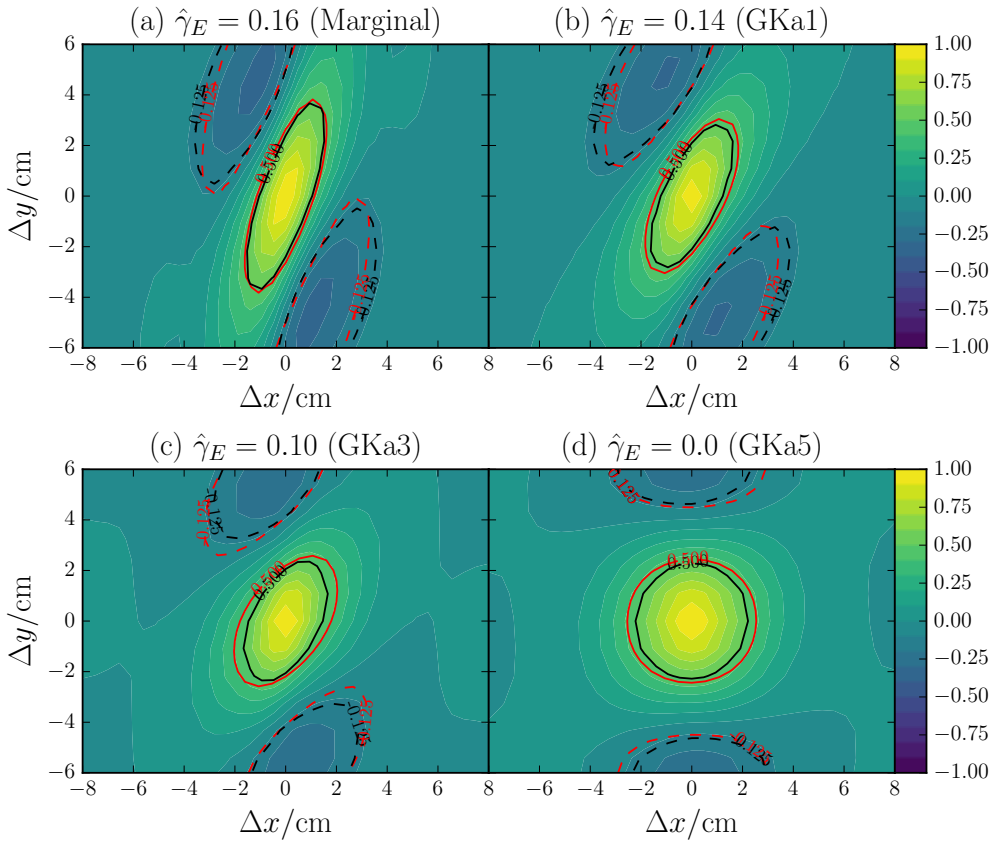
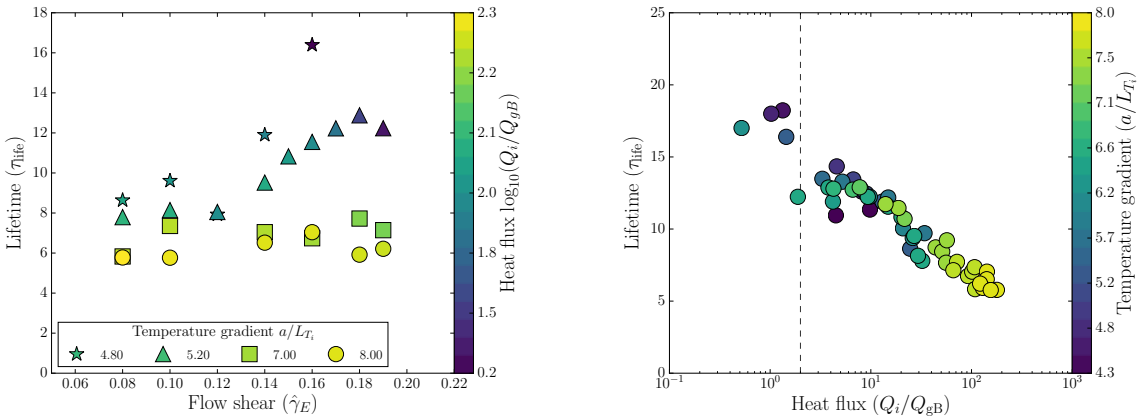


Figure 12.1: Directly calculated spatial correlation functions of the fluctuating density field for 4 of the runs documented in Table 12.1, with, from (a) to (d), value of the flow shear decreasing from the experimental (EGK) value to $\hat{\gamma}_E = 0$. The spatial domain of the simulation is regularly gridded, therefore multiple values of the correlation function (11.3) (with δn_i instead of δI_i, i being the grid point) occur for each $(\Delta r, \Delta Z)$ pair; these values are then averaged as in Section 2.1.4, to produce the spatial correlation function that is plotted (it is also averaged over time, typically several hundred μs, i.e., tens of correlation times). These correlation functions are to be compared with experimental correlation functions with and without flow shear in Figure 11.3. The correlation parameters for the fitting function (11.5), approximating the true correlation functions plotted here, are given in Table 12.1. The red contours in these plots correspond to the fitting function (11.5) with these parameters, showing the quality of the fit (and thus supporting its use for experimental data; see Chapter 2.1 for further discussion).



(a) $\tau_{\rm life}$ vs. $\hat{\gamma}_E$ (b) $\tau_{\rm life}$ vs. $Q_i/Q_{\rm gB}$

Figure 12.2: (a) Life time of perturbations, defined by (11.6), $\tau_{\rm life} = |\tan\Theta/\gamma_E|$, and normalised by $a/v_{{\rm th}i}$, vs. flow shear $\hat{\gamma}_E$ for a number of values of the ion-temperature gradient a/L_{T_i} (distinguished by different shapes of the data points); the data points are coloured according to the value of the gyro-Bohm-normalised heat flux $Q_i/Q_{\rm gB}$ (see discussion in Section 12.3). (b) Same, but here $\tau_{\rm life}$ is plotted vs. $Q_i/Q_{\rm gB}$ with data points coloured according to the value of a/L_{T_i} (this plot includes data from the full set of simulations carried out in [40] and so covers a larger number of values of ITG than (a)); the vertical dashed line indicates the experimental value of $Q_i/Q_{\rm gB}$ for the EGK case (Table 11.1).

pression of the turbulence caused by increasing the flow shear will cause the plasma equilibrium to respond: as the turbulent transport is reduced, assuming constant ion heat flux, the ion-temperature gradient (ITG) must increase [19, 6]. Generally speaking, experimentally one expects to find turbulent plasma states near the stability threshold (which, in the instances of ion-scale MAST turbulence that we are considering is a nonlinear stability threshold, the turbulence being subcritical [40]). As a crude simplification, we can think of this threshold (or "zero-turbulence manifold" [19]) as a boundary in a two-dimensional parameter space consisting of $\hat{\gamma}_E$ and ITG, although obviously other equilibrium parameters are in fact also involved [39, 19, 6, 106]. From the point of view of interpreting experimental results, the key questions are (i) near which part of the zero-turbulence manifold the experimental case under consideration is located and (ii) how close to the threshold it is. The second question is very crucial indeed, because we know from simulations [40] (and will further confirm in what follows) that the properties of our turbulence depend on the distance from threshold very sensitively. To investigate these matters, in Section 12.3, we will consider a set of numerical simulations in a range of values of both flow shear and ITG and argue that both the tilt and the skewness are strong functions of the distance from threshold, i.e., that the symmetry-breaking effects as-

sociated with the flow shear fade away and the symmetry is effectively restored if one probes deep into the strongly turbulent regime far from the stability boundary.

12.1 Tilt vs. flow shear

We start by considering a parameter scan in flow shear, with 6 different values of $\hat{\gamma}_E$ (see Table 12.1) and all other equilibrium parameters the same as those of the EGK experimental case, listed in Table 11.1 (except, in these runs, $a/L_{T_i} = 4.8$, which is within the experimental uncertainty of the measurement [40]). The largest value of the flow shear in this scan, $\hat{\gamma}_E = 0.16$, corresponds to the EGK case itself—and at even larger values, there is no turbulence (all perturbations decay), so we will refer to the simulated EGK case as Marginal.

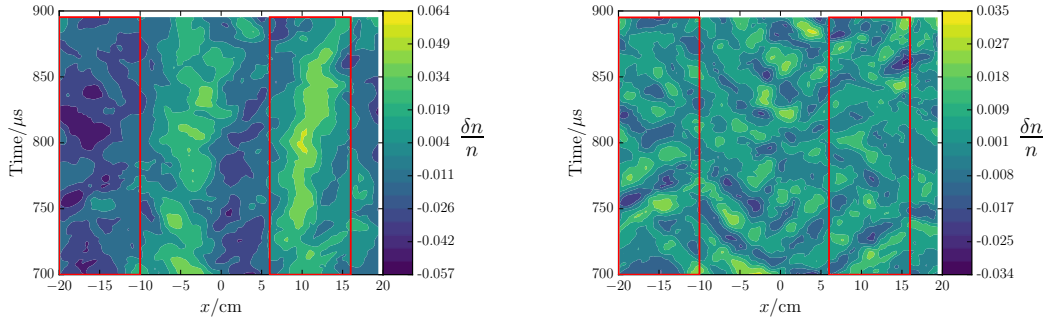
For the purposes of this analysis, we adopt the definition of the fluctuating density field $\delta n_i(t)$ analogous to the definition (11.2) of the fluctuating intensity $\delta I_i(t)$ in the experimental measurements reported in Chapter 11: at each grid point i, it is the density perturbation at this point (extracted directly from the simulations—it is the velocity integral of the perturbed particle distribution function (1.8), which is being solved for by GS2), with a running time average, calculated over a moving 50 μs interval, subtracted, so the time average of the fluctuating field is zero by definition. Note that this corresponds to using a 20 kHz high-pass frequency filter (which experimentally was needed anyway; see Appendix E.1) and that this procedure will remove any long-lived zonal density component (see Section 12.1.2).

The spatial correlation functions of the fluctuating density fields calculated in this fashion are shown in Figure 12.1 and the correlation parameters (lengths and wave numbers) defined by the fitting function (11.5)[3] are documented in Table 12.1. It is manifest that, as the flow shear increases, the radial-reflection symmetry is broken and the correlation function develops a tilt, which becomes quite large as the Marginal case is approached. Qualitatively, the difference between the zero-flow-shear, untilted correlation function for run GKa5 and the sheared, tilted ones for runs GKa3 or GKa1 is very similar to the difference between the DLM and BLM cases shown in Figure 11.3.

12.1.1 Tilt and life time

Quantitatively, we find that the tilt $\tan\Theta = k_x/k_y$ increases approximately linearly with $\hat{\gamma}_E$, except near the stability threshold. Recalling the discussion at the end of Section 10.2 and in Section 11.3.4, we conclude that, except near the stability

[3]The simulations obviously have a much higher spatial resolution than the BES diagnostic, with many more grid points than BES has channels. Therefore, unlike in Section 11.3.2, we do not need to constrain the product $k_Z\ell_Z$ with the aid of the time-correlation function.



(a) without high-pass filter (b) with high-pass filter

Figure 12.3: Perturbed density field from run GKa5 ($\hat{\gamma}_E = 0$) integrated over y shown vs. x and time (a) without subtracting moving time average and (b) with moving time average subtracted (as for all fluctuating density fields used in Chapter 12). The presence of a zonal density component is manifest. The red boxes show regions for which conditional correlation functions shown in Figure 12.4 and discussed in Section 12.1.2 were calculated.

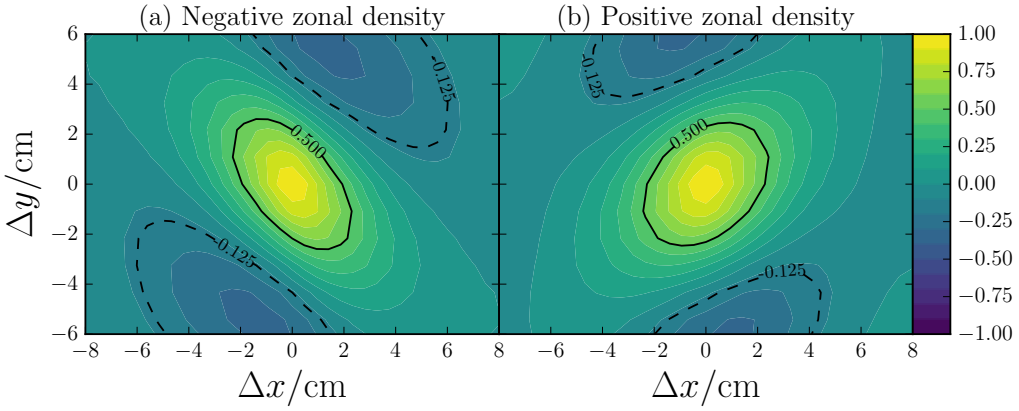


Figure 12.4: Same correlation function as Figure 12.1(d), for run GKa5 ($\hat{\gamma}_E = 0$), but calculated for two spatial subdomains: (a) with negative zonal density and (b) with positive zonal density, as discussed in Section 12.1.2, see Figure 12.3(a).

threshold, the life time (11.6) of the turbulent perturbations is independent of the flow shear—presumably because dynamically the flow shear is not very important away from the threshold. This point is illustrated by Figure 12.2(a). The data for other values of the ion temperature gradient also shown in this figure supports this conclusion and will be further discussed in Section 12.3.1.

12.1.2 Tilts at zero flow shear as a signature of zonal flows

As we saw in Figure 12.1(d), when the mean flow shear is zero, the correlation function of the fluctuating density field is untilted, in agreement with the symmetry (10.1). We stress, however, that this is only true if the correlation function is

calculated over a sufficiently large spatial domain. Because drift-wave turbulence is prone to developing zonal flows [107, 108], locally a flow shear can be present—and indeed is, in the simulations that we are analysing. As these simulations have kinetic electrons, they can, and do, develop a zonal density perturbation on ion scales [109, 110], so the presence of a zonal field is detectable directly from the measured density field, in the form of a y-independent, long-lived component. Because zonal fields have a long life time, compared to the life time of the turbulence, they can only be seen if we remove the high-pass frequency filter effectively imposed on our fluctuating density field by subtracting the running time average (as stated at the beginning of Section 12.1). This is illustrated in Figure 12.3, where we show the y-integrated perturbed density field for the zero-flow-shear run GKa5 with and without this filter.

Experimentally, the high-pass frequency filter may be difficult to abandon (see Appendix E.1), however, the zonal shear can be detected indirectly via correlation functions of the fluctuating density field:[4] if those are calculated over a spatial domain that is smaller (radially) than the wave length of the zonal flow, they will be tilted by the same mechanism as in the case of a mean flow shear. This is illustrated in Figure 12.4, which shows correlation functions for the zero-flow-shear run GKa5 restricted to regions of positive and negative zonal density, as marked in Figure 12.3,—as is obvious from the tilts of the correlation functions, these regions turn out also to be regions of positive and negative zonal shear (in this context, we should perhaps recall the presence of tilted instantaneous structures in the zero-flow-shear DLM case, noted in Section 11.3.1). The overall correlation function in Figure 12.1(d) is an average over several such regions—the opposite tilts average out and the overall radial-reflection symmetry is preserved.

Since turbulence with mean flow shear will also develop zonal flows, a similar analysis applied to it will show a certain spread in the tilt angle of the correlation function depending on whether the zonal shear locally subtracts from or adds to the mean flow shear. This can matter if the mean flow shear is sufficiently weak.

12.2 Skewness vs. flow shear

The numerical scan in flow shear also reveals that the symmetry of the distribution of the fluctuating density field is broken by the flow shear: the skewness of the distribution increases with the flow shear, as documented in Table 12.1; the distributions for a run with no flow shear (for which in accordance with the theoretical expectations outlined in Chapter 10, there is no skew) and runs with two

[4] Since zonal flows advect the fluctuating density field, it is also possible to detect them by tracking the movement of density contours in time [111, 112, 113, 114, 115].

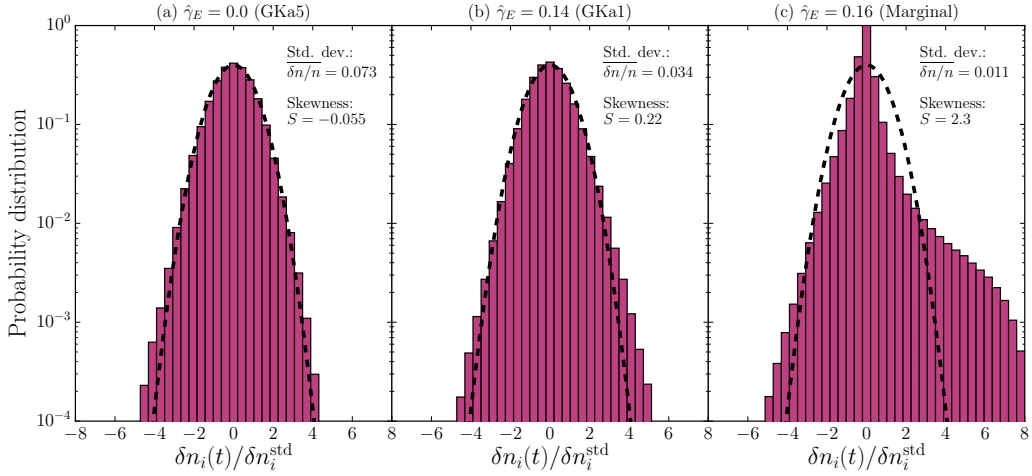


Figure 12.5: Distribution of the fluctuating density field δn, normalised by its own standard deviation, for (a) GKa5 (no flow shear), (b) GKa1 (with flow shear, close but not at the nonlinear stability threshold), (c) Marginal (at the threshold) runs (see Table 12.1). The black-dashed line in each case gives the unit normal distribution. These distributions should be compared with experimental ones with and without flow shear in Figure 11.5.

values of the flow shear, one at the nonlinear stability threshold and one just off it, are shown in in Figure 12.5. The skew in the distribution for the Marginal case in Figure 12.5(c) is extremely pronounced, much more so than anything that we have observed experimentally, but the distribution for the case that is only slightly offset from the stability threshold, shown in Figure 12.5(b), is very similar qualitatively to the experimental BLM case in Figure 11.5(a).[5] Generally speaking, in many runs with various values of $\hat{\gamma}_E$ and a/L_{T_i}, we only find distributions with a pronounced tail on the overdensity side in cases that are very close to the threshold (and in all cases that were simulated, we do find asymmetry in favour of over-, rather than underdensities), while the majority of the skewed distributions are similar to that in Figure 12.5(b). This gives us a degree of confidence that the skewness that we have found in the experimentally measured distributions in Section 11.4 is indeed due to

[5]In Section 11.4, we considered the distribution of the fluctuating intensity field measured by the BES, whilst here we are considering the distribution of the fluctuating density field generated by the gyrokinetic simulations. There is a certain difference between the two, due to the finite-size PSFs of the BES diagnostic [66]. For a closer comparison with experiment, synthetic BES data can be generated from the gyrokinetic simulations by applying the PSFs of the real diagnostic using (2.1). We will not do this here as we are, in any event, not in a position to make a detailed comparison between simulated and BES-measured turbulent density fields in the same experimental configurations, but are rather looking for qualitative trends. The PSF effects on the distribution functions are considered in Appendix E, where we generate synthetic BES data and show that PSFs do not significantly alter the skewness of the distribution.

flow shear. It is likely that the fact that this skewness is not very large (and indeed not always measurable) is due to the rather sensitive dependence of it on the distance to the threshold: note the precipitous decline in skewness from the Marginal run to run GKa1, even though the difference in the values of $\hat{\gamma}_E$ for these two cases ($\hat{\gamma}_E = 0.16$ and 0.14, respectively) is small and experimentally would be within measurement errors on the velocity profile (see further discussion in Section 12.3).

12.2.1 Physics of skewed distributions

Besides encouraging the physical interpretation of the experimental evidence in terms of symmetry breaking associated with flow shear, numerical simulations give us a crucial insight as to how, dynamically, this symmetry breaking occurs. In [40], for which these simulations were originally carried out, it was shown that the transition to turbulence in these flow-sheared MAST configurations occurs via emergence and accumulation (as equilibrium parameters move deeper into the unstable regime) of long-lived, intense coherent structures, which occupy a small fraction of the volume. This is because turbulence in these equilibria is subcritical—while the system is formally linearly stable, perturbations do grow transiently and, for finite perturbations, this can lead to non-zero nonlinearly saturated turbulent fluctuation levels and heat fluxes. Since finite amplitudes are required for such a state to persist, the only way for the system to have small overall heat fluxes as the threshold is approached is by restricting finite amplitudes to a small fraction of the volume, hence the spatially sparse, but intense structures. Clearly, in terms of the probability distribution of the amplitudes, the presence of such structures and the fact that they give rise to a non-zero overall heat flux, implies skewed distributions. Away from the threshold, the structures become more numerous, overlap, interact, break up and dissolve into a more volume-filling turbulent sea of "eddies," characteristic of standard, unsheared drift-wave turbulence—resulting in approximately symmetric distributions.

Another important observation afforded us by the numerical simulations but unavailable experimentally (because equilibrium parameters in experiments cannot in general be changed independently) is that, other things being equal, increasing flow shear does have a suppressing effect on the rms amplitude of the turbulent density field: this is documented by the $\overline{\delta n/n}$ values in Table 12.1 (it is not evident in Figure 12.5, because these are distributions of δn normalised to its own standard deviation). Thus, as we anticipated in Section 11.4.2, the tail of the skewed distributions found for the near-threshold, sheared turbulence is, in a sense, a remnant of a wider unsheared/far-from-threshold distribution, containing large-amplitude perturbations that might have existed in a more unstable local equilibrium config-

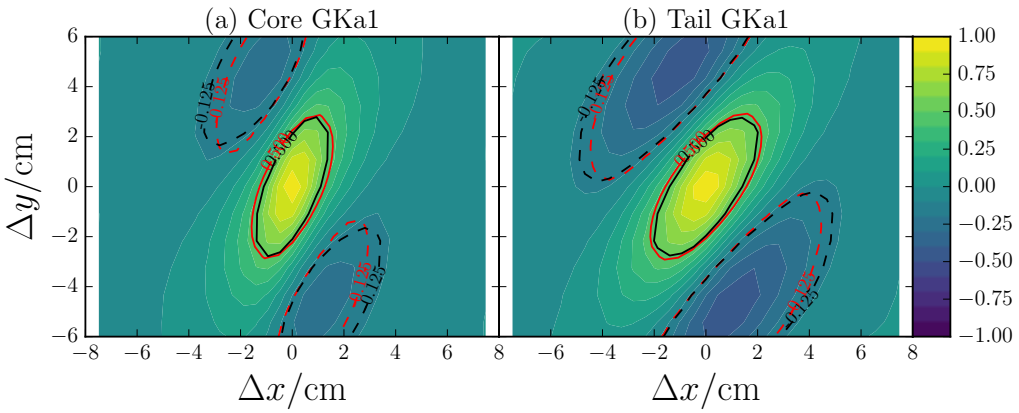


Figure 12.6: Same correlation function as Figure 12.1(b), for run GKa1, but this time conditioned on (a) lower densities (core of the distribution, $|\delta n| < 2.75$ standard deviations) and (b) higher densities (tail of the distribution, $\max \delta n > 3$ standard deviations) in the way described in Section 12.2.2. The correlation parameters for each case are given in Table 12.1. These correlation functions can be compared to Figure 11.7 for the experimental BLM case.

uration (although, as argued above, these perturbations have a rather distinct character once only a dwindling number of them are left with a sole responsibility of maintaining turbulent transport; see also Section 12.2.2).

12.2.2 Skewness vs. tilt: two-component turbulence in simulations

In Section 11.4.2, we conjectured that turbulence in the presence of flow shear is a two-component mix of strong but rare perturbations giving rise to the skew in the distribution and a wider sea of weaker ones, which constitute the core of the distribution and are tilted, more or less passively, by the flow shear. In other words, the tilt and the skew represent symmetry breaking by flow shear occurring in different types of perturbations.

To test this picture, we introduced conditional correlation functions, designed to measure the spatial correlation parameters associated with the core and the tail of the distribution. Here we perform the same analysis on the numerically simulated fluctuating density fields, with the same condition that frames containing at least one instance of δn larger than 3 standard deviations are declared to belong to the tail (for the purposes of this selection, the full artificially large $40\ \mathrm{cm} \times 80\ \mathrm{cm}$ GS2 computational domain is split into $7.48\ \mathrm{cm} \times 9.19\ \mathrm{cm}$ subdomains—this is comparable to the $10\ \mathrm{cm} \times 8\ \mathrm{cm}$ BES subarray that we used in Section 11.4.2 and necessary in order for conditioning on the maximum value of δn within a subdomain to pick out statistically different patches of turbulence). The results are documented in Ta-

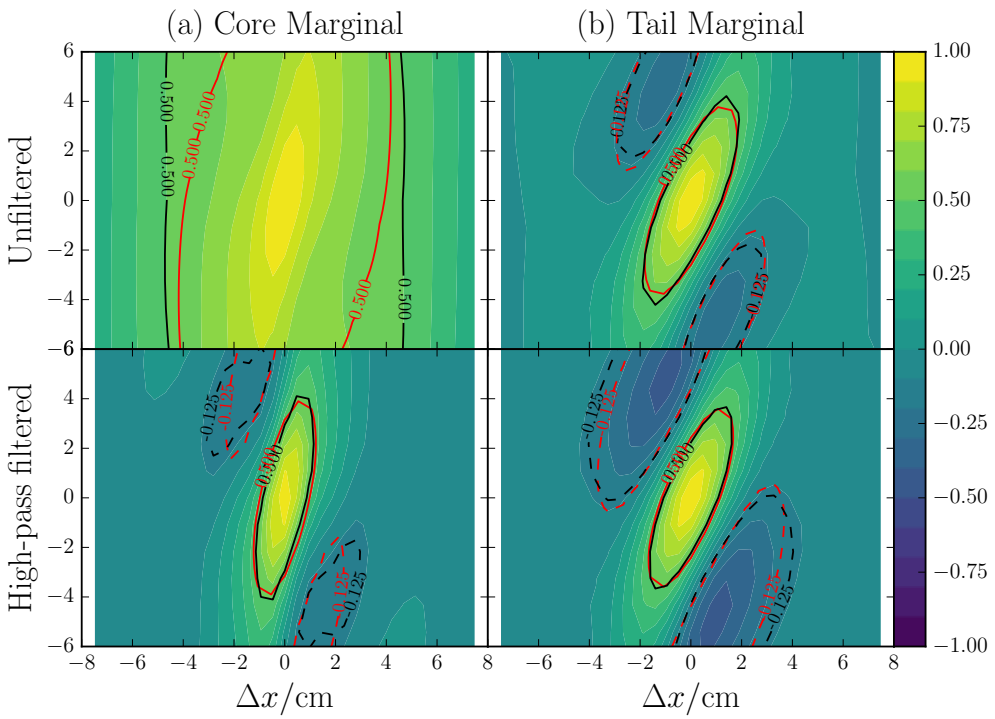


Figure 12.7: Same as Figure 12.6, but for the Marginal run (see Table 12.1 and Figure 12.1(a)). The bottom row has correlation functions calculated in the standard way from the high-pass-filtered fluctuating density field (as explained at the beginning of Section 12.1); the top row has correlation functions of an unfiltered field, i.e., including the zonal density perturbation. The latter manifestly dominates the core population but not the tail.

ble 12.1 and conditional correlation functions for the core and tail of two of the runs with flow shear are shown in Figures 12.6 (run GKa1) and 12.7 (Marginal run). We see that fluctuations in the tail of the distribution are always less tilted than those in the core. This is similar to the behaviour exhibited by the experimental BLM case in Section 11.4.2.

Another qualitative similarity between simulated and real sheared turbulence is that the perturbations in the tail of the distribution, in both cases, have longer radial correlation lengths ℓ_x, not just lower tilt (i.e., smaller k_x). Table 11.3 shows this for both BLM and IFS cases (even despite the failure of the latter to follow the trend as far as its tilt angle is concerned) and Table 12.1 confirms the same trend for our numerical runs with varying flow shear; it is also quite obvious from the plots of the conditional correlation functions in Figures 12.6 and 12.7.

Comparing these two figures, we note also a sizeable increase of the poloidal correlation length in the core of the distribution as the threshold is approached (see Table 12.1). Interestingly, in the Marginal run, the core fluctuations are so weak, that

Run name	Marginal	GKb1	GKb2	GKb3	GKb4	GKb5	GKb6	GKb7
a/L_{T_i}	4.8	4.9	5.0	5.1	5.2	6.0	7.0	8.0
Q_i/Q_{gB}	1.4	5.2	7.9	9.8	14.8	44.0	92.3	142.2
$\delta n/n$	0.011	0.021	0.027	0.030	0.035	0.069	0.11	0.14
Skewness	2.3	0.50	0.40	0.28	0.24	0.075	0.094	0.12
ℓ_x/ρ_i	3.5	3.1	3.2	3.2	3.3	3.7	3.6	3.6
ℓ_y/ρ_i	10	10	9.9	9.4	9.3	8.6	9.3	9.3
$k_x\rho_i$	-0.51	-0.44	-0.43	-0.42	-0.41	-0.34	-0.24	-0.24
$k_y\rho_i$	0.24	0.25	0.25	0.26	0.27	0.29	0.27	0.26
Tilt Θ/deg	69	65	64	63	62	54	47	48
τ_{life}	16	13	13	12	12	8.7	6.7	7.0
CORE								
ℓ_x/ρ_i	2.7	2.6	2.7	2.7	2.8	3.2	3.1	3.2
ℓ_y/ρ_i	9.3	8.8	8.6	8.2	7.9	7.4	7.5	7.4
$k_x\rho_i$	-0.56	-0.49	-0.48	-0.47	-0.46	-0.38	-0.29	-0.31
$k_y\rho_i$	0.18	0.25	0.25	0.26	0.27	0.29	0.27	0.26
Tilt Θ/deg	75	67	66	66	64	53	52	55
TAIL								
ℓ_x/ρ_i	3.6	3.7	3.9	4.0	3.9	4.4	4.2	4.1
ℓ_y/ρ_i	10	10	9.8	9.8	9.9	8.9	9.7	9.9
$k_x\rho_i$	-0.50	-0.42	-0.40	-0.38	-0.38	-0.30	-0.19	-0.17
$k_y\rho_i$	0.26	0.27	0.26	0.27	0.28	0.30	0.28	0.28
Tilt Θ/deg	67	62	62	60	58	51	40	36

Table 12.2: Same as Table 12.1, but for $\hat{\gamma}_E = 0.16$ and a sequence of values of the ion-temperature gradient a/L_{T_i}.

the zonal density perturbation (in our definition of the fluctuating density field, it is removed by time averaging/high-pass frequency filtering; see Section 12.1.2) becomes comparable to them—so much so that, as we see in Figure 12.7, it dominates the conditional core correlation function (although not the total one or the tail) if the high-pass frequency filter is removed (suggesting what is perhaps a promising experimental direction of enquiry).

12.3 Restoration of symmetry far from threshold

In our discussion of both experimental and numerical results so far, we have repeatedly anticipated the argument that what truly matters for the degree to which the symmetry of the turbulence is broken is how far from the (nonlinear) stability threshold the system is. Thus, changing the flow shear in Sections 12.1 and 12.2 led to significant changes in behaviour because this took the system closer to or farther from the Marginal case.

This notion is easily confirmed if we fix the flow shear at what in the previous sections was the marginal value, $\hat{\gamma}_E = 0.16$, and change instead the ion-temperature gradient (ITG) a/L_{T_i}. A sequence of runs within such a parameter scan is documented in Table 12.2. The trend that emerges is very clear: as the ITG is increased from the marginal value ($a/L_{T_i} = 4.8$), both the tilt angle of the correlation function and the skewness of the distribution of the fluctuating densities diminish (the decline in skewness is particularly strong). Thus, the symmetry is broken less strongly.[6] The situation in this sense is rather similar to what happened in the $\hat{\gamma}_E$ scan (Table 12.1) with decreasing flow shear. One might argue that, as turbulence becomes stronger away from the threshold (with the distance from the threshold measured either in $\hat{\gamma}_E$ or in a/L_{T_i}), the flow shear ceases to be an important factor and the symmetry formally broken by it is effectively restored.

12.3.1 Tilt, flow shear and life time

It is worth discussing a little further how the effective restoration of symmetry happens for the tilt of the correlation functions. We argued at the end of Section 10.2 and again in Section 12.1.1 that the flow shear did not need to be dynamically important in order to induce a tilt in the correlation function. In such a "passive" tilting scenario, the tilt $\tan\Theta = k_x/k_y$ is simply proportional to γ_E, with the constant of proportionality being the life time τ_{life} of the perturbations, as per (10.8) or (11.6). This life time, defined by (11.6) and given in Table 12.2, becomes shorter as the ITG is increased. This is also manifest in Figures 12.2(a) and (b)—the latter figure is a scatter plot of τ_{life} for a large set of values of $\hat{\gamma}_E$ and a/L_{T_i} against the gyro-Bohm-normalised ion heat flux Q_i/Q_{gB}, where Q_i is calculated using (1.10) and $Q_{\text{gB}} = n_i T_i v_{\text{th}i} \rho_i^2/a^2$, which is a good measure of distance to threshold (it is zero at the threshold and increases steeply away from it [40]). The reason correlation times shorten is that larger ITG implies stronger drive and so higher turbulent amplitudes: "eddies" turn over faster.[7] Shorter τ_{life} then implies smaller tilt angle ($\tan\Theta \sim \gamma_E \tau_{\text{life}}$) farther from marginality.

In physical terms, the flow shear ceases to be important if it is smaller than the local, fluctuating velocity shear acting on a turbulent perturbation and caused by its fellow perturbations. This nonlinear fluctuating shear must, in saturation, be

[6] Technically, the symmetry is either broken or it is not. However, we resort to the colloquial phrasing referring to the 'strength' of the symmetry breaking as a synonym for the size of the characteristics (tilt and skewness) that indicate the symmetry has been broken.

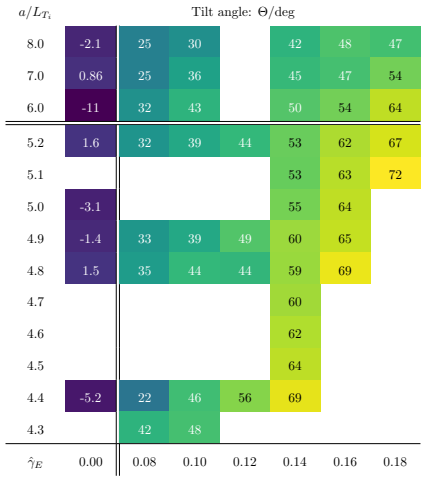
[7] Very far from the threshold, in ITG turbulence without flow shear (which, far from the threshold, presumably does not matter anyway), the correlation times become independent of the ITG because turbulence is controlled by the "critical balance" between linear, nonlinear and streaming time scales [27], but here we are discussing cases that are still relatively close to the threshold (although one might argue that $a/L_{T_i} = 7$ and 8 in Figure 12.2(a) already have fairly similar values of τ_{life}).

comparable to some appropriate linear rate at which the perturbations are replenished by the ITG drive. In this sense, the competition between the life time of the turbulence and the flow shear as the threshold is approached is reminiscent of the so-called Waltz rule [46]: that in order to affect (suppress) the turbulence, the flow shear must be similar to, or greater than, the linear growth rate (we recall, however, that the turbulence that we are dealing with here is subcritical [40] and so formally there is no linear growth rate; what effective quantity from the linear theory should be used instead is a matter of current research interest [18, 19, 105]).

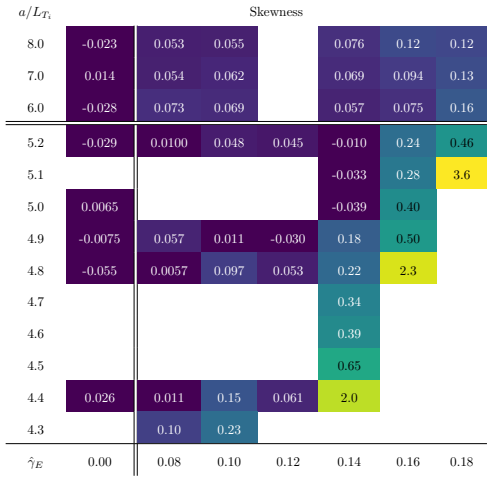
12.3.2 Tilt and skewness vs. distance from threshold

Figures 12.8(a) and (b) show the tilt angle of the correlation function and skewness of the distribution of the fluctuating density field for a range of values of the flow shear $\hat{\gamma}_E$ and ITG a/L_{T_i} around the nonlinear stability threshold and departing from it—this extends the $\hat{\gamma}_E$ and a/L_{T_i} scans documented in Tables 12.1 and 12.2. The conclusion remains the same: away from the threshold, symmetry is effectively restored—particularly quickly for the distribution functions (as we argued in Section 12.2.1, the restoration of symmetry of the distribution of fluctuating densities far from the threshold occurs because intense coherent structures that dominate the transition to turbulence and are responsible for the skewed distributions become too numerous for individual survival, interact and break each other apart [40]).

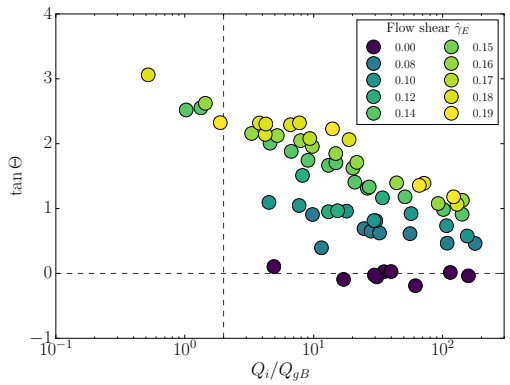
As we already did in Section 12.3.1 for the life time of the perturbations, we quantify the dependence of the measures of asymmetry (tilt and skewness) on the distance to threshold in terms of their dependence on the gyro-Bohm-normalised heat flux Q_i/Q_{gB}, which vanishes at the threshold but increases strongly and monotonically away from it [40] and thus constitutes a good order parameter. Scatter plots of the tilt and the skewness vs. Q_i/Q_{gB} are shown in Figures 12.8(c) and (d), respectively, for the entire data base of numerical simulations originally carried out in [40]. We see that, modulo some scatter, both the tilt and the skewness are approximately functions of the distance to the threshold (to be precise, Figure 12.2(b) suggests that it is the life time $\tau_{\mathrm{life}} = \tan\Theta/\gamma_E$, rather than the tilt, that is a nearly single-valued function of this distance, at least when measured sufficiently far from the threshold). The case of $\hat{\gamma}_E = 0$ is the exception to this rule, as expected theoretically, being subject to the exact symmetry (10.1): namely, at zero flow shear, both the tilt and the skew are essentially zero regardless of how marginal, or otherwise, the system is.



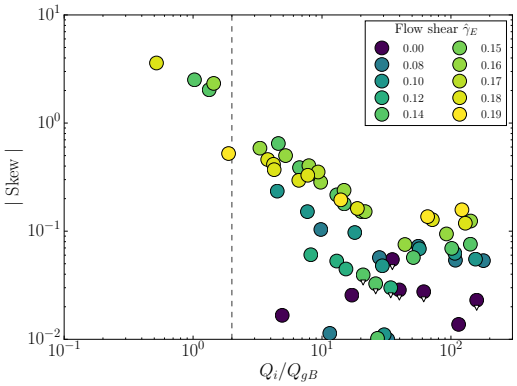
(a) Tilt vs. $\hat{\gamma}_E$ and a/L_{T_i}



(b) Skewness vs. $\hat{\gamma}_E$ and a/L_{T_i}



(c) Tilt vs. Q_i/Q_{gB}



(d) Skewness vs. Q_i/Q_{gB}

Figure 12.8: (a) Tilt angle of the correlation function and (b) skewness of the distribution of the fluctuating density field vs. flow shear $\hat{\gamma}_E$ and ITG a/L_{T_i} in a range of values of these parameters around the nonlinear stability threshold. The tilt and the skewness are replotted in (c) and (d), respectively, vs. the gyro-Bohm-normalised ion heat flux, with data points coloured according to the value of $\hat{\gamma}_E$. These plots contain data for $\hat{\gamma}_E \in [0, 0.19]$ and ITG $a/L_{T_i} \in [4.3, 8]$, covering the entire database of the runs carried out in [40]. In (d), inverted triangles mark the cases where skewness is negative.

CHAPTER 13

Discussion

To summarise, we started with a premise that, as the presence of the flow shear appears to be quite strongly correlated with larger temperature gradients both in MAST [6] and in numerical simulations [19, 40], the effect of the shear on the local structure of plasma turbulence must be detectable. Theoretically, we argued (in Chapter 10) that flow shear would break the reflection symmetry (10.1) [98, 99] and that statistically this symmetry breaking would be actualised in the form of skewed distributions (Section 10.1) and tilted correlation functions (Section 10.2) of the fluctuating density field. We did then find both of these signatures of symmetry breaking experimentally (Sections 11.4.1 and 11.3.3, respectively), at least as a proof of principle—in specific examples of turbulent density fields in MAST with and without flow shear.

For a number of reasons to do with spatial resolution of the MAST BES system and with the range of equilibrium parameters available, we cannot, at this point, have a broad parameter-scan study and so we sought reassurance, validation and further physical insight from a set of numerical simulations of MAST turbulence performed by [40] and covering a range of flow shears and ion-temperature gradients in a MAST-relevant equilibrium configuration. Again we found both skewed fluctuating-density distributions (Section 12.2) and tilted correlation functions (Section 12.1), qualitatively similar to the experimental ones.

With the aid of the simulations, we were able to establish that, generally speaking, the symmetry breaking was most pronounced in the vicinity of the (nonlinear) stability threshold, whereas away from it, symmetry was gradually restored (Section 12.3.2)—essentially because flow shear became dynamically less and less relevant far from the threshold (Section 12.3.1). The dependence of the symmetry breaking on the distance from threshold—especially of the skewness of the fluctuating-density distributions—turned out to be quite strong. Experimentally, while we expect to find turbulent states in the general vicinity of the stability boundary (as indeed confirmed in [40]), it is not reasonable to expect them to be exactly on it. The degree to which symmetry is found to be broken can then be viewed as an indicator of how close to the threshold any given measured instance of turbulence is.

We have also argued that tilted correlation functions provide a versatile diag-

nostic that could be used to probe the effective life time (correlation time) of turbulent structures (Sections 11.3.4, 12.1.1, and 12.3.1) and the local zonal shear (Section 12.1.2). Furthermore, when conditioned on the amplitude of the fluctuating density, these correlation functions appeared to reveal, both experimentally (Section 11.4.2) and numerically (Section 12.2.2), that sheared, skewed, near-threshold turbulence could be thought of as consisting of two components: longer-lived, spatially larger, more intense, but statistically rarer structures and a general sea of smaller, weaker, but statistically volume-filling fluctuations. Indeed, that spatially sparse coherent structures dominate the transition to turbulence in the physical situation considered here was shown by [40] (see the summary of their argument in Section 12.2.1)—what we have found here is that the statistical signature of these structures is the breaking of symmetry (skewness) of the distribution function of the fluctuating density, or, conversely, that the physical way in which the system takes advantage of the breaking of symmetry is the emergence of these structures. The tilting of the correlation functions is a better understood and, arguably, more straightforward phenomenon (Section 10.2) affecting both strong and weak perturbations, the latter more than the former (see Sections 11.4.2 and 12.2.2).

Part IV

Conclusions

Chapter 14

Conclusions and future work

In this Thesis, we have presented, in Part II, a full discussion of how the point-spread functions (PSFs) of the Beam-Emission-Spectroscopy (BES) diagnostic on MAST modify the correlation function of the turbulent density field, and the corresponding fluctuation amplitude, correlation lengths, wavenumbers, and correlation times. The main results of Part II can be separated into two parts: the first is the elucidation of the assumptions behind the measurement methods used to extract statistical quantities from time series of turbulence data (most notably the correlation-time measurement, see Chapter 8), while the second is the development of a method for the reconstruction of the fluctuation amplitude and spatial correlation parameters of a turbulent density field from BES measurements (Chapter 7). Thus, given a two-point correlation function of the BES-measured intensity field, we have provided an algorithm for extracting the corresponding correlation function for the true density field.

In Part III of this thesis, we have used the results from Part II to help us understand how flow shear affects the statistical properties of the measured ion-scale turbulence in MAST (Chapter 11). We have identified that flow shear tilts the spatial correlation function of the turbulent density field, as well as causing the distribution of fluctuations to become skewed. This has been interpreted in the context of flow shear breaking the symmetry of the gyrokinetic equation, see (10.1). In Chapter 12, by performing a similar analysis on the turbulent density field from nonlinear gyrokinetic simulations of a MAST plasma, the same effects of flow shear on the structure of the turbulence as were seen in experiment have been reproduced. Furthermore, the gyrokinetic simulations have provided insight into how the magnitude of the tilt and skewness increases as the distance to the marginal stability boundary decreases, due to competition between the equilibrium flow shear and the turbulent velocity field.

It is quite clear that, experimentally, a much more extensive study is called for. The trends revealed by the numerical simulations serve as a guideline to the range of questions that can be asked and of parameter dependences that could be verified or falsified. It would be interesting to learn in what circumstances fluctuating-density distributions are skewed towards underdensities, rather than overdensities (exem-

plified by one of the experimental cases; see Section 11.4.1). The nature and role of zonal flows generally and in subcritical turbulence with flow shear in particular (such as the MAST turbulence that we have investigated), remain a fascinating subject, which perhaps could be tackled experimentally using some of the tools developed here (see Section 12.1.2) or other methods [115]. More generally, a full experimental (as well as numerical and theoretical) understanding of the transition to turbulence and of the resulting turbulent states in subcritically unstable, sheared tokamak turbulence is a worthwhile goal, important for practical purposes of optimising tokamaks and perhaps learning how to manipulate stability boundaries.

Additional theoretical work is also required. First, there is the outstanding question of what determines the distance, in flow-shear and ion-temperature-gradient parameter space, from the marginal boundary at which any specific experimentally realisable equilibrium will be. Or, rather, if we consider the equilibrium flow shear to be a control parameter, then we can ask: what determines the temperature gradient of the resulting equilibrium? Such a theory has been constructed in the absence of flow shear using the critical balance conjecture [27], however, further numerical (and experimental) investigation is required to pin down which physical mechanism is most important once flow shear is introduced. Secondly, there is the obvious question of how the tilt and skewness depend on other equilibrium parameters (see Table 11.1 for a full list), or, more pertinently, how the shape and position of the stability boundary varies in the full parameter space.

Finally, the 'complete' nature of the simulations allows for further investigation into parameters that are not directly accessible to experimental diagnostics. For example, the phase relationship between the fluctuating density and electrostatic potential fields can be calculated, which could provide insight into how, as one approaches the stability boundary, the growth rates of instabilities change [10, 18] and how transport rates become suppressed.

Part V

Appendices

APPENDIX A

Measuring the product of the poloidal wavenumber and poloidal correlation length

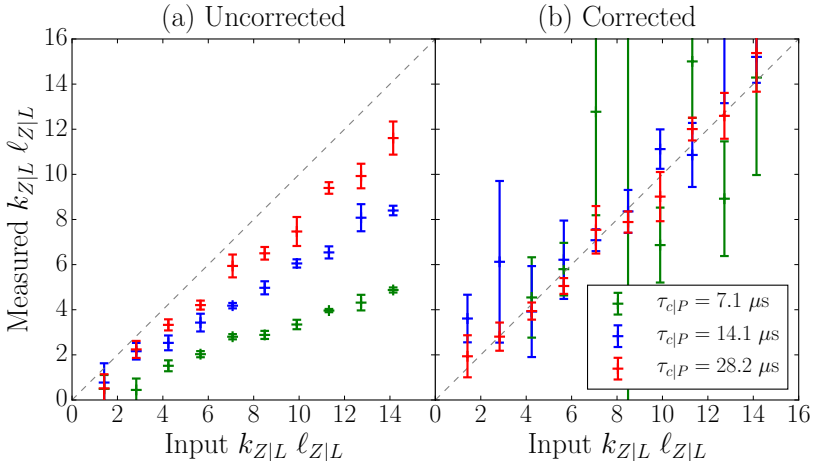


Figure A.1: A scan in $k_{Z|L}\ell_{Z|L}$ has been performed using our model of fluctuating fields (see Section 6.1) by varying $k_{Z|L}$ and keeping constant $\ell_{Z|L} = 16.3$ cm, for three different values of correlation time $\tau_{c|L} \in \{7.1, 14.1, 28.2\}$ μs. In both panels (a) and (b), the measurement of $k_{Z|L}\ell_{Z|L}$ is made by fitting (2.12) to the auto-correlation function (2.4) of the numerically generated fluctuating density field. In (b), the fit is performed after correcting the auto-correlation function for its temporal decay $\tau_{c|L}$, by multiplying it by $\exp(\Delta t^2/\tau_{c|L}^2)$.

The temporal auto-correlation function in the laboratory frame (3.7) contains both spatial and temporal correlation parameters. In this Appendix, we demonstrate that it is possible to extract the product of the poloidal wavenumber $k_{Z|L}$ and poloidal correlation length $\ell_{Z|L}$ from the temporal auto-correlation function (3.7), provided that the correlation time $\tau_{c|L}$ has been measured (using, for example, the CCTD method — see Section 2.1.2).

The product $k_{Z|L}\ell_{Z|L}$ plotted in Figure A.1(a) is measured by fitting (2.12) to the temporal auto-correlation function calculated using (2.4), with the intensity field δI replaced by a density field δn generated numerically using our model of fluctuating fields (see Section 6.1 and Appendix B). Figure A.1(a) shows that a finite value of the correlation time causes the measured product $k_{Z|L}\ell_{Z|L}$ to be an underestimate of

the true $k_{Z|L}\ell_{Z|L}$ (input into the model).

The degree to which $k_{Z|L}\ell_{Z|L}$ is underestimated increases as the correlation time becomes shorter. This is because the contribution of the correlation time $\tau_{c|L}$ to the auto-correlation time (3.8) becomes large compared to the ratio of the poloidal correlation length to the toroidal velocity, $\ell_{Z|L}/v_\zeta$, which is held constant for this analysis. The comparison between $\tau_{c|L}$ and $\ell_{Z|L}/v_\zeta$ can be understood by inspecting (3.8), using (3.4) to relate the plasma-frame correlation parameters to the laboratory-frame correlation parameters, setting the poloidal velocity $v_Z = 0$, and assuming that the parallel correlation length $\ell_{z|P} \gg \ell_{Z|L}$.

In Figure A.1(b), we show that the underestimate of $k_{Z|L}\ell_{Z|L}$ can be corrected for, as discussed in Section 2.1.4, by multiplying the measured auto-correlation function by $\exp(\Delta t^2/\tau_{c|L}^2)$, before fitting (2.12). The quality of the reconstructed value of $k_{Z|L}\ell_{Z|L}$ clearly decreases as the correlation time becomes shorter. This is because any small errors in the measurement of either the temporal auto-correlation function or the correlation time will be increased by using the correction factor $\exp(\Delta t^2/\tau_{c|L}^2)$, which grows faster in Δt for smaller $\tau_{c|L}$.

We have not considered PSF effects in this Appendix, because we could perform the exact same analysis to extract the product $k_{Z|B}\ell_{Z|B}$ of the intensity field, provided we have a measurement of the correlation time of the intensity field $\tau_{c|B}$. This is possible because the technique does not depend on how the correlation function decays in time (see discussion in Section 8.2), but rather just that we are able to correct for that effect (i.e., all the information about the temporal decay is contained in $\tau_{c|B}$).

Finally, we estimate whether this procedure is able to reconstruct accurately the product $k_{Z|B}\ell_{Z|B}$ from experimental data obtained using the MAST BES. As discussed above, and from (3.8), we require that

$$\tau_{c|L} \gg \frac{\ell_{Z|L}}{v_\zeta}, \tag{A.1}$$

in order for us to have confidence in the resulting value of $k_{Z|L}\ell_{Z|L}$. We can translate (A.1) into BES-relevant quantities by changing $\tau_{c|L} \to \tau_{c|B}$ and $\ell_{Z|L} \to \ell_{Z|B}$. In MAST, $\tau_{c|B} \simeq 10\ \mu$s, $\ell_{Z|B} \lesssim 10$ cm, and $v_\zeta \gtrsim 2$ cm/μs. These values satisfy (A.1) and, therefore, we should be able to use this procedure to measure $k_{Z|B}\ell_{Z|B}$ with reasonable accuracy for real MAST BES data.

APPENDIX B

Modelling a fluctuating field

In this Appendix, we provide the detailed description of the model of fluctuating fields introduced in Section 6.1, extended in Section 8.2 and used by us to test our data reconstruction methodology. First, in Appendix B.1, we describe the equations used to generate the two-dimensional fluctuating field. In Appendix B.2, the plasma-frame correlation function of this fluctuating field is calculated, followed by the laboratory-frame correlation function in Appendix B.3. In Appendix B.4, the fluctuation amplitude of this model is discussed. Then, in Appendix B.5, details of the algorithm for generating the described fluctuating field are presented. In Appendix B.6, the input parameters are provided for the model fluctuating fields used in this thesis.

B.1 Basic equations

We generate a fluctuating field in the radial-poloidal plane as a function of time:

$$\frac{\delta n}{n}(r, Z, t) = \sum_{i=1}^{N} s_i(r, Z, \zeta = 0, t, r_{i0}, Z_{i0}, \zeta_{i0}, t_{i0}), \tag{B.1}$$

where N is the number of 'individual perturbations' s_i, which are functions of the laboratory-frame coordinates: the radial r, poloidal Z, and toroidal ζ positions and the time t, as well as the initial position of the perturbation $(r_{i0}, Z_{i0}, \zeta_{i0}, t_{i0})$ in space and time. From here on, we suppress the dependence of s_i on the initial position. The toroidal coordinate of the radial-poloidal plane at which the fluctuating field is generated is specified to be $\zeta = 0$.

The structure of each individual perturbation is specified in the plasma frame (Section 3.1). The plasma frame is defined in terms of field-aligned coordinates (x radial, z parallel to the magnetic field, y binormal). In this Appendix, we define the transformations that take us from the plasma frame into the laboratory frame (Section 3.2), so that an individual perturbation

$$s_i(x, y, z, t) = A_i \exp\left\{ -\frac{[\Delta x_i(t)]^2}{\lambda_x^2} - \frac{[\Delta y_i(t)]^2}{\lambda_y^2} - \frac{[\Delta z_i(t)]^2}{\lambda_\parallel^2} - \frac{[\Delta t_i(t)]^2}{\tau_c^2} \right\} \times \cos[k_x(t)\Delta x_i(t) + k_y \Delta y_i(t) + \phi_i], \tag{B.2}$$

can be written in terms of the laboratory-frame coordinates, and, therefore, making it possible to evaluate (B.1). In (B.2), A_i is the amplitude of the perturbation taken from a Gaussian random distribution with zero mean and standard deviation σ_{amp}, λ_x is the characteristic radial length, λ_y is the characteristic binormal length, $\lambda_\parallel$ is the characteristic parallel length, τ_c is the characteristic lifetime, $k_x(t)$ is the radial wavenumber, k_y is the binormal wavenumber, ϕ_i is a random phase uniformly distributed in the range $[0, 2\pi]$. Note that the term 'characteristic' is used because, as we will find, these differ non-trivially from the correlation lengths and times that are measured in the laboratory frame.

If the position of the centre (maximum) of the ith perturbation is $(x_i(t), y_i(t), z_i(t))$, then, in (B.2),

$$\Delta x_i(t) = x - x_i(t), \quad \Delta y_i(t) = y - y_i(t), \quad \Delta z_i(t) = z - z_i(t). \tag{B.3}$$

The relative plasma-frame coordinates (B.3) are related to the laboratory-frame coordinates (r, Z, ζ) via

$$\begin{aligned} \Delta x_i(t) &= \Delta r_i(t), \\ \Delta y_i(t) &= \Delta\zeta_i(t)\sin\alpha + \Delta Z_i(t)\cos\alpha, \\ \Delta z_i(t) &= \Delta\zeta_i(t)\cos\alpha - \Delta Z_i(t)\sin\alpha, \end{aligned} \tag{B.4}$$

where α is the field-line pitch angle and

$$\Delta r_i(t) = r - r_i(t), \quad \Delta Z_i(t) = Z - Z_i(t), \quad \Delta\zeta_i(t) = \zeta - \zeta_i(t). \tag{B.5}$$

The centre of the perturbation $(r_i(t), Z_i(t), \zeta_i(t))$ is related to $(x_i(t), y_i(t), z_i(t))$ by expressions analogous to (B.4).

The time evolution of each individual perturbation is determined by five effects:

1. the growth and decay of the perturbation controlled by the characteristic lifetime, τ_c:

$$\Delta t_i = t - \left(t_{i0} + \frac{1}{2}C\tau_c\right), \tag{B.6}$$

   where t_{i0} is the time at which the perturbation is created and C is a dimensionless constant that describes how long a perturbation exists: time $C\tau_c/2$ passes before it reaches its peak amplitude;

2. the advection of the perturbation in the toroidal direction by the toroidal flow v_ζ, so the toroidal position of the centre of the perturbation evolves as

$$\zeta_i(t) = \zeta_{i0} + v_\zeta \Delta t_i, \tag{B.7}$$

   where ζ_{i0} is the initial toroidal position of the perturbation;

3. the advection of the perturbation in the poloidal direction by a (small) poloidal

flow v_Z, so the poloidal position evolves as

$$Z_i(t) = Z_{i0} + v_Z \Delta t_i, \tag{B.8}$$

where Z_{i0} is the initial poloidal position of the perturbation;

4. the advection of the perturbation in the radial direction by a (fluctuating) radial flow v_r, so that the radial position evolves as

$$r_i(t) = r_{i0} + v_r \Delta t_i, \tag{B.9}$$

where r_{i0} is the initial radial position of the perturbation;

5. the increase in $k_x(t)$ caused by the radial gradient of the toroidal velocity S (the flow shear), see discussion in Section 10.2:

$$k_x(t) = k_y S \Delta t_i + k_{x0}, \tag{B.10}$$

where k_{x0} is the radial wavenumber of the perturbation (whose meaning is discussed below).

Summarising the above expressions, we can write the time and spatial dependence in (B.2) explicitly as

$$\Delta t_i = t - \left(t_{i0} + \frac{1}{2} C \tau_c \right), \tag{B.11}$$

$$\Delta x_i = r - r_{i0} - v_r \Delta t_i, \tag{B.12}$$

$$\Delta y_i(t) = (\zeta - \zeta_{i0} - v_\zeta \Delta t_i) \sin\alpha + (Z - Z_{i0} - v_Z \Delta t_i) \cos\alpha, \tag{B.13}$$

$$\Delta z_i(t) = (\zeta - \zeta_{i0} - v_\zeta \Delta t_i) \cos\alpha - (Z - Z_{i0} - v_Z \Delta t_i) \sin\alpha, \tag{B.14}$$

$$k_x(t) = k_y S \Delta t_i + k_{x0}. \tag{B.15}$$

It is worth discussing the implications of the choice of the constant C. When $C = 0$, the perturbations are created at their peak amplitude, with their specific radial wavenumber, k_{x0}, and then evolve in the sheared velocity field. When $C > 0$, each perturbation grows and then decays and k_{x0} is then the radial wavenumber when the perturbation reaches its maximum amplitude. The choice of C does not affect the results of the analytic calculations of the correlation function in Appendix B.2, but it does affect the results calculated from the numerical implementation of this model described in Appendix B.5. In order to ensure that the time series generated by this model is smooth around the peak amplitude of single perturbations, which is necessary for the CCTD method described in Section 2.1.2 to work, we use a finite value of C.

B.2 Plasma-frame correlation function

In the calculation of the correlation function, we need only consider the correlation of each individual perturbation (B.2) with itself, because, in our model, each individual perturbation is independent of all other such perturbations. The two-point covariance function of a single perturbation, s_i, evaluated at (x_a, y_a, z_a, t_a) and (x_b, y_b, z_b, t_b) in the plasma frame is

$$\begin{aligned}\langle s_{ai} s_{bi} \rangle_P &\equiv \langle s_i(x_a, y_a, z_a, t_a) s_i(x_b, y_b, z_b, t_b) \rangle_P \\ &= \int \frac{s_{ai} s_{bi}\, \mathrm{d}A_i \mathrm{d}\phi_i \mathrm{d}x_{i0} \mathrm{d}y_{i0} \mathrm{d}z_{i0} \mathrm{d}t_{i0} \mathrm{d}t \mathrm{d}v_r}{(2\pi)^2 L_x L_y L_z T^2 \sigma_{\mathrm{amp}} \delta v_r} \exp\left(-\frac{A_i^2}{2\sigma_{\mathrm{amp}}^2} - \frac{v_r^2}{2\delta v_r^2} \right), \end{aligned} \tag{B.16}$$

where L_x, L_y, L_z, T are the compact supports of uniform probability distributions for the initial positions x_{i0}, y_{i0}, z_{i0}, and t_{i0}. The integration ranges for each of the variables are: $A_i \in [-\infty, \infty]$, $v_r \in [-\infty, \infty]$, $\phi_i \in [0, 2\pi]$, $x_{i0} \in [-L_x/2, L_x/2]$, $y_{i0} \in [-L_y/2, L_y/2]$, $z_{i0} \in [-L_z/2, L_z/2]$, t_i and $t \in [0, T]$. The radial velocity for each perturbation is taken from a Gaussian random distribution with zero mean and standard deviation δv_r. The toroidal and poloidal velocities are both assumed to be constant in space and time (in Chapter 6 we set $v_Z = 0$). We compute the integrals in (B.16) under the assumption that the integration ranges are much larger than the typical characteristic lengths/times in all directions (e.g., $L_x \gg \lambda_x$). Then it is possible to extend to infinity the limits of integration with respect to the random variables x_{i0}, y_{i0}, z_{i0} and t_{i0}, so that the integrals then become standard Gaussian integrals.

The two-point covariance function in the plasma frame is the sum of (B.16) over all individual perturbations

$$C_P^{\mathrm{cov}}(\Delta x, \Delta y, \Delta z, \Delta t) = \sum_{i=1}^{N} \langle s_{ai} s_{bi} \rangle_P. \tag{B.17}$$

It is a function only of the distance between the two points' locations and the time difference between them ($\Delta x = x_a - x_b, \Delta y = y_a - y_b, \Delta z = z_a - z_b, \Delta t = t_a - t_b$). After completing the integration in (B.16), (B.17) takes the form

$$\begin{aligned} &C_P^{\mathrm{cov}}(\Delta x, \Delta y, \Delta z, \Delta t) \\ &\quad = N \frac{\pi^2 \sigma_{\mathrm{amp}}^2 \lambda_x \lambda_y \lambda_\parallel \tau_c}{4 L_x L_y L_z T} \sqrt{G(\Delta t)} \\ &\qquad \times \exp\left\{ -\frac{\Delta x^2}{\ell_{x|P}^2} G(\Delta t) - \frac{\Delta y^2}{\ell_{y|P}^2} - \frac{\Delta z^2}{\ell_{z|P}^2} - \left[\frac{1}{\tau_{\mathrm{life}|P}^2} + \frac{k_{x|P}^2 \delta v_r^2}{2} G(\Delta t) \right] \Delta t^2 \right\} \\ &\qquad \times \cos\left[k_{x|P} G(\Delta t) \Delta x + k_{y|P} \Delta y \right]. \end{aligned} \tag{B.18}$$

The plasma-frame correlation function is then

$$C_P(\Delta x,\Delta y,\Delta z,\Delta t) \equiv \frac{C_P^{\rm cov}(\Delta x,\Delta y,\Delta z,\Delta t)}{C_P^{\rm cov}(0,0,0,0)}$$
$$= \sqrt{G(\Delta t)}\exp\left\{-\frac{\Delta x^2}{\ell_{x|P}^2}G(\Delta t)-\frac{\Delta y^2}{\ell_{y|P}^2}-\frac{\Delta z^2}{\ell_{z|P}^2}\right.$$
$$\left.-\left[\frac{1}{\tau_{{\rm life}|P}^2}+\frac{k_{x|P}^2\delta v_r^2}{2}G(\Delta t)\right]\Delta t^2\right\}$$
$$\times\cos\left[k_{x|P}G(\Delta t)\Delta x+k_{y|P}\Delta y\right], \tag{B.19}$$

where

$$\ell_{x|P}=\sqrt{2}\lambda_x'=\frac{\sqrt{2}\lambda_x}{\sqrt{1+(k_y\lambda_x S\tau_c/2)^2}}, \tag{B.20}$$
$$\ell_{y|P}=\sqrt{2}\lambda_y, \tag{B.21}$$
$$\ell_{z|P}=\sqrt{2}\lambda_\parallel, \tag{B.22}$$
$$\tau_{{\rm life}|P}=\sqrt{2}\tau_c'=\frac{\sqrt{2}\tau_c}{\sqrt{1+(k_y\lambda_x S\tau_c/2)^2}}, \tag{B.23}$$
$$k_{x|P}=k_{x0}, \tag{B.24}$$
$$k_{y|P}=k_y, \tag{B.25}$$
$$G(\Delta t)=\frac{\ell_{x|P}^2}{\ell_{x|P}^2+2\delta v_r^2\Delta t^2}. \tag{B.26}$$

The plasma-frame auto-correlation function has the form

$$C_P(0,0,0,\Delta t)=\sqrt{G(\Delta t)}\exp\left[-\left(\frac{1}{\tau_{{\rm life}|P}^2}+\frac{k_{x|P}^2\delta v_r^2}{2}G(\Delta t)\right)\Delta t^2\right]. \tag{B.27}$$

To define the plasma-frame correlation time $\tau_{c|P}$, we have to be able to compare the expression (B.27) with the plasma-frame auto-correlation function defined in (3.1), i.e., $\exp(-\Delta t^2/\tau_{c|P}^2)$. To do this, we expand the $G(\Delta t)$ term (B.26) for $\delta v_r\Delta t \ll \ell_{x|P}$, which is consistent with extending the asymptotic ordering (3.10-3.12) to include $\delta v_r \ll v_\zeta$ (this is formalised in Appendix C.1). Retaining terms to the lowest order $\mathcal{O}(\epsilon^2)$ in the exponent of (B.27), the plasma-frame correlation time of our model is then

$$\frac{1}{\tau_{c|P}^2}=\frac{1}{\tau_{{\rm life}|P}^2}+\left(k_{x|P}^2\ell_{x|P}^2+2\right)\frac{\delta v_r^2}{2\ell_{x|P}^2}. \tag{B.28}$$

The expressions for the plasma-frame correlation parameters defined by (3.1) are related to the characteristic lengths and times of the individual perturbations (B.2) via (B.20-B.28). When $\delta v_r=0$, (B.19) becomes exactly the same as the plasma-frame correlation function (3.1), and, as there are no $G(\Delta t)$ terms, there is no need to use the asymptotic ordering to find an expression for the plasma-frame correlation time

(i.e., $\tau_{c|P} = \tau_{\text{life}|P}$). When $\delta v_r \neq 0$, as is discussed in Section 8.2, the time dependence in (B.26) introduces cross-terms between spatial and temporal coordinates, and therefore, (B.19) is not equal to (3.1).

B.3 Laboratory-frame correlation function

To calculate the two-point covariance function in the laboratory frame, we follow the same procedure as in Appendix B.2, but write the individual perturbation (B.2) in laboratory frame coordinates using the transformations (B.12-B.14) and then integrate over the range of initial positions in the laboratory-frame coordinates $(r_{i0}, Z_{i0}, \zeta_{i0})$, rather than in the plasma-frame coordinates (x_{i0}, y_{i0}, z_{i0}). Explicitly,

$$\begin{aligned}\langle s_{ai} s_{bi} \rangle_L &\equiv \langle s_i(r_a, Z_a, \zeta_a = 0, t_a) s_i(r_b, Z_b, \zeta_b = 0, t_b) \rangle_L \\ &= \int \frac{s_{ai} s_{bi}\, \mathrm{d}A_i \mathrm{d}\phi_i \mathrm{d}r_{i0} \mathrm{d}Z_{i0} \mathrm{d}\zeta_{i0} \mathrm{d}t_{i0} \mathrm{d}t \mathrm{d}v_r}{(2\pi)^2 L_r L_Z L_\zeta T^2 \sigma_{\text{amp}} \delta v_r} \exp\left(-\frac{A_i^2}{2\sigma_{\text{amp}}^2} - \frac{v_r^2}{2\delta v_r^2}\right), \end{aligned} \tag{B.29}$$

where L_r, L_Z, L_ζ are the compact supports of uniform probability distributions for the initial positions of the perturbations $r_{i0}, Z_{i0}, \zeta_{i0}$. We complete this integration, in the same way as we did in Appendix B.2, by assuming that the integration ranges are large compared to the size of the perturbations, e.g. $L_r \gg \lambda_x$. Then the covariance function in the laboratory frame, defined analogously to (B.17), is

$$\begin{aligned} C_L^{\text{cov}}(\Delta r, \Delta Z, \Delta t) = F_0(\Delta t) \exp\left\{ - \left[F_1(\Delta t) \Delta r^2 + F_2 \Delta Z^2 + F_3 \Delta Z v_\zeta \Delta t + F_4(\Delta t) v_\zeta^2 \Delta t^2 \right] \right\} \\ \times \cos\left[F_5(\Delta t) \Delta r + F_6 \Delta Z + F_7 v_\zeta \Delta t \right], \end{aligned} \tag{B.30}$$

where, in terms of the plasma-frame correlation parameters (B.20-B.28),

$$F_0(\Delta t) = N \frac{\pi^2 \sigma_{\text{amp}}^2 \lambda_x \lambda_y \lambda_\parallel \tau_c}{4 L_r L_Z L_\zeta T} \sqrt{G(\Delta t)}, \tag{B.31}$$

$$F_1(\Delta t) = \frac{G(\Delta t)}{\ell_{x|P}^2}, \tag{B.32}$$

$$F_2 = \frac{\ell_{y|P}^2 \sin^2\alpha + \ell_{z|P}^2 \cos^2\alpha}{\ell_{y|P}^2 \ell_{z|P}^2}, \tag{B.33}$$

$$F_3 = \frac{(\ell_{y|P}^2 - \ell_{z|P}^2)\sin(2\alpha)}{\ell_{y|P}^2 \ell_{z|P}^2} + \frac{2 v_Z}{v_\zeta} \frac{(\ell_{y|P}^2 \sin^2\alpha - \ell_{z|P}^2 \cos^2\alpha)}{\ell_{y|P}^2 \ell_{z|P}^2}, \tag{B.34}$$

$$\begin{aligned} F_4(\Delta t) = &\frac{1}{v_\zeta^2 \tau_{\text{life}|P}^2} + \frac{\delta v_r^2}{2 v_\zeta^2} k_{x|P}^2 G(\Delta t) \\ &+ \frac{(v_\zeta \cos\alpha + v_Z \sin\alpha)^2}{\ell_{z|P}^2 v_\zeta^2} + \frac{(v_\zeta \sin\alpha + v_Z \cos\alpha)^2}{\ell_{y|P}^2 v_\zeta^2}, \end{aligned} \tag{B.35}$$

$$F_5(\Delta t) = k_{x|P} G(\Delta t), \tag{B.36}$$

$$F_6 = k_{y|P} \cos\alpha, \tag{B.37}$$

$$F_7 = -k_{y|P} \left(\sin\alpha + \frac{v_Z}{v_\zeta} \cos\alpha \right), \tag{B.38}$$

and where $G(\Delta t)$ is defined in (B.26). The laboratory-frame correlation function is defined analogously to the plasma-frame correlation function (B.19):

$$C_L(\Delta r, \Delta Z, \Delta t) = \sqrt{G(\Delta t)} \exp\left\{ - \left[F_1(\Delta t)\Delta r^2 + F_2 \Delta Z^2 + F_3 \Delta Z v_\zeta \Delta t + F_4(\Delta t) v_\zeta^2 \Delta t^2 \right] \right\} \times \cos\left[F_5(\Delta t)\Delta r + F_6 \Delta Z + F_7 v_\zeta \Delta t \right]. \tag{B.39}$$

When $\Delta t = 0$, the laboratory-frame correlation function (B.39) is exactly the same as (3.2), and the relationships (3.3-3.6) between the laboratory-frame and plasma-frame correlation parameters are determined by comparing these two expressions.

The procedure for calculating the relationship between the CCTD correlation time in the laboratory frame $\tau_{c|L}$ and the plasma-frame correlation time $\tau_{c|P}$ is described in Section 3.2.3, for the case when $\delta v_r = 0$. The detailed calculation of the laboratory-frame correlation time $\tau_{c|L}$ for the general case when $\delta v_r \neq 0$ is given in Appendix C.1, the results of which are discussed in Section 8.2.

B.4 Fluctuation amplitude

The plasma-frame mean square fluctuation amplitude is the amplitude of the plasma-frame covariance function (B.18) with $\Delta x = \Delta y = \Delta z = \Delta t = 0$, i.e.,

$$\sigma^2_{\mathrm{amp}|P} \equiv N \frac{\pi^2 \sigma^2_{\mathrm{amp}}}{4} \frac{\lambda_x \lambda_y \lambda_\parallel \tau_c}{L_x L_y L_z T}, \tag{B.40}$$

which is proportional to the mean square fluctuation amplitude of our model, σ^2_{amp}, introduced in (B.2). Similarly, the laboratory-frame mean square fluctuation amplitude is the amplitude of the laboratory-frame covariance function, $F_0(\Delta t = 0)$, given by (B.31)

$$\sigma^2_{\mathrm{amp}|L} \equiv N \frac{\pi^2 \sigma^2_{\mathrm{amp}}}{4} \frac{\lambda_x \lambda_y \lambda_\parallel \tau_c}{L_r L_Z L_\zeta T}. \tag{B.41}$$

As the volumes $L_x L_y L_z$ and $L_r L_Z L_\zeta$ are equal, the fluctuation amplitudes in both frames are the same.

For the plasma-frame (or laboratory-frame) fluctuation amplitude to be independent of the size of the domain, the number of individual perturbations s_i is chosen to be $N = \kappa L_x L_y L_z T / \lambda_x \lambda_y \lambda_\parallel \tau_c$, where κ is an arbitrary constant. The exact choice of κ does not affect the linear relationship between the plasma-frame (or laboratory-frame) fluctuation amplitude, $\sigma_{\mathrm{amp}|P}$ ($\sigma_{\mathrm{amp}|L}$), and the fluctuation amplitude σ_{amp} of the model field.

The finiteness of the spatial domain in which the model fluctuating signals are

generated can cause the plasma- and laboratory-frame fluctuation amplitudes to be lower when calculated from numerically generated time series than those expected from (B.41), because the integration limits in (B.29) cannot be extended to infinity. However, because the integration domain, spatial scales and velocity of the perturbations are all kept constant throughout the study of varying fluctuation amplitudes in Section 6.2.1, these effects simply cause the resulting fluctuation amplitude to be reduced by a constant factor [116]. Therefore, because we already have an arbitrary free parameter κ, we can rescale the analytic expression for the fluctuation amplitude (B.41) to match the value measured from the numerically generated fluctuating field. The effect of Gaussian-model PSFs on the laboratory-frame fluctuation amplitude can then be determined with (5.16) and compared with the effect of real PSFs (see Section 6.3.1).

B.5 Method for generating a fluctuating field

To generate a time series from the model of fluctuating fields described in Appendix B.1, one can simply use (B.1) and sum over N perturbations, each with its own random amplitude, phase, radial velocity, start time and position. However, N is determined from (B.41), and takes typical values of $N > 1000$, therefore evolving this number of perturbations over the whole four-dimensional (3 space + 1 time) domain requires long computation times.

In order to reduce the computation time, we use the fact that the contribution of a perturbation to a time series is localised in time, because $\tau_c \ll T$. Then we only have to calculate the contribution to the time series in a reduced time range centred around the time at which the perturbation reaches its peak amplitude. This is achieved through the introduction of the parameter C in (B.6), which determines the duration of time that a perturbation exists before reaching its peak amplitude. In Appendix B.2 and Appendix B.3, it was shown that the correlation function does not depend on C, provided that the integration range (in time) is taken to infinity. This is equivalent to ensuring that $C \gg 1$, so that each perturbation has sufficient time to grow and decay from and to near-zero amplitude.

Thus, for each individual perturbation, the density field is calculated on a sub-domain of the full domain $(r, Z, t) = (L_r, L_Z, C\tau_c)$. Then this sub-domain is added to the full domain (B.1) by positioning the sub-domain at the start time of the perturbation set by the random variable t_{i0}. The toroidal length of the domain is set by $L_\zeta = Cv_\zeta\tau_c$ so that only perturbations that will pass through $\zeta = 0$ during the reduced time period $C\tau_c$ are considered.

For typical turbulence parameters, using this approach to construct a fluctuating time series allows for the calculation of a $2\ \mathrm{ms}$, $30\ \mathrm{cm} \times 20\ \mathrm{cm}$ two-dimensional radial-

poloidal time series on a $0.5\ \mu$s and $0.5\ \mathrm{cm} \times 0.5\ \mathrm{cm}$ grid in less than 5 minutes using a desktop computer.

B.6 Input parameters

Input parameter	Value range	Description
λ_x / cm	0.75 — 5.0	Characteristic length in the radial direction
λ_y / cm	1.5 — (10) — 15	Characteristic length in the binormal direction
$\lambda_\parallel$ / cm	150.0	Characteristic length in the parallel direction
τ_c / μs	1 — (10) — 25	Characteristic life time
Θ /deg.	-45 — (25) — 45	Tilt angle of the correlation function
k_{x0} / cm^{-1}	$-k_y \cos\alpha \tan\Theta$	Radial wavenumber
k_y / cm^{-1}	(B.42)	Binormal wavenumber
σ_{amp}	0.1 — (1.0) — 2.0	Std. dev. of the amplitude of perturbations
v_ζ / cm/μs	0.5 — (1.5)* — 8.0	Bulk toroidal velocity (10 km/s)
v_Z / cm/μs	0.0	Poloidal velocity
δv_r / cm/μs	0.3	Standard deviation of radial velocity
S / μs^{-1}	0.02	Shearing rate
α / deg.	30	Pitch angle of the magnetic field
C	8	$C\tau_c$: existence time of a perturbation
L_r / cm	30	Radial length of the domain
L_Z / cm	20	Poloidal length of the domain
L_ζ / cm	$Cv_\zeta\tau_c$	Toroidal length of the domain
T/ μs	2000**	Duration of the simulation in time

Table B.1: Input parameters for generating time series from the model of fluctuating fields described in Section 6.1. Values in brackets are the fixed values used when varying other parameters. *In Figure 6.1(e), $v_\zeta = 3.0$ was used. **Except for Figure 8.2, where $T = 20$ ms.

The input parameters required to generate a time series of fluctuations from our model are listed in Table B.1 with the range of values used in this work also specified, for reference. The tilt angle $\Theta = -\arctan(k_{r|L}/k_{Z|L})$, has been made an input parameter for the model by using this to specify the radial wavenumber, $k_{x0} = -k_y \cos\alpha \tan\Theta$, where (3.6) has been used.

For our model field, we have chosen to fix the laboratory-frame poloidal wavenumber to the laboratory-frame poloidal correlation length: $k_{Z|L}\ell_{Z|L} = 2\pi$. This then requires that the input parameter k_y is fixed using

$$k_y = 2\pi \left(\frac{1}{2\lambda_y^2} + \frac{\tan^2\alpha}{2\lambda_\parallel^2} \right)^{1/2}, \tag{B.42}$$

where (3.4), (3.6), (B.21), and (B.22) have been used. This choice was influenced by the requirement to fix the product $k_{Z|B}\ell_{Z|B}$ in order to constrain a fit to the poloidal correlation function, which was done in previous studies by assigning the product

a value of 2π [28, 91]. We note that, by using the method described in Section 2.1.4 and Appendix A, we can now experimentally measure the product $k_{Z|B}\ell_{Z|B}$ from the auto-correlation function.

APPENDIX C

CCTD method: apparent poloidal velocity and correlation time

In Appendix C.1, we derive the expression for the laboratory-frame correlation time and apparent poloidal velocity that would be measured using the CCTD method (see Section 2.1.2) assuming that the correlation function has the form (B.39). The results include the effect of a Gaussian-distributed fluctuating radial velocity δv_r. They reduce to the results of Section 3.2.3 when $\delta v_r = 0$. In Appendix C.2, we discuss the details of the calculation for the BES-measured correlation time and apparent poloidal velocity, by starting from the correlation function including Gaussian-model PSF effects.

C.1 CCTD method in the laboratory frame

As the principle of the CCTD method was described in Section 3.2.3, here we focus on details, including how to perform the calculation accounting for a fluctuating radial velocity. The goal is to find expressions for the amplitude of the peak of the cross-correlation function $A_{\mathrm{peak}|L}(\Delta Z)$ and to find the time delay $\Delta t_{\mathrm{peak}|L}(\Delta Z)$ of this peak, both of which quantities are functions of the distance ΔZ between poloidally separated channels. Furthermore, we require the functional form of $A_{\mathrm{peak}|L}(\Delta Z)$ to be a Gaussian in ΔZ, so that it is possible to compare $A_{\mathrm{peak}|L}(\Delta Z)$ with the Gaussian fitting function used in (2.7) to measure the laboratory-frame correlation time $\tau_{c|L}$.

To proceed, we adopt the same asymptotic ordering (3.10-3.12) as in the main text, but include also a small radial velocity, which is modelled as a Gaussian-distributed random variable with zero mean and standard deviation δv_r. This standard deviation is then ordered small compared to the toroidal velocity $\delta v_r / v_\zeta \sim \epsilon$, and the same size as v_Z. Additionally, we express the time delay of the peak as $\Delta t_{\mathrm{peak}|L} = \Delta t_0 + \Delta t_1$, where $\Delta t_1 \sim \epsilon \Delta t_0$. The asymptotic ordering becomes

$$v_\zeta \tau_{c|P}, v_{\mathrm{th}i} \tau_{\mathrm{life}|P} \sim \ell_{z|P} \sim \mathcal{O}(R), \tag{C.1}$$

$$v_\zeta \Delta t_0 \sim \Delta Z, \Delta r, \ell_{x|P}, \ell_{y|P} \sim \mathcal{O}(\epsilon R), \tag{C.2}$$

$$v_Z \Delta t_0, \delta v_r \Delta t_0, v_\zeta \Delta t_1 \sim \mathcal{O}(\epsilon^2 R), \tag{C.3}$$

$$v_Z \Delta t_1, \delta v_r \Delta t_1 \sim \mathcal{O}(\epsilon^3 R). \tag{C.4}$$

C.1.1 Zeroth order

We assume that the correlation function has the form (B.39). We start by setting $\Delta r = 0$ in (B.39) and then neglect all terms that are smaller than $\mathcal{O}(\epsilon^0)$ in the arguments of the exponential and the cosine. The inclusion of a radial velocity has introduced a non-Gaussian dependence of the correlation function on the time delay Δt through the $G(\Delta t)$ function (B.26). However, realising that $\delta v_r \Delta t_0/\ell_{x|P} \sim \epsilon \ll 1$, we find that $G(\Delta t) = 1 + \mathcal{O}(\epsilon^2)$, and therefore, at the lowest order, we can neglect this effect. This gives the correlation function to zeroth order:

$$C_0(\Delta Z, \Delta t_0) = \exp\left[-\frac{(\Delta Z\cos\alpha - v_\zeta \Delta t_0 \sin\alpha)^2}{\ell_{y|P}^2}\right] \times \cos\left[k_{y|P}(\Delta Z\cos\alpha - v_\zeta \Delta t_0 \sin\alpha)\right]. \tag{C.5}$$

This is clearly a wave travelling at the apparent poloidal velocity $v_\zeta \tan\alpha$, with maxima occurring at

$$\Delta t_0 \equiv \Delta Z \cot\alpha / v_\zeta. \tag{C.6}$$

Note that these maxima do not decay in time. Therefore, we need to consider the small terms that we have neglected to determine how the amplitude of the peak of the correlation function (B.39) changes in time.

C.1.2 Second order corrections to the peak amplitude of the correlation function

To do this, we consider small deviations $\Delta t_1 \sim \epsilon \Delta t_0$ around the position of the maximum (C.6) of the zeroth-order correlation function (C.5). Then, by writing $\Delta t = \Delta t_0 + \Delta t_1$, and substituting this into (B.39), we find that the lowest-order terms that remain are $\mathcal{O}(\epsilon^2)$ (the peaks of the correlation function (B.39) do not decay at $\mathcal{O}(\epsilon^1)$). When carrying out this expansion, care must be taken, as the argument of the cosine is, in isolation, $\mathcal{O}(\epsilon^1)$, but, in order to compare this with the argument of the exponential in (B.39), we have to expand the cosine for small argument, which results in an $\mathcal{O}(\epsilon^2)$ contribution from the argument of the cosine. The correlation function (B.39), at second order in ϵ, is

$$C_2(\Delta Z, \Delta t_1) = \left(1 + \frac{2\delta v_r^2 \Delta Z^2}{\ell_{x|P}^2 v_\zeta^2 \tan^2\alpha}\right)^{-1/2} \exp\left[-\left(\frac{1}{\tau_{\text{life}|P}^2} + \frac{k_{x|P}^2 \ell_{x|P}^2 \delta v_r^2}{2\ell_{x|P}^2}\right)\frac{\Delta Z^2}{v_\zeta^2 \tan^2\alpha} - \frac{(v_\zeta \Delta t_1 \tan\alpha + v_Z \Delta Z \cot\alpha/v_\zeta)^2 \cos^2\alpha}{\ell_{y|P}^2} - \frac{\Delta Z^2}{\ell_{z|P}^2 \sin^2\alpha}\right] \times \cos\left[-\left(k_{y|P} v_\zeta \Delta t_1 \tan\alpha + k_{y|P} v_Z \Delta Z \cot\alpha/v_\zeta\right)\cos\alpha\right]. \tag{C.7}$$

At this order, the effects of the $G(\Delta t)$ term (B.26) first become evident. The coefficient of (C.7) has a dependence on ΔZ, which causes a non-Gaussian decay with ΔZ. As the second term in this coefficient is $\mathcal{O}(\epsilon^2)$ small, we make the following approximation

$$\left(1+\frac{2\delta v_r^2 \Delta Z^2}{\ell_{x|P}^2 v_\zeta^2 \tan^2\alpha}\right)^{-1/2} \simeq 1-\frac{\delta v_r^2 \Delta Z^2}{\ell_{x|P}^2 v_\zeta^2 \tan^2\alpha}+\mathcal{O}(\epsilon^4) \simeq \exp\left(-\frac{\delta v_r^2 \Delta Z^2}{\ell_{x|P}^2 v_\zeta^2 \tan^2\alpha}\right), \tag{C.8}$$

which means that this can be incorporated into the exponent of (C.7).

After using the approximation (C.8) in (C.7), we eliminate Δt_1 from the resulting expression by calculating the value of Δt_1 at the maximum of (C.7). The maximum of the correlation function occurs when

$$\Delta t_1 = -\frac{v_Z \Delta t_0}{v_\zeta \cot\alpha} - \frac{k_{y|P}\ell_{y|P}^2}{2 v_\zeta \sin\alpha}\tan\left[k_{y|P} v_\zeta \Delta t_1 \sin\alpha + k_{y|P} v_Z \Delta t_0 \cos\alpha\right], \tag{C.9}$$

which can be solved for Δt_1 by realising that the argument of the tangent is $\mathcal{O}(\epsilon^1)$ and, therefore, we may expand in this argument and obtain

$$\frac{\Delta t_1}{\Delta t_0} = -\frac{v_Z}{v_\zeta}\cot\alpha. \tag{C.10}$$

This implies that the peak of the cross-correlation function is shifted in time in comparison with the zeroth-order solution (C.6). Thus, the peak of the cross-correlation function occurs at

$$\Delta t_{\mathrm{peak}|L}(\Delta Z) = \left(1-\frac{v_Z}{v_\zeta}\cot\alpha\right)\frac{\Delta Z \cot\alpha}{v_\zeta} + \mathcal{O}(\epsilon^2 \Delta t_0). \tag{C.11}$$

C.1.3 Apparent poloidal velocity

We see immediately that the apparent poloidal velocity in the laboratory frame is then

$$\begin{aligned} v_{\mathrm{pol}|L} &\equiv \frac{\Delta Z}{\Delta t_{\mathrm{peak}|L}} = v_\zeta \tan\alpha \left(1-\frac{v_Z}{v_\zeta}\cot\alpha\right)^{-1} \\ &= v_\zeta \tan\alpha + v_Z + \mathcal{O}(\epsilon^2 v_\zeta), \end{aligned} \tag{C.12}$$

which is simply the sum of the projection of the toroidal velocity on to the poloidal plane, $v_\zeta \tan\alpha$, and the 'true' poloidal velocity v_Z (which is $\mathcal{O}(\epsilon^1)$ compared to v_ζ).

C.1.4 Correlation time

Using the result (C.10) in (C.7), we find the expression for the amplitude of the peak of the cross-correlation function between two detector channels separated by

a distance ΔZ to be

$$A_{\text{peak}|L}(\Delta Z) = \exp\left\{-\left[\frac{1}{\ell_{z|P}^2\cos^2\alpha} + \frac{1}{v_\zeta^2\tau_{\text{life}|P}^2} + \frac{(2+k_{x|P}^2\ell_{x|P}^2)}{2\ell_{x|P}^2}\frac{\delta v_r^2}{v_\zeta^2}\right]\Delta Z^2\cot^2\alpha\right\}. \tag{C.13}$$

To find the laboratory-frame correlation time, we compare (C.13) with the fitting function (2.7). This fitting function is given as a function of $\Delta t_{\text{peak}|L}$ by (C.11), however, because the exponent in (C.13) is only accurate to $\mathcal{O}(\epsilon^2)$, it is only necessary (and correct) to use the lowest-order part of (C.11). Therefore, the laboratory-frame correlation time is

$$\begin{aligned}\frac{1}{\tau_{c|L}^2} &= \frac{1}{\tau_{\text{life}|P}^2} + \frac{v_\zeta^2}{\ell_{z|P}^2\cos^2\alpha} + \left(\frac{2+k_{x|P}^2\ell_{x|P}^2}{2\ell_{x|P}^2}\right)\delta v_r^2 + \mathcal{O}\left(\frac{\epsilon^2}{\tau_{\text{life}|P}^2}\right), \\ &= \frac{1}{\tau_{c|P}^2} + \frac{v_\zeta^2}{\ell_{z|P}^2\cos^2\alpha}\end{aligned} \tag{C.14}$$

where $\tau_{c|P}$ is defined in (B.28). We see that the measurement of the correlation time is contaminated by the fluctuating-radial and bulk-toroidal velocities of the turbulent perturbations, but not by the small, constant poloidal velocity. Further discussion of this result is given in the main text; Sections 3.2.4 and Chapter 8.

C.2 PSF effects on the correlation time and apparent poloidal velocity

Now, we describe how to calculate the effect of PSFs on the correlation time and apparent poloidal velocity, including radial velocity effects. We start from the laboratory-frame covariance function (B.30), apply the PSFs using the integral (5.2) and define the BES correlation function analogously to (5.5). This expression is too cumbersome to reproduce here: it is similar in form to (B.39), but includes a cross-term between Δr and ΔZ similar to that in (5.7), arising due to the PSF integral.

With this BES correlation function, the exact same procedure is used as was described in Appendix C.1, starting from (B.39), though with the additional ordering of the PSF lengths to be the same order as the radial and binormal correlation lengths, $L_1, L_2 \sim \ell_{x|P}, \ell_{y|P}$, so (C.1-C.4) becomes:

$$v_\zeta\tau_{c|P}, v_{\text{th}i}\tau_{\text{life}|P} \sim \ell_{z|P} \sim \mathcal{O}(R), \tag{C.15}$$

$$v_\zeta\Delta t_0 \sim \Delta Z, \Delta r, \ell_{x|P}, \ell_{y|P}, L_1, L_2 \sim \mathcal{O}(\epsilon R), \tag{C.16}$$

$$v_Z\Delta t_0, \delta v_r\Delta t_0, v_\zeta\Delta t_1 \sim \mathcal{O}(\epsilon^2 R), \tag{C.17}$$

$$v_Z\Delta t_1, \delta v_r\Delta t_1 \sim \mathcal{O}(\epsilon^3 R). \tag{C.18}$$

The calculation of the time-delay $\Delta t_{\text{peak}|B}(\Delta Z)$ and amplitude $A_{\text{peak}|B}(\Delta Z)$ of the peak of the BES cross-correlation function becomes more extended than in Ap-

pendix C.1, because there are more $G(\Delta t)$ terms (B.26) that exist in the exponent of the BES correlation function (with $\Delta r = 0$). They arise because the PSF integral (5.2) brings (B.32) into the coefficients of the ΔZ terms. Therefore, to get the correct expression for the second-order correlation function, analogous to (C.7), it is necessary to approximate $G(\Delta t)$ using (C.8). However, other than this detail, the process is no different from that described in Appendix C.1.

The resulting expression for the time at which the peak of the cross-correlation function occurs is the same as (C.11), and is, therefore, unaffected by the PSFs. Thus, the apparent poloidal velocity that would be measured by the BES, $v_{\mathrm{pol}|B}$, is equal to the laboratory-frame apparent poloidal velocity (C.12), $v_{\mathrm{pol}|L}$. In contrast, the BES correlation time is affected by the PSFs:

$$\frac{1}{\tau_{c|B}^2} = \frac{1}{\tau_{c|L}^2} + (2 + k_{r|L}^2 \ell_{r|L}^2) \left(1 - \frac{\ell_{r|B}^2}{\ell_{r|L}^2}\right) \frac{\delta v_r^2}{2\ell_{r|B}^2} + \left(\frac{k_{Z|L}^2 \ell_{Z|L}^2}{2\ell_{r|B}^2} - \frac{k_{Z|L}^2 \ell_{Z|L}^4}{2D^4}\right) \delta v_r^2 + \mathcal{O}\left(\frac{\epsilon^2}{\tau_{c|L}^2}\right), \tag{C.19}$$

where we have written the expression in terms of both laboratory-frame (subscript L) and BES parameters (subscript B), and D is given by (5.13). The mixed notation is used in order to be concise, and should not cause concern, as the zero-time-delay expressions for the relationship between the two parameter sets are determined by (7.1-7.4), independent of any radial-velocity contributions. The result (C.19) is discussed in Section 8.2.

APPENDIX D

Quantifying the difference between real and Gaussian-model PSFs

In Section 4.5, we compared sets of real PSFs with sets of Gaussian-model PSFs, where each set of Gaussian-model PSFs had the same parameters L_1, L_2 and $\alpha_{\rm PSF}$. These parameters are, respectively, the means of the sets of parameters $\{L_{1i}\}, \{L_{2i}\}$ and $\{\alpha_{{\rm PSF}i}\}$ measured from each of the real PSFs, at channel i, using principal component analysis as described in Section 4.2. The purpose of this Appendix is to assess which part of the assumptions encoded in the Gaussian-model PSFs cause the biggest difference between these Gaussian-model PSFs and the real PSFs.

D.1 Difference of the shape of real PSFs from a tilted Gaussian function

The first assumption was that it was possible to describe the real PSFs by a Gaussian function. We measure the quality of this assumption by comparing each real PSF with a single Gaussian that has the parameters L_{1i}, L_{2i} and $\alpha_{{\rm PSF}i}$ measured from that real PSF. We use the measure

$$\Delta P_i = \frac{\mathrm{RMS}\left[P_i^{\rm real}(\mathbf{r}-\mathbf{r}_i) - P_i^{\rm Gauss}(\mathbf{r}-\mathbf{r}_i, L_{1i}, L_{2i}, \alpha_{{\rm PSF}i}, A_{{\rm PSF}i})\right]_{\mathbf{r}}}{A_{{\rm PSF}i}}, \tag{D.1}$$

which gives the root-mean-square (RMS) difference between the real PSF, $P_i^{\rm real}$, and the Gaussian model (4.2) of the same PSF, relative to the peak amplitude of the real PSF. The coordinates of the centre of the real PSF, $\mathbf{r}_i$, are determined by considering the line defined by $\alpha_{\rm PSF}$ and the point of the maximum of the PSF. The point on this line a distance L_1 from the e^{-1} contour towards the maximum of the PSF is taken to be $\mathbf{r}_i$.[1]

Averaging ΔP_i given by (D.1) over the set of channels in a BES subarray gives the measure plotted in the histogram of Figure D.1(a), for 245 different sets of PSFs. This shows that there is a variation of 12% to 20% in this 'difference from Gaussian' measure. Indeed, this Figure is very similar to Figure 4.2, and, therefore, most of the difference between using the Gaussian-model (with all PSFs the same) and the real PSFs is due to the assumption of a Gaussian shape for the PSFs.

[1] This is not the focal point of the BES, the difference will be discussed in Appendix D.4.

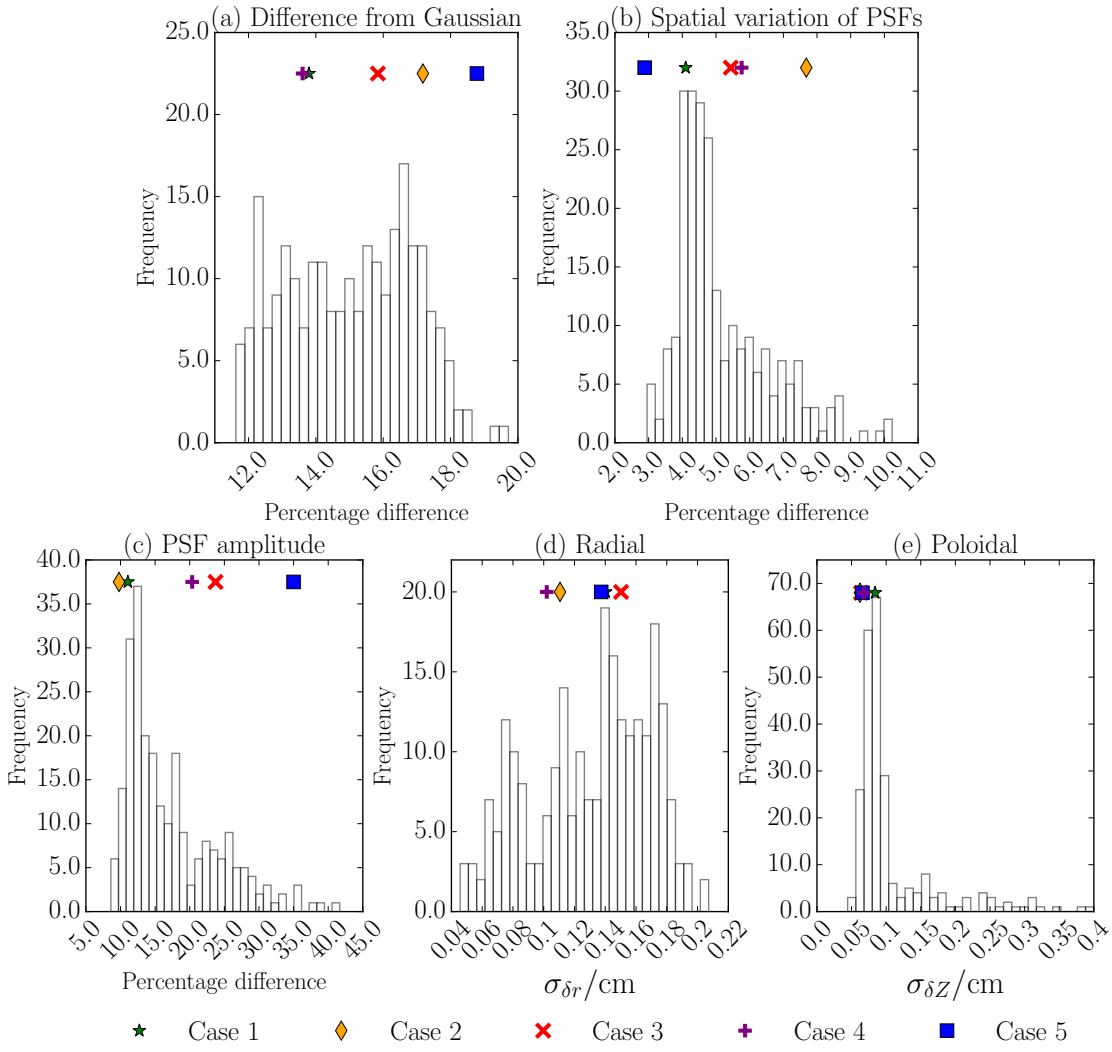


Figure D.1: Variation of real PSFs from Gaussian-model PSFs for 245 sets of PSFs calculated at various times in 20 MAST shots in DND configuration. The different measures are designed to measure: (a) the difference of the real PSFs from a Gaussian (Appendix D.1); (b) the spatial variation of the shape of the PSFs (Appendix D.2); (c) the spatial variation of the amplitudes of the PSFs (Appendix D.3); and (d) and (e) the variation across the channels of the weighted centre of the response compared to the focal centre (Appendix D.4). The values for each of the example cases, considered in Figure 2.1, are indicated with the coloured symbols. Case 5 is not included in the calculation of the histograms, yet is labelled for comparison.

D.2 Spatial variation of PSFs

To calculate the PSF effects analytically (Chapter 5), we had to assume that the shape of the PSFs was the same for all the detector channels. We measure how the PSFs vary in space, in violation of this assumption, using

$$\Delta\overline{P}_i = \mathrm{RMS}\left[P_i^{\mathrm{Gauss}}(\mathbf{r}-\mathbf{r}_i, L_{1i}, L_{2i}, \alpha_{\mathrm{PSF}i}) - P_i^{\mathrm{Gauss}}(\mathbf{r}-\mathbf{r}_i, L_1, L_2, \alpha_{\mathrm{PSF}})\right]_{\mathbf{r}}, \quad \text{(D.2)}$$

which is the difference between the Gaussian-model PSFs for each channel and the Gaussian-model PSFs using the mean PSF parameters $(L_1, L_2, \alpha_{\mathrm{PSF}})$ over the set of channels being considered. For this measure, we have assumed that all PSFs have the same amplitude and central locations $\mathbf{r}_i$. The average over a set of channels of $\Delta\overline{P}_i$ is plotted in the histogram of Figure D.1(b). This shows that most sets of PSFs have a spatial variation of 4% to 5%, suggesting that the spatial variation of the PSFs across the subarray is of secondary importance compared to the difference of the real PSF shape from a Gaussian.

D.3 Variation of PSF amplitudes

In Figure D.1(c), we consider the variation in amplitude of the PSFs across the array. The Figure shows the standard deviation of the $A_{\mathrm{PSF}i}$, relative to the mean of this quantity, over a set of channels. There is a large variation compared to the previous two measures, with some cases varying up to 40%, however this is the tail of the distribution, with the most frequent variation around 10%. We note, however, the amplitudes of the PSFs cancel in the calculation of the covariance function (2.3), as shown in Section 5.1. Therefore, the variation in the amplitudes of the PSFs can have no effect on the correlation function (2.4).

D.4 Shifted centres of PSFs

When using the Gaussian-model PSFs, we assumed that the peak response was located at the focal points $(r_{\mathrm{focal}i}, Z_{\mathrm{focal}i})$ of the detector channels (black dots in Figure 2.1). However, as can be seen in Figure 2.1, the PSF contours are in fact shifted from their focal centres. In order to measure this discrepancy, we first calculate the location of the weighted mean response of a PSF P_i^{real} in the radial direction, relative to the focal point of that PSF:

$$\delta r_i = \frac{\int \mathrm{d}r\mathrm{d}Z(r-r_{\mathrm{focal}i})P_i^{\mathrm{real}}(r-r_{\mathrm{focal}i}, Z-Z_{\mathrm{focal}i})}{\int \mathrm{d}r\mathrm{d}Z P_i^{\mathrm{real}}(r_k-r_{\mathrm{focal}i}, Z-Z_{\mathrm{focal}i})}. \quad \text{(D.3)}$$

We consider the standard deviation $\sigma_{\delta r}$ of δr_i over a subarray of BES channels as our measure of the difference between the focal point and the location of the mean response of the PSFs. This is because we are interested only in the irregularity of the

PSF response locations, and not in mean shifts to the position of the PSF response, as the latter would not alter the shape of the correlation function.

A similar definition is adopted for the poloidal difference δZ_i. The two measures $\sigma_{\delta r}$ and $\sigma_{\delta Z}$ are plotted in Figures D.1(d) and D.1(e), respectively. The radial and poloidal variation of the mean PSF response from the regular grid of focal points is at most a few millimetres, which is an order of magnitude smaller than the typical sizes of the PSFs and of turbulent structures. Therefore, these effects can be neglected and it is reasonable to assume that there is no difference between the peak response of the PSFs $\mathbf{r}_i$ and the focal point of the BES $\mathbf{r}_{\mathrm{focal}i}$.

APPENDIX E

Measuring skewed distributions

Experimental measurement of skewed (or otherwise) distributions of the fluctuating intensity fields is complicated by a number of extraneous effects, which we detail and describe how to correct for in Appendix E.1. In Appendix E.2, we determine the effect of PSFs on the skewness of the fluctuating-field distributions.

E.1 Accounting and correcting for spurious skewness

The distribution of fluctuating intensities of the raw BES signal can be skewed for two main reasons not associated with the symmetry breaking of the turbulent field: the presence of high-energy radiation and the slow variation of the intensity signal. We discuss these effects by considering Figure E.1(a), where the distribution of (unnormalised) fluctuating intensities from the raw BES signal for the DLM case (see Section 11.4) is plotted.

First, let us consider the smaller (in this case) of the two effects: the low-probability tail on the right-hand side of the distribution in Figure E.1(a). This tail is caused by high-energy radiation (neutron, gamma ray, or hard X-ray) impinging on the avalanche-photodiode detector (APD) of the BES camera and producing spikes in the time series that are isolated to a single detector channel.

We can observe this effect more clearly by analysing BES data from another MAST shot (#27367), where the shutter over the optical system of the BES diagnostic was closed, and so no beam-emission photons were able to reach the APD. The distribution of unnormalised fluctuating intensities for this "shutter-closed" case is plotted in Figure E.1(d). It can be seen to be made up of two components: the first is a Gaussian distribution of photon (electronic) noise, the second is a tail of positive δI due to the high-energy radiation, causing large positive skewness $S = 11.77$.

The sum of two randomly distributed independent variables (here, beam-emission photons and high-energy radiation) has a probability distribution that is the convolution of the probability distributions of the two variables (see, e.g., [117]). Therefore, formally, knowing (having measured) the probability distribution of the radiation spikes, it is possible to deconvolve this probability distribution from an experimentally measured probability distribution. However, this is not possible in practice because the actual number of large-amplitude radiation spikes is small (typ-

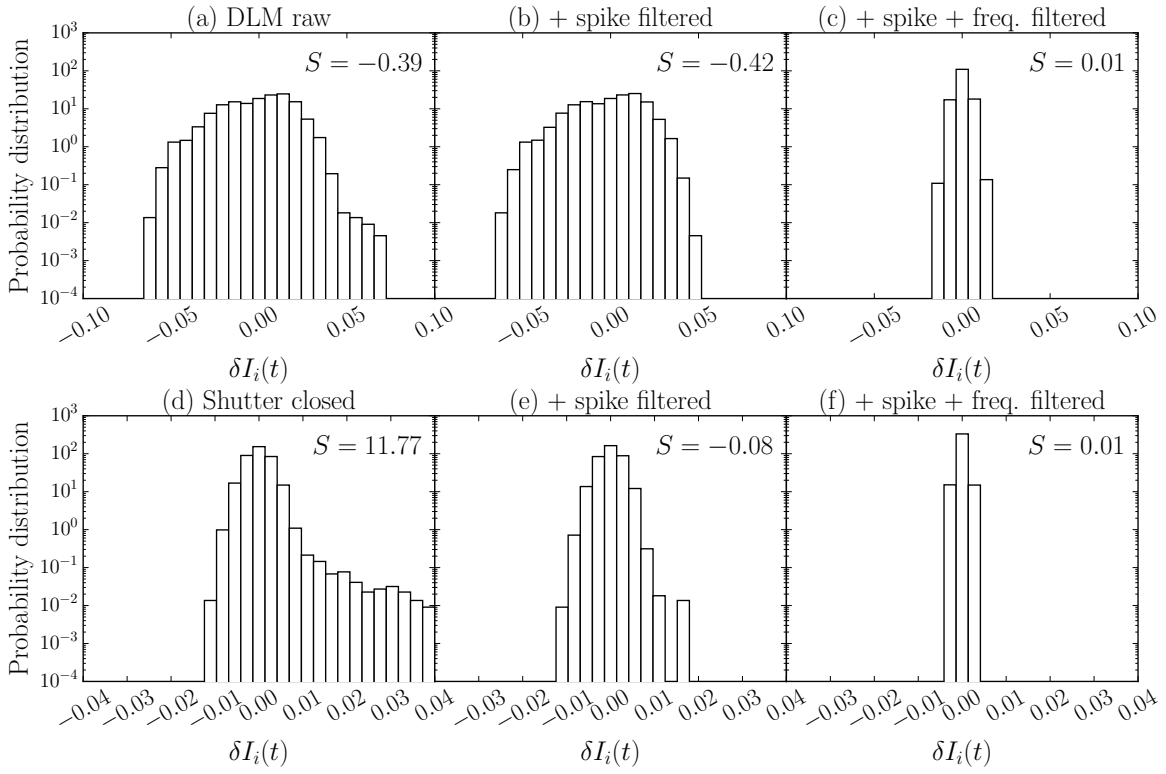


Figure E.1: Probability distribution of the intensity perturbation δI_i (unnormalised) for (a) the DLM case (see Section 11.2) for 2×4 BES channels, as in Figure 11.5(b); (b) the same as (a) but spike-filtered; (c) the same as (a) but spike- and then bandpass-filtered in the range $20 - 100$ kHz; (d) the detected signal of the BES diagnostic when the shutter is closed, measured during shot #27367 at $t \in [250, 252]$ ms, using the 5×4 channels inner BES subarray; (e) the same as (d) but spike-filtered; (f) same as (d) but spike- and then bandpass-filtered in the range $20 - 100$ kHz. Note the different x-axis scales in (a-c) and (d-f).

ically at most one or two per channel in a 2 ms time window). As a result, we resort to a cruder method, but an effective one, of removing the radiation spikes from the time series by identifying large (above a certain threshold) differences between the intensity at one point in time and the next, and then replacing this large-intensity value with the value of the neighbouring point.[1] [54] The result of this "spike filtering" can be seen in Figure E.1(e), where the large tail of the distribution in Figure E.1(d) has been successfully removed by this method.

However, our spike filter is not able to remove all of the radiation spikes, especially ones with smaller amplitudes. These remaining low-amplitude radiation spikes cause high-frequency variations in the time series. Therefore, a low-pass filter can be used to remove them. A low-pass filter is also necessary to remove

[1]The radiation spikes can persist over a number of sampling times (each equal to 0.5 μs), so the spike-filtering algorithm is designed to fill in up to 4 time points with neighbouring values.

high-frequency (above 100 kHz) noise from the signal (see Figure 11 of [54]). In order to account for the slow variation of the intensity signal (which will be discussed shortly), a high-pass filter is also required. Therefore, we use a bandpass filter in the range $20 - 100$ kHz on the BES-measured time series. The outcome is shown in Figure E.1(f). The skewness of the fluctuating-intensity distribution in this figure is nearly zero, demonstrating that this process can successfully account for the skewness caused by high-energy radiation and gives us an estimate of the uncertainty with which we can measure the skewness of the distribution of the turbulent field (in the absence of other effects; see Appendix E.2). Returning to the DLM case, in Figure E.1(b), we see that the spike filter successfully removes the low-probability tail.

Now we consider the second spurious source of skewness in the distribution: the slow ($\sim$ ms) time evolution of the intensity signal due to changes in the equilibrium and slow MHD modes (> 50 μs). If, during a given time interval, the (running) mean intensity signal varies unevenly (for example, decreases slightly for the last third of the time interval), then the mean over the entire time interval $\langle I_i(t) \rangle$ will be weighted by this variation. The distribution of the fluctuating part of the intensity signal, $\delta I_i(t) = I_i(t) - \langle I_i(t) \rangle$, will then be skewed. Therefore, a high-pass filter is used to remove all variations of the intensity signal with frequencies below 20 kHz. We demonstrate the effect of using such a filter (in combination with the low-pass filter discussed above) on the DLM case, which has, on inspection of the raw time series, a slow, uneven variation in the intensity signal over a 2 ms time interval. In Figure E.1(c), the $20 - 100$ kHz bandpass filter reduces the skewness in the distribution significantly, compared to that in Figure E.1(b). We have now recovered the distribution that was shown in Figure 11.5(b).

We finish by noting another possible source of spurious skewness in the distribution of fluctuating intensities, the background emission from the plasma. Intensity distributions for the cases either when there is no neutral beam heating or when only the SW neutral beam is active (the BES images the SS beam), are similar to that of the shutter-closed case in Figure E.1(d). Therefore, we do not expect the background plasma emission to produce a skewness larger than that caused by the high-energy radiation, and that we have been able to account and correct for.

E.2 PSF effects

We now consider PSF effects on the distribution of the fluctuating field. In the first row of Figure E.2, panels (a-c), we reproduce the three distributions of the numerically simulated fluctuating density field already plotted in Figure 12.5 (these are the distributions for the GKa5, GKa1, and Marginal runs). In each of the fol-

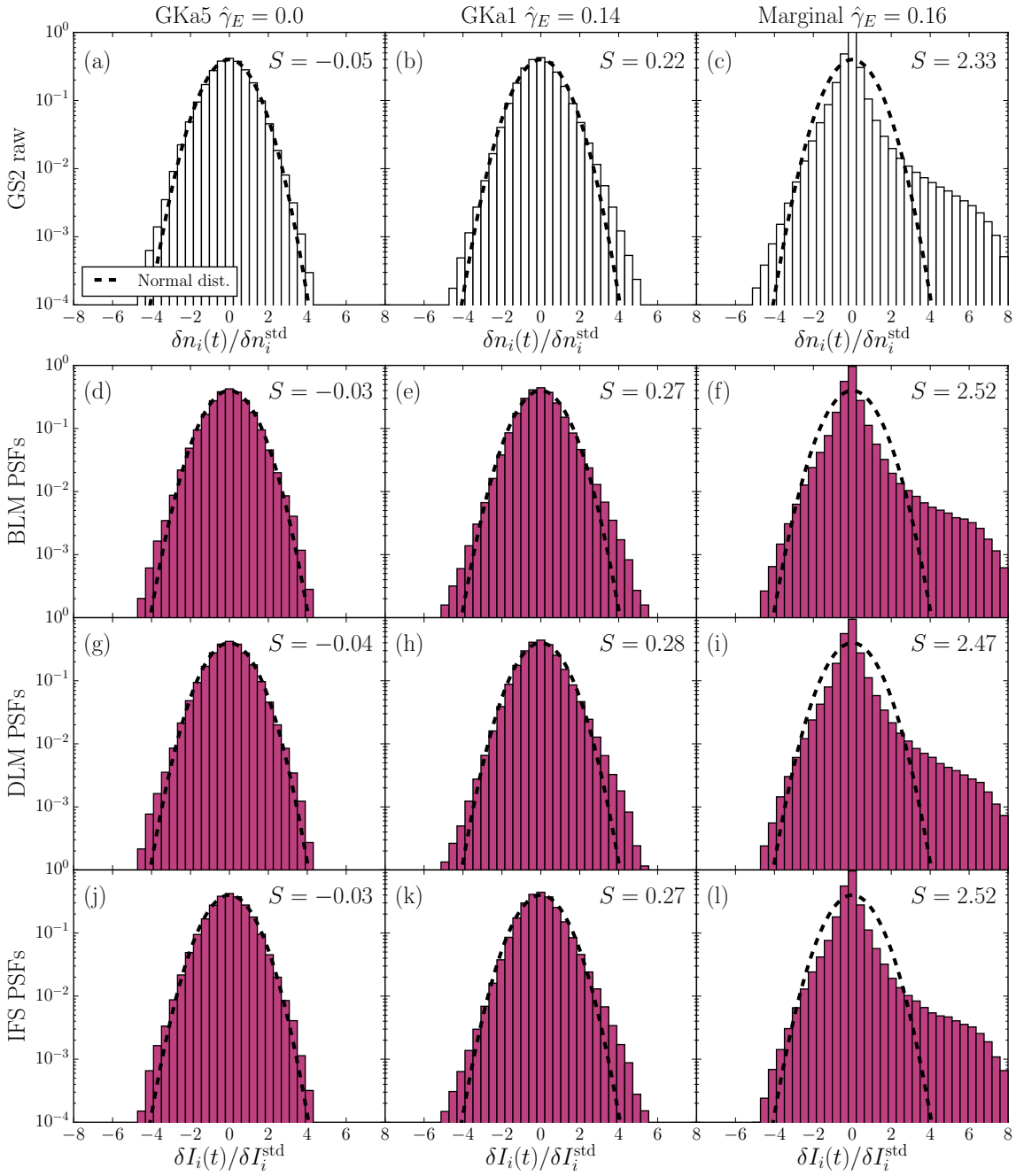


Figure E.2: Effect of PSFs on the distribution of amplitudes from the GKa5, GKa1, and Marginal simulations. The intensity fields (d-l) are calculated from the density fields (a-c) by evaluating (2.1). The dashed line in each plot is the unit normal distribution.

lowing rows, we plot the distributions of the fluctuating intensity field calculated from the density field used in panels (a-c) and using the PSFs of the BES diagnostic calculated for each experimental case that we considered in Section 11.4: the second row, panels (d-f), is for the BLM case, the third row, panels (g-i), is for the DLM case, and the fourth row, panels (j-l), is for the IFS case. The relationship between the density field, the intensity field and the PSFs is given by (2.1), and the coefficient $\beta \equiv (\delta I/I)/(\delta n/n)$ is related to the atomic physics of the line emission and is a weak function of density [65] (for our three experimental cases, it is approximately constant: $\beta = 0.7$).

For the run with zero flow shear (GKa5), we see from the first column of Figure E.2 that the skewness is changed from -0.05 without PSFs to at most -0.03 when applying the PSFs. In the second column of Figure E.2, we see similar behaviour for the runs with a moderate flow shear (GKa1), with a maximum increase in the skewness of 0.06. For the Marginal run, the skewness is again increased by the PSFs, but by an even lesser amount, in the 10% range (irrelevant compared to the true skewness for these runs). It is clear that in the runs with non-zero flow shear the change in skewness due to the PSFs is small compared to the true value of skewness. These results suggest that the difference in skewness between the three experimental cases considered in Section 11.4 cannot be due solely to PSF effects. In fact, we see that all three of the sets of PSFs taken from the experimental cases have similar effects on the distribution of the fluctuating field.

Bibliography

[1] R. A. B. Mynors, R. M. Thomson, and M. Winterbottom, *William of Malmesbury, Gesta regum Anglorum / The history of the English kings*, Oxford Medieval Texts, 1998-9.

[2] J. D. Lawson, Proceedings of the Physical Society. Section B **70**, 6 (1957).

[3] J. Wesson and D. J. Campbell, *Tokamaks*, volume 149, Oxford University Press, 2011.

[4] C. Gormezano et al., Phys. Rev. Lett. **80**, 5544 (1998).

[5] J. P. Freidberg, *Plasma physics and fusion energy*, Cambridge University Press, 2008.

[6] Y.-c. Ghim et al., Nucl. Fusion **54**, 042003 (2014).

[7] R. J. Akers et al., Plasma Physics and Controlled Fusion **45**, A175 (2003).

[8] P. A. Davidson, *Turbulence: An Introduction for Scientists and Engineers: An Introduction for Scientists and Engineers*, Oxford University Press, 2004.

[9] G. Hammett, Physical mechanisms driving gyrokinetic turbulence, in *Vienna Gyrokinetic Workshop*, pages 15–19, 2008.

[10] S. C. Cowley, R. M. Kulsrud, and R. Sudan, Phys. Fluids B **3**, 2767 (1991).

[11] M. Rosenbluth and C. Longmire, Annals of Physics **1**, 120 (1957).

[12] G. Colyer et al., ArXiv e-prints (2016).

[13] W. Dorland, F. Jenko, M. Kotschenreuther, and B. N. Rogers, Phys. Rev. Lett. **85**, 5579 (2000).

[14] B. B. Kadomtsev and O. P. Pogutse, Soviet Physics Doklady **14**, 470 (1969).

[15] J. W. Connor, R. J. Hastie, and P. Helander, Plasma Physics and Controlled Fusion **48**, 885 (2006).

[16] C. M. Roach et al., Plasma Physics and Controlled Fusion **51**, 124020 (2009).

[17] L. N. Trefethen, A. E. Trefethen, S. C. Reddy, and T. A. Driscoll, Science **261**, 578 (1993).

[18] A. A. Schekochihin, E. G. Highcock, and S. C. Cowley, Plasma Phys. Control. Fusion **54**, 055011 (2012).

[19] E. G. Highcock et al., Phys. Rev. Lett. **109**, 265001 (2012).

[20] P. C. Liewer, Nucl. Fusion **25**, 543 (1985).

[21] C. P. Ritz et al., Rev. Sci. Instrum. **59**, 1739 (1988).

[22] B. Koch et al., J. of Nucl. Materials **363**, 1056 (2007).

[23] Y.-c. Ghim et al., Plasma Phys. Control. Fusion **54**, 095012 (2012).

[24] P. Goldreich and S. Sridhar, Astrophys. J. **438**, 763 (1995).

[25] S. V. Nazarenko and A. A. Schekochihin, J. Fluid Mech. **677**, 134 (2011).

[26] M. A. Forman, R. T. Wicks, and T. S. Horbury, The Astrophysical Journal **733**, 76 (2011).

[27] M. Barnes, F. I. Parra, and A. A. Schekochihin, Phys. Rev. Lett. **107**, 115003 (2011).

[28] Y.-c. Ghim et al., Phys. Rev. Lett. **110**, 145002 (2013).

[29] F. L. Hinton and S. K. Wong, Phys. Fluids **28**, 3082 (1985).

[30] J. Rice et al., Nucl. Fusion **39**, 1175 (1999).

[31] J. Hillesheim et al., Nucl. Fusion **55**, 032003 (2015).

[32] F. I. Parra and M. Barnes, Plasma Phys. Control. Fusion **57**, 045002 (2015).

[33] K. H. Burrell, Phys. Plasmas **4**, 1499 (1997).

[34] S. Newton and P. Helander, Phys. Plasmas **13**, 012505 (2006).

[35] A. R. Field et al., Plasma Phys. Control. Fusion **51**, 105002 (2009).

[36] L. Schmitz et al., Phys. Rev. Lett. **108**, 155002 (2012).

[37] P. J. Catto, M. N. Rosenbluth, and C. S. Liu, Phys. Fluids **16**, 1719 (1973).

[38] M. Barnes et al., Phys. Rev. Lett. **106**, 175004 (2011).

[39] S. L. Newton, S. C. Cowley, and N. F. Loureiro, Plasma Phys. Control. Fusion **52**, 125001 (2010).

[40] F. van Wyk et al., ArXiv:1607.08173 (2016).

[41] P. W. Terry, Rev. Mod. Phys. **72**, 109 (2000).

[42] F. Wagner et al., Phys. Rev. Lett. **49**, 1408 (1982).

[43] F. Wagner, Plasma Phys. Control. Fusion **49**, B1 (2007).

[44] H. Biglari, P. H. Diamond, and P. W. Terry, Phys. Fluids B: Plasma Physics **2**, 1 (1990).

[45] K. C. Shaing, E. C. Crume, and W. A. Houlberg, Phys. Fluids B **2**, 1492 (1990).

[46] R. E. Waltz, G. D. Kerbel, and J. Milovich, Phys. Plasmas **1**, 2229 (1994).

[47] T. S. Hahm and K. H. Burrell, Phys. Plasmas **2**, 1648 (1995).

[48] T. S. Hahm et al., Physics of Plasmas **6**, 922 (1999).

[49] E. G. Highcock et al., Phys. Rev. Lett. **105**, 215003 (2010).

[50] A. Sykes et al., Nucl. Fusion **41**, 1423 (2001).

[51] M. Cox, Fusion Eng. Des. **46**, 397 (1999).

[52] Y. Peng, *Spherical torus, compact fusion at low field*, 1984.

[53] Y. M. Peng and D. J. Strickler, Nucl. Fusion **26**, 769 (1986).

[54] A. R. Field et al., Rev. Sci. Instrum. **83**, 013508 (2012).

[55] J. Hillesheim et al., Nucl. Fusion **55**, 073024 (2015).

[56] D. Thomas et al., Nucl. Fusion **56**, 026013 (2016).

[57] L. Lao et al., Nucl. Fusion **25**, 1611 (1985).

[58] I. Lupelli et al., Fusion Eng. Des. **9697**, 835 (2015), Proceedings of the 28th Symposium On Fusion Technology (SOFT-28).

[59] N. J. Conway et al., Rev. Sci. Instrum. **77**, 10F131 (2006).

[60] R. Scannell et al., Rev. Sci. Instrum. **79**, 10E730 (2008).

[61] R. Scannell et al., Rev. Sci. Instrum. **81**, 10D520 (2010).

[62] N. J. Conway et al., Rev. Sci. Instrum. **81**, 10D738 (2010).

[63] M. J. Hole, L. C. Appel, and R. Martin, Rev. Sci. Instrum. **80**, 123507 (2009).

[64] R. J. Fonck, P. A. Duperrex, and S. F. Paul, Rev. Sci. Instrum. **61**, 3487 (1990).

[65] I. H. Hutchinson, Plasma Phys. Control. Fusion **44**, 71 (2002).

[66] Y.-c. Ghim, A. R. Field, S. Zoletnik, and D. Dunai, Rev. Sci. Instrum. **81**, 10D713 (2010).

[67] I. G. Kiss et al., Fusion Engineering and Design **86**, 1315 (2011), Proceedings of the 26th Symposium of Fusion Technology (SOFT-26).

[68] D. Dunai, S. Zoletnik, J. Srkzi, and A. R. Field, Rev. Sci. Instrum. **81**, 103503 (2010).

[69] M. Kotschenreuther, G. Rewoldt, and W. Tang, Comp. Phys. Comm. **88**, 128 (1995).

[70] I. G. Abel et al., Rep. Prog. Phys. **76**, 116201 (2013).

[71] E. G. Highcock, ArXiv: 1207.4419 (2012).

[72] W. W. Lee, The Physics of Fluids **26**, 556 (1983).

[73] M. F. J. Fox et al., ArXiv: 1609.09534 (2016).

[74] M. F. J. Fox et al., Plasma Physics and Controlled Fusion **59**, 034002 (2017).

[75] S. F. Paul and R. J. Fonck, Rev. Sci. Instrum. **61**, 3496 (1990).

[76] G. McKee et al., Rev. Sci. Instrum. **70**, 913 (1999).

[77] D. R. Smith et al., Rev. Sci. Instrum. **81**, 10D717 (2010).

[78] Y. U. Nam, S. Zoletnik, M. Lampert, and A. Kovácsik, Rev. Sci. Instrum. **83**, 10D531 (2012).

[79] R. D. Durst et al., Rev. Sci. Instrum. **63**, 4907 (1992).

[80] M. W. Shafer et al., Phys. Plasmas **19**, 032504 (2012).

[81] D. Moulton, Y. Marandet, P. Tamain, and G. Dif-Pradalier, Nucl. Fusion **55**, 073025 (2015).

[82] G. Hornung et al., Physics of Plasmas **18**, 082303 (2011).

[83] G. I. Taylor, Proc. R. Soc. Lond. A Math. Phys. Sci. **164**, 476 (1938).

[84] D. R. Smith et al., Phys. Plasmas **20**, 055903 (2013).

[85] P. J. Catto, I. B. Bernstein, and M. Tessarotto, Phys. Fluids **30**, 2784 (1987).

[86] A. A. Schekochihin et al., J. Plasma Phys. **82** (2016).

[87] M. W. Shafer, R. J. Fonck, G. R. McKee, and D. J. Schlossberg, Rev. Sci. Instrum. **77**, 10F110 (2006).

[88] I. Jolliffe, *Principal Component Analysis*, Springer, 2002.

[89] S. Zoletnik et al., Rev. Sci. Instrum. **76**, 073504 (2005).

[90] B. Tal et al., Phys. Plasmas **18**, 122304 (2011).

[91] A. R. Field et al., Plasma Phys. Control. Fusion **56**, 025012 (2014).

[92] N. Fedorczak, P. H. Diamond, G. Tynan, and P. Manz, Nucl. Fusion **52**, 103013 (2012).

[93] J. Luxon, Nucl. Fusion **42**, 614 (2002).

[94] G. R. Tynan, A. Fujisawa, and G. McKee, Plasma Phys. Control. Fusion **51**, 113001 (2009).

[95] Y. Koide et al., Phys. Rev. Lett. **72**, 3662 (1994).

[96] R. Nazikian et al., Phys. Rev. Lett. **94**, 135002 (2005).

[97] J. Connor et al., Nucl. Fusion **44**, R1 (2004).

[98] F. I. Parra, M. Barnes, and A. G. Peeters, Phys. Plasmas **18**, 062501 (2011).

[99] H. Sugama, T. H. Watanabe, M. Nunami, and S. Nishimura, Plasma Phys. Control. Fusion **53**, 024004 (2011).

[100] I. Chapman et al., Nucl. Fusion **55**, 104008 (2015).

[101] J. A. Alonso et al., Plasma Phys. Control. Fusion **48**, B465 (2006).

[102] I. Shesterikov et al., Nucl. Fusion **52**, 042004 (2012).

[103] T. A. Carter and J. E. Maggs, Phys. Plasmas **16**, 012304 (2009).

[104] D. Howell, T. Hender, and G. Cunningham, Nucl. Fusion **47**, 1336 (2007).

[105] F. van Wyk et al., In preparation (2016).

[106] E. G. Highcock, N. R. Mandell, M. Barnes, and W. Dorland, arXiv:1608.08812 (2016).

[107] B. N. Rogers, W. Dorland, and M. Kotschenreuther, Phys. Rev. Lett. **85**, 5336

(2000).

[108] P. H. Diamond, S.-I. Itoh, K. Itoh, and T. S. Hahm, Plasma Phys. and Control. Fusion **47**, R35 (2005).

[109] G. W. Hammett et al., Plasma Physics and Controlled Fusion **35**, 973 (1993).

[110] I. G. Abel and S. C. Cowley, New J. Phys. **15**, 023041 (2013).

[111] G. R. McKee, C. Fenzi, R. J. Fonck, and M. Jakubowski, Rev. Sci. Instrum. **74**, 2014 (2003).

[112] G. R. McKee et al., Plasma Physics and Controlled Fusion **45**, A477 (2003).

[113] G. R. McKee et al., Rev. Sci. Instrum. **75**, 3490 (2004).

[114] D. K. Gupta et al., Phys. Rev. Lett. **97**, 125002 (2006).

[115] A. R. Field et al., Proc. 25th IAEA Fusion Energy Conf., St. Petersburg, 13–18 Oct. 2014, paper EX/P4-38 .

[116] J. Kim et al., Comp. Phys. Comm. **204**, 152 (2016).

[117] J. Bendat and A. Piersol, *Random Data: Analysis and Measurement Procedures*, Wiley Series in Probability and Statistics, Wiley, 2011.